

VOLUME 34

JUNE 1956

NUMBER 6

Canadian Journal of Physics

Editor: G. M. VOLKOFF

Associate Editors:

L. G. ELLIOTT, *Atomic Energy of Canada, Ltd., Chalk River*

J. S. FOSTER, *McGill University*

G. HERZBERG, *National Research Council of Canada*

L. LEPRINCE-RINGUET, *Ecole Polytechnique, Paris*

R. W. PRINGLE, *University of Manitoba*

B. W. SARGENT, *Queen's University*

Sir FRANCIS SIMON, *Clarendon Laboratory, University of Oxford*

W. H. WATSON, *University of Toronto*

Published by THE NATIONAL RESEARCH COUNCIL
OTTAWA CANADA

CANADIAN JOURNAL OF PHYSICS

(Formerly Section A, Canadian Journal of Research)

Under the authority of the Chairman of the Committee of the Privy Council on Scientific and Industrial Research, the National Research Council issues **THE CANADIAN JOURNAL OF PHYSICS** and six other journals devoted to the publication, in English or French, of the results of original scientific research. Matters of general policy concerning these journals are the responsibility of a joint Editorial Board consisting of: members representing the National Research Council of Canada; the Editors of the Journals; and members representing the Royal Society of Canada and four other scientific societies.

EDITORIAL BOARD

Representatives of the National Research Council

A. N. Campbell, *University of Manitoba*
G. E. Hall, *University of Western Ontario*
H. G. Thode, *McMaster University*
D. L. Thomson, *McGill University*
W. H. Watson (Chairman), *University of Toronto*

Editors of the Journals

D. L. Bailey, *University of Toronto*
T. W. M. Cameron, *Macdonald College*
J. B. Collip, *University of Western Ontario*
G. A. Ledingham, *National Research Council*
Léo Marion, *National Research Council*
R. G. E. Murray, *University of Western Ontario*
G. M. Volkoff, *University of British Columbia*

Representatives of Societies

D. L. Bailey, *University of Toronto*
Royal Society of Canada
T. W. M. Cameron, *Macdonald College*
Royal Society of Canada
J. B. Collip, *University of Western Ontario*
Canadian Physiological Society
R. G. E. Murray, *University of Western Ontario*
Canadian Society of Microbiologists
H. G. Thode, *McMaster University*
Chemical Institute of Canada
T. Thorvaldson, *University of Saskatchewan*
Royal Society of Canada
G. M. Volkoff, *University of British Columbia*
Royal Society of Canada; Canadian Association of Physicists

Ex officio

Léo Marion (Editor-in-Chief), *National Research Council*
F. T. Rosser, Director, Division of Administration, *National Research Council*

Manuscripts for publication should be submitted to Dr. Léo Marion, Editor-in-Chief, Canadian Journal of Physics, National Research Council, Ottawa 2, Canada.
(For instructions on preparation of copy, see **Notes to Contributors** (inside back cover).)

Proof, correspondence concerning proof, and orders for reprints should be sent to the Manager, Editorial Office (Research Journals), Division of Administration, National Research Council, Ottawa 2, Canada.

Subscriptions, renewals, requests for single or back numbers, and all remittances should be sent to Division of Administration, National Research Council, Ottawa 2, Canada. Remittances should be made payable to the Receiver General of Canada, credit National Research Council.

The journals published, frequency of publication, and prices are:

Canadian Journal of Biochemistry and Physiology	Bimonthly	\$3.00 a year
Canadian Journal of Botany	Bimonthly	\$4.00 a year
Canadian Journal of Chemistry	Monthly	\$5.00 a year
Canadian Journal of Microbiology	Bimonthly	\$3.00 a year
Canadian Journal of Physics	Monthly	\$4.00 a year
Canadian Journal of Technology	Bimonthly	\$3.00 a year
Canadian Journal of Zoology	Bimonthly	\$3.00 a year

The price of single numbers of all journals is 75 cents.



Canadian Journal of Physics

Issued by THE NATIONAL RESEARCH COUNCIL OF CANADA

VOLUME 34

JUNE 1956

NUMBER 6

PARAMAGNETISM OF THE γ PHASE IN COPPER MANGANESE ALLOYS¹

By H. P. MYERS

ABSTRACT

Measurements of the paramagnetic susceptibility and its variation with temperature were made on a series of copper manganese alloys having compositions from 10 to 90 atomic per cent manganese. The measurements were confined to the temperature regions where the face centered cubic γ phase is known to be stable. The results show that alloys containing <25 atomic per cent manganese present a Curie-Weiss dependence of susceptibility on temperature, in agreement with earlier work. For compositions between 30 and 40 atomic per cent manganese the $1/\chi$ vs. T graph is linear at high temperatures but becomes increasingly curved at lower temperatures, the curvature being concave to the temperature axis. Alloys containing more than 60 atomic per cent manganese show a linear variation of $1/\chi$ with temperature but the change in χ , both with temperature and with composition, is slight. Alloys with 70 and 80 atomic per cent manganese show minima in the susceptibility at 900° and 950°C. respectively. An alloy with 90 atomic per cent manganese showed a continuous increase of susceptibility with temperature.

1. INTRODUCTION

The phase diagrams of the alloy systems manganese copper and manganese gold show wide ranges of composition and temperature over which the face centered cubic γ phase is stable. For dilute alloys of manganese in copper the γ form is stable at room temperature but for increasing manganese concentrations it becomes a high temperature phase. Even so for compositions up to 90 atomic per cent manganese the range of stability with respect to temperature is sufficient to allow the temperature dependence of the paramagnetic susceptibility to be determined.

A study of the γ phase offers considerable interest for, compared with the complex α and β modifications, the structure is simple. Measurements on copper manganese and gold manganese alloys should therefore provide data illustrating the paramagnetic behavior of a mid-transition group element suitable for comparison with that obtained on the end members of this group and in particular the nickel copper alloys of similar structure. This paper presents the results of measurements on the copper manganese system.

¹Manuscript received February 14, 1956.

Contribution from the Department of Mining and Metallurgy, The University of British Columbia, Vancouver, Canada.

2. EXPERIMENTAL PROCEDURE

The materials used were manganese of 99.9% purity donated by the Electro-manganese Corporation of America and copper with better than 99.99% purity obtained from Johnson Matthey Ltd.

The alloys were prepared in high grade alumina crucibles with the use of induction heating under an atmosphere of purified argon. The melts were chill cast under argon forming ingots of approximate dimensions 5 cm. \times 0.75 cm. diameter; these were then annealed *in vacuo* for seven days at a temperature appropriate to the composition to remove coring. From the center sections of the ingots were machined small right circular hollow cylinders of dimensions 2 mm. \times 6 mm. O.D. \times 2.75 mm. I.D. These were then given a short anneal. The ring specimens were suitable for the susceptibility measurements which were made using a Sucksmith (1929, 1938) ring balance. The force on the specimen was transmitted to the ring by a thin-walled quartz tube. The specimen was mounted in the following manner. At the end, remote from the ring, a circular groove was ground in the quartz tube; the specimen was slid over the tube and rested on a small clip made from a 1 cm. length of 0.3 mm. diam. molybdenum wire which fastened in the groove on the quartz tube. A platinum-platinum-rhodium thermocouple passed down the inside of the quartz tube and was arranged so that the junction was in line with the specimen. In the absence of a specimen this carrier assembly was diamagnetic and became increasingly so at high temperatures. Corrections for the deflection due to the carrier assembly at room and high temperatures were determined for all the field strengths used (up to 16,200 oersteds).

On account of the significant vapor pressure of manganese in the manganese-rich alloys high temperature measurements were made under a reduced atmosphere of argon. Any changes in sensitivity of the balance with temperature could be assessed using the deflection produced by a small weight (0.15 gm.) which could be added to the balance ring at will. Susceptibility values for the alloys were obtained by comparison with a standard nickel specimen prepared from Johnson Matthey nickel. The values of susceptibility for nickel determined by Sucksmith and Pearce (1938) were used for this calibration.

3. RESULTS

Nine alloys of composition from 10 to 90 atomic per cent manganese at increments of 10 atomic per cent were prepared. The actual compositions* of the alloys were determined by chemical analysis.

The results for each composition are shown in Figs. 1, 2, and 3. Each figure shows a different type of behavior. The susceptibility is referred to a gram of alloy and the values for the copper-rich alloys have been corrected to take into account the diamagnetic contribution of the copper.† This correction becomes

*All compositions are referred to atomic per cent.

†The value $\chi = -0.086 \times 10^{-4}$ was assumed for pure copper metal and a proportional correction was made for those alloys containing <40% Mn. This correction is probably appropriate for the copper since in these alloys the manganese core appears independent of the copper matrix. It is most likely that the manganese itself would contribute the greater diamagnetic effect owing to the large diameter of the incompletely filled $3d$ shell but an accurate estimate cannot be made; it was therefore omitted.

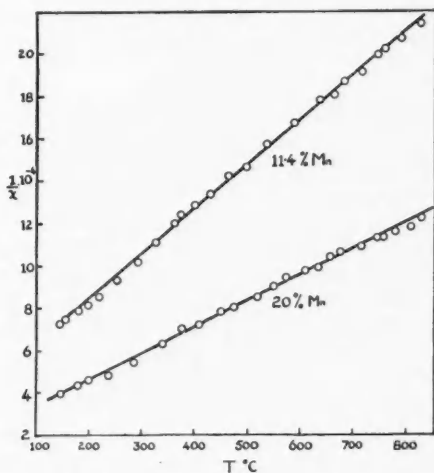


FIG. 1. $1/\chi$ against temperature for alloys containing 11.4 and 20% manganese. The units for χ are ergs oersted⁻² gm.⁻¹

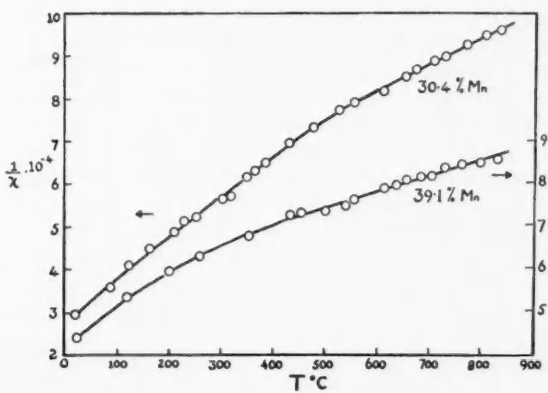


FIG. 2. $1/\chi$ against temperature for alloys containing 30.4 and 39.1% manganese.

insignificant for alloys containing $>40\%$ manganese. No allowance has been made for the diamagnetism of the manganese.

For alloys containing 11.4 and 20% manganese and within the accuracy of the results, $1/\chi$ varies linearly with T showing a Curie-Weiss behavior. The 30.4 and 39.1% manganese alloys have a $1/\chi$ vs. T curve showing pronounced

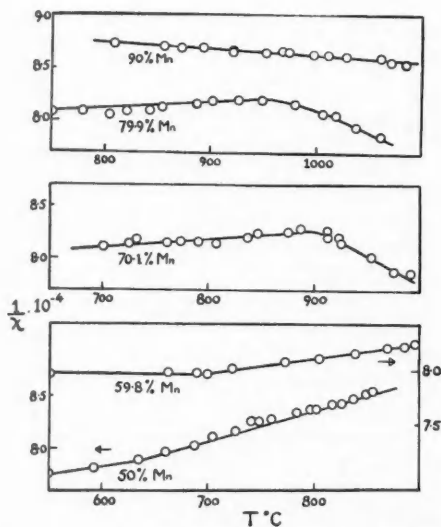


FIG. 3. $1/\chi$ against temperature for alloys containing 50, 59.8, 70.1, 79.9, and 90% manganese. The scale of the ordinate is the same for all the graphs, which have been displaced to avoid confusion. The change in temperature intervals should also be noticed.

curvature concave to the T axis although above 500°C . the graphs become linear. For a given temperature there is a significant increase in susceptibility with an increase in manganese content from 11.4 to 39.1%. For greater Mn contents the susceptibility for a given temperature remains almost unchanged and in fact for a given composition there is little variation with temperature. However the variation of $1/\chi$ with T although slight is evident, and whereas it is perhaps no longer significant to plot $1/\chi$ against T this has been done to preserve the sequence of the results.

For the 50 and 59.8% manganese alloys $1/\chi$ varies linearly with T and the slopes of the graphs continue to decrease. This aspect is maintained in the 70.1 and 79.9% alloys but an added feature is the maximum that appears in the graph, indicating that the susceptibility for these alloys begins to increase at approximately 900°C . and 950°C . respectively. The alloy containing 90% manganese shows a susceptibility which increases with temperature.

In connection with the results a further point concerning the stability of the γ phase in these alloys may be mentioned. For manganese contents $>20\%$ the γ phase may be retained at room temperature and it is noteworthy that the 30.4 and 39.1% alloys show no discontinuity in the variation of $1/\chi$ with T . The 50 and 59.8% did show an abrupt change in slope of the $1/\chi$ vs. T graph at temperatures which correspond closely to the position of the phase boundaries indicated on the phase diagram. For this reason measurements were only

made in the high temperature region of stability of the γ phase for alloys with manganese contents $>39.1\%$.

4. DISCUSSION

The present work supplements that of Néel (1932), Gustafsson (1936), and Valentiner and Becker (1933). The two former authors measured the properties of dilute alloys ($\text{Mn} < 5\%$) and obtained results showing that at vanishingly small concentrations of manganese in copper the manganese had a $p_{\text{eff}} = 4.85$ indicating a probable $3d_5 4s_1$ configuration.

Furthermore their results indicate that p_{eff} increases from 4.85 to 5.5 as the manganese content increases from vanishingly small to 5% . Néel also measured the properties of two alloys with greater manganese contents. Valentiner and Becker studied compositions up to 80% but their measurements were made in the temperature range 20° to -183°C . Thus for the higher manganese contents their data represent the properties of mixed phases. However, for compositions in the range 5 – 20% manganese, the results presented here agree well with those of Néel and Valentiner and Becker although the three sets of measurements were made over quite different temperature ranges.

In Fig. 4 are plotted the p_{eff} values at different compositions. The p_{eff} number has significance only at low manganese contents but since our measure-

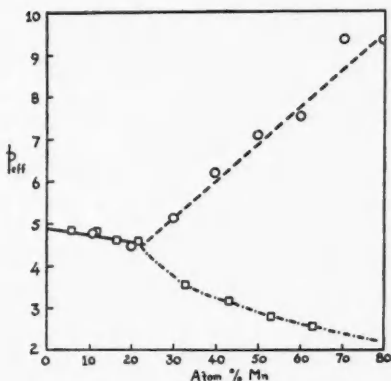


FIG. 4. Values of p_{eff} for manganese copper alloys. Values calculated from the work of Valentiner and Becker are also plotted (\square) for comparison; these were determined from measurements made below room temperature.

ments have shown $1/\chi$ to vary linearly with temperature for all compositions studied, we have calculated values for the higher manganese alloys. It should be emphasized that this is done only as a means for comparing the properties of the dilute alloys ($<20\%$) with those alloys with higher manganese contents; in these latter instances p_{eff} is merely a parameter proportional to the reciprocal of the gradient of the $1/\chi$ vs. T graph and has no other significance. It will

be seen from Fig. 4 that the 'dilute' alloys containing between 5 and 20% manganese show a simple behavior, p_{eff} decreasing slightly with increasing manganese content. We have drawn a straight line through these points so that the intercept on the ordinate corresponds to $p_{\text{eff}} = 4.9$, the value expected for manganese in a $3d_64s_1$ configuration possessing spin moment only.

For compositions greater than 20% manganese the p_{eff} values determined in this work increase sharply with increasing manganese content; this is in direct contrast with those values determined by Valentiner and Becker which continue to decrease. This divergence can be partly explained by the pronounced curvature found in our $1/\chi$ vs. T graphs for the 30.4 and 39.1% alloys, for since Valentiner and Becker made measurements only at low temperatures the gradients of their graphs would be larger than those we measured at high temperatures and therefore result in lower values of p_{eff} . The difference between the two sets of results at higher manganese contents can be attributed to the presence of a second phase in the alloys of Valentiner and Becker, a fact which they acknowledge in their paper.

Thus the measurements show that alloys containing less than about 25% manganese present a different type of behavior from those with greater concentrations and it is significant that the neutron diffraction data of Meneghetti and Sidhu (1954), which were recently brought to our notice, showed short range magnetic ordering to occur in these alloys and to have a maximum effect at about 50 atomic per cent manganese. The present data are however restricted to the regions where $1/\chi$ varies linearly with temperature and are valid for temperature ranges well above any antiferromagnetic critical temperatures found by Meneghetti and Sidhu.

The behavior of the alloys containing 70.1 and 79.9% manganese is complicated by the fact that above certain temperatures the susceptibility increases with increasing temperature. For these high manganese content alloys the change in susceptibility can be observed easily but the variation being small it is not possible to define the gradients of the graphs accurately. It is also noteworthy that the alloy containing 90% Mn has a susceptibility with a positive temperature coefficient in contrast to the existing data for pure γ manganese.

Subject to the fashion in which the results are displayed in Fig. 4, the most striking feature is the apparent change of properties occurring at manganese concentrations around 20-25%. Below this concentration the results admit of a simple interpretation in that the manganese can be considered monovalent—the tendency being to maintain a concentration of 4s electrons similar to that for pure copper. The 3d electrons of the manganese appear to remain localized on the atoms and thus give rise to a moment characteristic of the $3d_64s_1$ configuration. For alloys containing more than 25% manganese it is clear from the large apparent p_{eff} values calculated from the slopes of the $1/\chi$ vs. T graphs that a different electronic arrangement must exist.

If we choose to consider the variation of susceptibility, appropriate to a particular temperature, with composition a smooth change is found. This is illustrated in Fig. 5 where the value of susceptibility at 800° C. for each alloy is plotted against composition. It is seen that the susceptibility increases

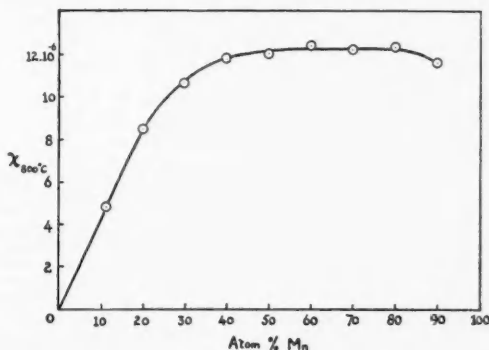


FIG. 5. The variation of susceptibility measured at 800°C. with composition of alloy.

rapidly with initial addition of manganese to copper but the susceptibility is almost independent of composition for manganese contents greater than 40%. On account of the very slight temperature variation of susceptibility that has been found this result would also remain true at other temperatures.

It seems that such behavior can only be understood if it is assumed that in this composition range the 3*d* electrons of copper and manganese form a common 3*d* band. The approximate constancy of the susceptibility for different alloy compositions would then imply an approximate constancy of the density of 3*d* energy states with electron concentration. Thus if for convenience we assume that there is one 4*s* electron per atom of alloy it is required that no change in the density of energy states in the 3*d* band should occur for 3*d* electron concentrations lying between 6.8 and 8.4 electrons per atom of alloy. Such behavior is in keeping with the suggested shapes for the 3*d* band of transition metals which invoke sharp maxima in the density of states at the beginning and end of the band but require these maxima to be separated by a region of constant or slowly varying density of states. Thus the change in properties which occurs at about 25% manganese content can be associated with the transition from localized states for the 3*d* electrons of the manganese atoms to collective electron treatment of these electrons for the atoms of the alloy. It is to be noted that such a change is more accurately defined by the change in the temperature variation of the susceptibility with composition rather than the variation of the susceptibility, measured at some arbitrary temperature, with composition.

ACKNOWLEDGMENTS

The author wishes to acknowledge the contribution of Mr. R. G. Butters who prepared the alloys and performed the chemical analysis. This work was carried out with the support of the Defence Research Board of Canada under Grant D.R.B. 281, project number D44-95-35-02. The support of the National Research Council is also gratefully acknowledged.

REFERENCES

- GUSTAFSSON, G. 1936. *Ann. Physik*, **25**: 545.
MENEGHETTI, D. and SIDHU, S. S. 1954. Argonne Natl. Lab. Rept.
NÉEL, L. 1932. *J. phys.* **3**: 160.
SUCKSMITH, W. 1929. *Phil. Mag.* **8**: 158.
SUCKSMITH, W. and PEARCE, R. R. 1938. *Proc. Roy. Soc. A*, **167**: 189.
VALENTINER, S. and BECKER, G. 1933. *Z. Physik*, **80**: 735.

THE DURATION OF FORWARD-SCATTERED SIGNALS FROM METEOR TRAILS¹

BY P. A. FORSYTH AND E. L. VOGAN

ABSTRACT

The durations of radio signals obtained by forward scattering from meteor trails have been determined by direct measurement, using moving chart, amplitude recordings. The recordings were made simultaneously at two frequencies and similar measurements were made on signals received over two transmission paths in western Canada. The durations of signals observed over an east-west path appear to be greater than those observed over a north-south path. The observed dependence of duration upon both wavelength and equipment sensitivity is compared with that found previously by McKinley for back-scattered signals. Effects similar to those found by McKinley are present in the forward-scatter data. The method used to record the signals makes possible a more detailed examination of these effects. While the dependence of duration upon equipment sensitivity seems to be in accord with the presently accepted theories of meteor scattering, the dependence upon wavelength is not yet completely understood.

INTRODUCTION

The relation between the duration of radar (back-scatter) echoes from meteors and the radar equipment parameters has been investigated experimentally by McKinley. While existing theoretical models predicted that the echo duration would be independent of equipment sensitivity, McKinley (1953a) found that echoes which were observed with high power equipment lasted longer than did the corresponding echoes observed simultaneously with low power equipment, and also that the ratio of the echo durations for the two systems varied with duration. Furthermore, while it was expected on theoretical grounds that the echo duration would be proportional to the square of the wavelength, McKinley (1953b) found that the ratio of durations on two wavelengths varied with duration and deviated significantly from the square law value. This latter result is perhaps the more interesting because it appears to be related more directly to the physical behavior of the meteor trail after its formation. The predicted square law relation between duration and wavelength is based upon the assumption that diffusion alone controls the decay of meteor echoes. In fact, of course, it is known that the trails must be distorted by winds and that recombination and attachment processes must contribute also to the reduction of the volume density of free electrons within a trail. These effects are likely to be more significant for the echoes of longer duration.

Because of the nature of the scattering mechanism, the forward-scattered signal from a meteor trail should always be of greater duration than the corresponding back-scatter echo (Eshleman 1952; Eshleman and Manning 1954). It is reasonable, therefore, to expect that the anomalies found by McKinley would be even more apparent in similar measurements made on forward-scattered signals. This paper discusses the results of an experiment

¹Manuscript received February 22, 1956.

Contribution from the Radio Physics Laboratory of the Defence Research Board, Ottawa, Canada. The work was performed under project PCC No. D48-28-35-05.

which involved the reception of forward-scattered meteor signals simultaneously at two frequencies, the measurements being made concurrently over two nearly orthogonal paths in western Canada.

EXPERIMENTAL ARRANGEMENT

The transmission circuits which were used for the experiment are those designated as 5, 6, 7, and 8 of Table I in an earlier paper (Forsyth and Vogan 1955). The transmitters for these circuits operate on frequencies of 38.06 Mc./s. and 49.98 Mc./s. and are located at Winnipeg, Manitoba. One set of receiving equipment is located approximately 1000 km. to the west (Ralston, Alberta) and another set about the same distance to the north (Churchill, Manitoba). For this experiment, new antenna arrangements were used which provided the same antenna gain for each frequency. The recording equipment was similar to that used to record the individual signals shown in Fig. 3 of the earlier paper. The records were made during the period 25 January to 2 February, 1955.

Every effort was made to ensure that the recordings were as reliable as possible. The transmitters were attended continuously during the recording periods and the sensitivity of each receiving system was calibrated at least once before or during each high speed recording period. High speed records (with a recording chart speed of 10 or 25 mm./sec.) were taken as often as was convenient during the daylight hours. Later, the records were examined carefully and for this analysis all those records were discarded in which there was any evidence of drift in the receiving and recording equipment or any indication of faulty calibration. The days on which good records were obtained are listed in Table I together with the times of the earliest and latest records

TABLE I

Place	Date	Recording intervals	No. of signals recorded
Ralston	25 Jan.	1100-1600 M.S.T.	219
	26 Jan.	1310-1500	127
	27 Jan.	1450-1600	56
	31 Jan.	1020-1400	202
			604
Churchill	27 Jan.	0950-1010 C.S.T.	30
	28 Jan.	1000-1540	301
	31 Jan.	0930-1200	234
	1 Feb.	0930-1445	406
	2 Feb.	0930-1300	220
			1191

on each day; recording was by no means continuous between these two times. The number of individual signals which were clearly resolved on the selected records is also listed. This number refers specifically to the record for the higher frequency; in general, a signal at 49.98 Mc./s. was accompanied by one at 38.06 Mc./s. It was not, however, always possible to make accurate measure-

ments of signals which appeared simultaneously at the two frequencies because one or other of the records was sometimes partially obscured by interference or by neighboring meteor signals.

The signals were analyzed initially with regard to amplitude and duration. The amplitude of each signal was measured and the signal assigned to one of ten logarithmically related amplitude classes. The duration was measured at a level which was $1/e$ of the maximum amplitude. It should be noted that the photographic method of recording used by McKinley permitted only the measurement of duration above a fixed level, namely the threshold level of the recording system. In the present paper this threshold duration measured at a fixed sensitivity level will be designated by T whereas the duration measured at a level which is $1/e$ of the maximum amplitude will be designated by D . Durations measured at a frequency of 49.98 Mc./s. will be indicated by D_6 and those for 38.06 Mc./s. by D_8 (the subscripts refer to the wavelength). The theoretical relations mentioned earlier were intended to apply strictly to the measurements of D and not to those of T .

COMPARISON OF DURATIONS FOR THE TWO PATHS

The results of the first analysis are summarized in Table II. The most striking feature of the results is the significant difference between the signals measured at Churchill and those measured at Ralston. The fact that the

TABLE II

	Recording station			
	Ralston	Ralston	Churchill	Churchill
Frequency, Mc./s.	49.98	38.06	49.98	38.06
No. of signals	561	438	1029	865
Duration D , sec.: Mean	1.425	2.370	1.180	1.737
Median	0.55	1.05	0.45	0.67
Mode	0.30	0.60	0.30	0.35
D_8/D_6 Mean		1.859		1.547
Median		1.72		1.38
Mode		1.9		1.30

recording equipments used on the two frequencies were interchanged during the recordings at both stations and that the receiving equipments were calibrated frequently makes it unlikely that the observed difference between the two paths is instrumental. The durations measured at Ralston for both frequencies are significantly greater than those measured at Churchill. The ratio of the durations at the two frequencies is also greater for the Ralston measurements. For the sake of comparison it may be noted that if duration were proportional to the first power of wavelength the ratio D_8/D_6 would have the value 1.31, whereas if duration were proportional to the square of wavelength this ratio would have the value 1.72.

The recordings at the two stations were not always made simultaneously and even if it had been possible to make them simultaneously the records would not, of course, refer to the same meteors. On the other hand, the record-

ings for each day were examined separately and there did not appear to be any significant changes in the characteristics of the signals from day to day, so that the lack of exact simultaneity between the records from the two stations can scarcely explain the observed differences.

The recent theoretical treatment of meteor "observability" given by Hines (1955) points out the importance of observational selection in the measurements of the forward-scattered signals from meteors. This selection certainly operates differently for the two circuits. For example, the Churchill path is relatively insensitive to meteors which come from regions of the sky near the plane of the ecliptic. On the other hand, the Winnipeg-Ralston path is quite sensitive to such meteors. Another important difference between the two circuits involves the earth's magnetic field. On the east-west path many meteors are detected which lie very nearly along the lines of force of the magnetic field, whereas for the north-south path most of the meteor trails which are detected make angles with the direction of the magnetic field greater than 37° . The diffusion of ionization at meteoric heights proceeds more rapidly along lines of magnetic force than at right angles to them. For this reason one would expect the observed durations to be greater for the Ralston measurements than for those made at Churchill. Further experiments are required in order to determine if the effect of the magnetic field is sufficiently great to produce the observed differences between the two paths.

THE DEPENDENCE OF DURATION UPON WAVELENGTH

In order to indicate more clearly the dependence of duration upon wavelength a scatter diagram in which the common logarithm of D_8 is plotted against the common logarithm of D_6 is shown in Fig. 1. Each experimental point represents the two signals which were observed simultaneously on the two frequencies at Ralston. The straight line representing the theoretical relation

$$R \equiv D_8/D_6 = (\lambda_8/\lambda_6)^2,$$

where λ is the wavelength, is also drawn on the same diagram. The experimental points are nicely distributed about the theoretical line but the scatter is large.

It was pointed out earlier that the measurements made by McKinley were durations above a fixed threshold level and not durations measured at a level which was some fraction of the maximum amplitude of the signal. In order to provide a more direct comparison of the present results with the back-scatter measurements, the Ralston durations were measured again, this time at a fixed sensitivity level corresponding to a receiving antenna voltage of 0.25 microvolts. A scatter diagram of the results, in which T_8 is plotted against T_6 , is given in Fig. 2. The general trend is very similar to that in the previous figure but it is evident that the threshold measurements do not fit the theoretical line as well as did the relative duration measurements of Fig. 1.

It may be suggested reasonably that the lack of fit between the experimental points and the theoretical relation in Figs. 1 and 2, and also the large scatter

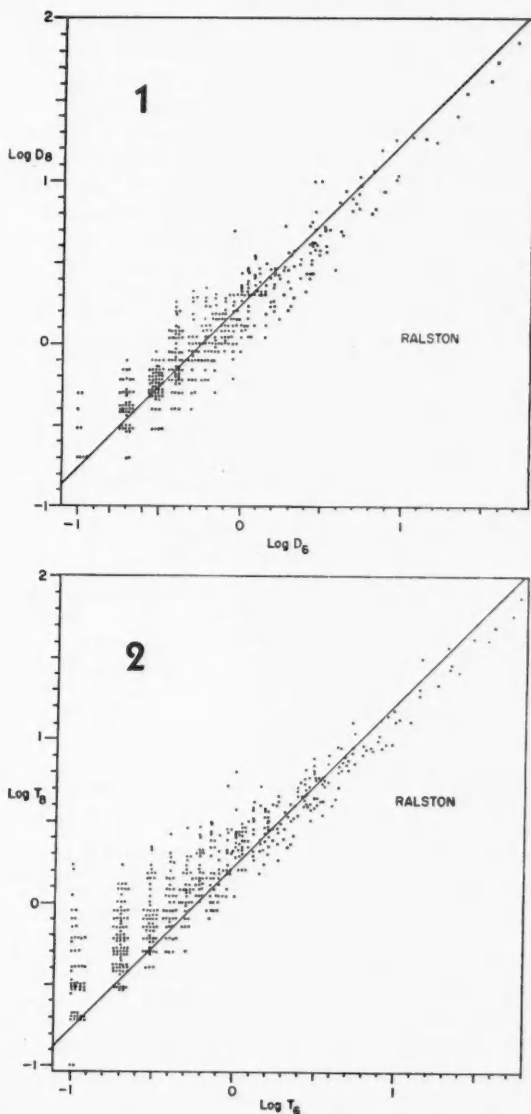


FIG. 1. Scatter diagram of the relative durations of meteor signals (measured at an amplitude which is $1/e$ of the maximum) received at a frequency of 38.06 Mc./s. (D_3) plotted against the durations of the corresponding signals received at a frequency of 49.98 Mc./s. (D_4). The solid line represents the relation $D_3/D_4 = (\lambda_3/\lambda_4)^2$.

FIG. 2. Scatter diagram of the threshold durations (measured at a fixed sensitivity level) for the signals shown in Fig. 1.

in the experimental points, is due entirely to the occurrence of fading in the meteor signals. This argument follows from the fact that the probability of occurrence of fading in a signal is a function of the duration of the signal, increasing with increasing duration. The presence of fading then introduces an uncertainty into the measurement of duration and at the same time imposes a bias on the measurements. In order to test this suggestion, the Ralston data were re-examined and signals were selected which exhibited the rapid rise and exponential fall of amplitude characteristic of the underdense trail, and which also exhibited no fading (see Fig. 2(a) of the earlier paper, Forsyth and Vogan 1955). A scatter diagram of the relative durations $D(S)$ of these selected signals at the two frequencies is given in Fig. 3. With the exception of those

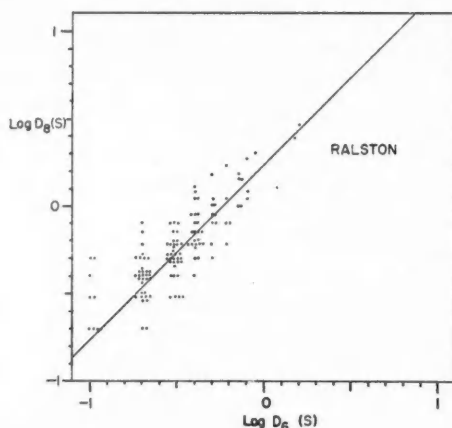


FIG. 3. Scatter diagram for relative durations of a group of selected signals which decayed exponentially with time and showed no fading.

signals with $D_6(S)$ equal to 0.1 sec.—a value which is subject to considerable experimental error—the fit with the theoretical line is quite good. The agreement with the theoretical line may, in fact, be slightly better than that of Fig. 1, but the scatter is still large. It is necessary, therefore, to conclude that the anomalous behavior of the observed durations is not due simply to the occurrence of fading in the signals.

In his investigation McKinley applied a particularly sensitive test to the data in order to reveal the departure of the experimental data from the square law of wavelength. He divided the pairs of measurements at the two frequencies up into classes according to the duration recorded at the shorter wavelength. For each class the mean value of the logarithm of the ratio, R , of the durations at the two wavelengths was plotted as an ordinate against the mean logarithm of duration at the shorter wavelength as abscissa. On such a graph the square law of wavelength can be represented by a horizontal straight line. The present data are shown plotted on this type of graph in Fig. 4.

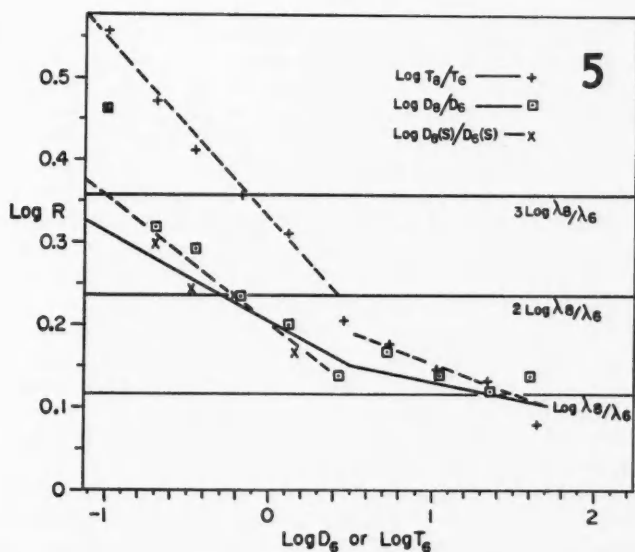
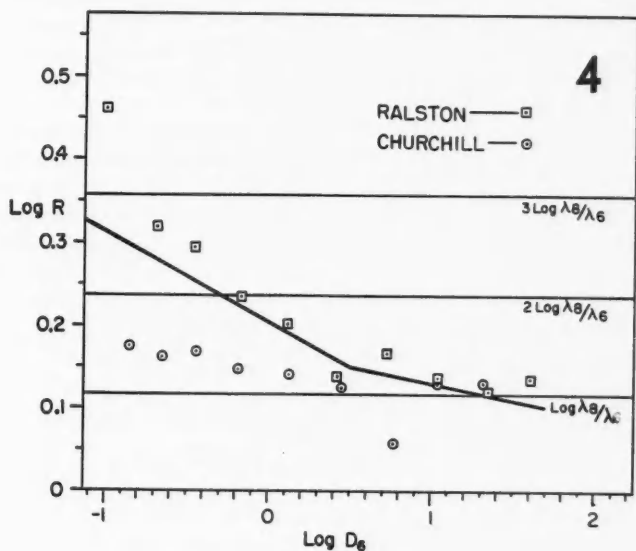


FIG. 4. Graph of the mean logarithm of the ratio $D_5/D_6 = R$ against the mean logarithm of D_6 , the measurements being grouped by class interval of D_6 . The solid lines have the slopes predicted by the empirical relations found by McKinley (1953b).

FIG. 5. The data of Figs. 1, 2, and 3 replotted after the manner of Fig. 4.

The duration class intervals used for the figure are the same as those used by McKinley (1953b). The two slanting lines in the figure are drawn with the slopes predicted by the empirical relations given by McKinley,

$$(1) \quad \log R = (1.0 - 0.796p)(2.0 - \log D_\lambda)$$

for the left-hand side of the graph, and

$$(2) \quad \log R = (1.0 - 0.921p)(5.4 - \log D_\lambda)$$

for the right-hand side, where $p = 4.23 \log \lambda_a/\lambda_b + 0.333 x$, and x is the logarithm of the sensitivity ratio (zero for the present measurements). The lines drawn in Fig. 4 have only the slopes and not the positions given by these relations. The positions of the lines were adjusted arbitrarily to fit the data. The marked differences between the Ralston and Churchill measurements are evident again in this figure. The points for the Churchill data lie nearly on a horizontal line with a value of R which is intermediate between that required by a first power law and that required by a square law of wavelength. On the other hand, the Ralston results are consistent with the bilinear characteristic predicted by equations (1) and (2).

In Fig. 5 the data of Figs. 1, 2, and 3 are shown plotted after the manner of Fig. 4. The straight solid lines of this figure are the same as those of Fig. 4. The most striking characteristic here is that while the points on the right-hand side of the diagram can be adequately represented by a single line (for example, the broken line of the figure), points on the left-hand side require two such lines. It appears that for the longer durations it does not much matter whether the measurements refer to the relative duration D or to the threshold duration T , whereas for shorter durations this distinction is important. This behavior is consistent if the left-hand side of the graph is considered to refer to signals from underdense trails, which decay exponentially, while the right-hand side refers to signals from overdense trails which persist for some time at constant amplitude and then decay suddenly. The data for the durations, $D(S)$, of the selected signals which are known to be of the exponential type follow very closely those for all the shorter duration signals. This evidence seems to confirm McKinley's suggestion that the discontinuity of slope actually corresponds to the transition from underdense to overdense trails.

It is interesting to examine the actual value of the durations at which the discontinuity of slope takes place. The empirical equations (1) and (2) which were derived from back-scatter measurements predict (for the present wavelengths) that this discontinuity should occur when $\log D_e$ is equal to zero. In fact, from Fig. 5 this discontinuity seems to occur in the neighborhood of $\log D_e = 0.5$. As a first approximation it is reasonable to suppose that this shift is due simply to the increase in duration of the signals from underdense trails. The ratio of the durations of the forward- and back-scattered signals from underdense trails has been predicted by Eshleman and Manning (1954):

$$D_F/D_B = \sec^2 \phi,$$

where ϕ is the forward-scattering angle. Taking

$$\log D_F/D_B = 0.5$$

and solving for ϕ , a value of about 57° is obtained. The value of ϕ which is

appropriate to the region of highest "observability" for a path which is 1000 km. in length is about 72° , but many meteors should be observed for which ϕ is considerably less than this value.

It has been suggested that the particular characteristics found by McKinley were due, in part, to the method of plotting the results. The present results do not support this suggestion. While it is reasonable to doubt the accuracy of the sensitive tests of Figs. 4 and 5 when used on data which are as widely scattered as those of Figs. 1, 2, and 3, the characteristics deduced from Fig. 5 are evident, at least qualitatively, from a close inspection of the earlier figures. Since the scatter diagrams contain relatively raw data, there is no reason to believe that these effects are spurious.

THE DEPENDENCE OF DURATION UPON SENSITIVITY

In order to investigate the variation of duration with sensitivity the records for the lower frequency (38.06 Mc./s.) were examined again. For this analysis the duration of each signal was measured at two fixed threshold levels, corresponding to antenna voltages of 0.4 and 1.6 microvolts, a sensitivity difference of 12 db. The duration measured at the high sensitivity level (0.4 microvolts) is here indicated by T_h and that for the low sensitivity level (1.6 microvolts) by T_l . In Fig. 6 the mean logarithm of the ratio $R = T_h/T_l$ is plotted against

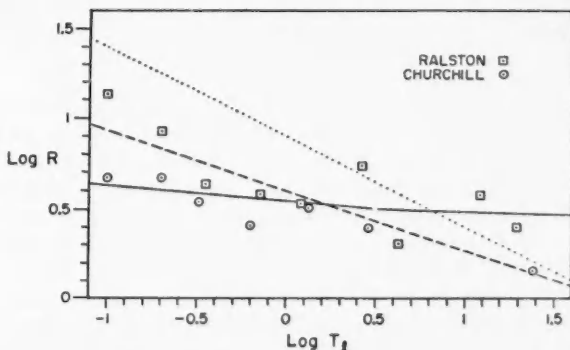


FIG. 6. Graph of the mean logarithm of the ratio, R , of the durations measured at high and low sensitivity levels against the mean logarithm of the duration at the low sensitivity level (T_l).

the mean logarithm of T_l for the same duration intervals as were used earlier. Although there were only 72 suitable signals measured at Ralston and 80 at Churchill the results seem to show a general trend of the kind found by McKinley (1953a). The solid lines on the graph have the slopes (but not the positions) predicted by equations (1) and (2). Once again, the slower decay of the signals at Ralston is indicated, although not as clearly as in Fig. 4. While the scatter of experimental points is too great to permit an assessment of the accuracy with which either set can be represented by a formula of the kind given by McKinley, the general decrease of the mean logarithm of R with increasing T_l seems to be real.

It is interesting to consider the apparent trend of the observations of Fig. 6 in relation to the known characteristics of the signals. It is inherent in the method of measurement that T_l cannot exceed T_h for any given signal so that there is a constant lower boundary to the possible values of $\log R$ for all values of T_l , namely zero. On the other hand, it is known from the observations themselves that the occurrence of signals having durations greater than, say, one minute is extremely rare. We may, for present purposes, impose a practical upper limit upon the values of $\log T_h$ and $\log T_l$ somewhere in the neighborhood of 1.8. On a graph of the kind shown in Fig. 6 this upper bound could be represented by a sloping line having the equation

$$(3) \quad \log R = 1.8 - \log T_l.$$

It is clear that if there is any variation in R for a given value of T_l , then the presence of the two boundaries will cause a decrease in the mean value of $\log R$ with increasing $\log T_l$. A simple assumption is that, for a given value of $\log T_l$, all values of $\log R$ between zero and that given by equation (3) are equally probable. In this case the mean value of $\log R$ for each value of T_l is just half that indicated by equation (3). These values are plotted in Fig. 6 as the dotted line. Another simple, but more reasonable, assumption which agrees qualitatively with the observations is that, for a given value of T_l , the probability of occurrence of any value of $\log R$ is greatest for $\log R = 0$ and decreases uniformly to zero as $\log R$ approaches the upper bound set by equation (3). For this case the mean value of $\log R$ is given by the equation

$$\log R = 0.60 - 0.33 \log T_l,$$

which is plotted in Fig. 6 as the broken line. To the order of accuracy permitted by the statistical variation of the observations, this equation can be said to fit the experimental points. Clearly, there is no justification in the present measurements for attempting any more refined analysis. This discussion will serve to indicate that the general trend shown in Fig. 6 follows directly from observable characteristics of the signals, namely, a wide variation in the values of R associated with a particular value of T_l , and a practical upper limit to the observed values of duration. The first of these characteristics is due to variations in the rate of decay of different meteor signals. In the case of back-scattered signals it is known (Greenhow and Neufeld 1955) that variations in the height at which different meteor trails are formed causes a large variation in the rate of decay of signals. For forward-scattered signals there is an additional variation introduced by the occurrence of widely differing values of the forward-scattering angle, ϕ . The second characteristic is also reasonably well understood. For the long-enduring signals the duration is proportional to the line density of ionization in the meteor trail. It is well known (see, for example, McKinley 1951) that the probability of occurrence of a meteor trail decreases rapidly with increasing values of initial ionization density. In addition to this effect, there is reason to believe (Kaiser 1953) that there is an ultimate limit to the observable duration of meteor signals which is set by the disappearance of the ionization through recombination and attachment processes.

CONCLUDING REMARKS

It appears from the present measurements that the general dependence of the duration of forward-scattered signals from meteor trails upon both wavelength and equipment sensitivity is similar to that found by McKinley for back-scattered signals. In the case of the wavelength dependence, the use of moving chart records has permitted the analysis of the signals by several different methods which, together, have revealed more clearly the roles of underdense and overdense meteor trails. These methods of analysis have also revealed systematic differences between durations measured at a fixed threshold level and those measured at a value which is $1/e$ of the maximum amplitude of each signal. It is important that the latter method of measurement be used in preference to the former whenever the durations are to be used for comparison with the present theory. This is particularly true for the signals of shorter durations. If this relative duration (D , in the preceding text) is used, then it is, inherently, independent of the equipment sensitivity. In any case, the behavior of the threshold durations measured at different sensitivity levels seems to be in accord with the present understanding of the characteristics of the meteor trails. Unfortunately the comparative measurements at two frequencies are not so well understood. It has been suggested by Eshleman (1955) that the low observed value of the exponent in the duration-wavelength relation for the longer durations is due to departures of the actual shape of the trails from the assumed cylindrical form. The duration of the signal from a spherical overdense cloud of ionization is proportional to the four-thirds power of wavelength. While this mechanism may contribute to the observed effect for the long enduring signals, it cannot be used to explain the results derived from the selected signals which are known to be of the kind usually associated with underdense trails. For underdense clouds Eshleman predicts that the duration of the signals should be proportional to the square of the wavelength even when the clouds are spherical in shape.

The significant differences in signal characteristics which were found between the signals recorded at Churchill and those recorded at Ralston are, as yet, unexplained. Further investigation of these differences is required.

ACKNOWLEDGMENTS

The authors are indebted to Mr. J. Orosz who assisted with the recordings made at Ralston, and to Dr. L. L. Campbell and Mr. D. R. Hansen who measured the durations used in Fig. 6. During the recording periods the transmitters at Winnipeg were attended by Mr. C. Collins.

REFERENCES

- ESHLEMAN, V. R. 1952. Tech. Rept. No. 49, Electronics Research Lab., Stanford University.
——— 1955. Trans. Inst. Radio Engrs. (PGAP), **AP-3**: 32.
ESHLEMAN, V. R. and MANNING, L. A. 1954. Proc. Inst. Radio Engrs. **42**: 530.
FORSYTH, P. A. and VOGAN, E. L. 1955. Can. J. Phys. **33**: 176.
GREENHOW, J. S. and NEUFELD, E. L. 1955. J. Atm. and Terrest. Phys. **6**: 133.
HINES, C. O. 1955. Can. J. Phys. **33**: 493.
KAISER, T. R. 1953. Advances in Phys. **2**: 495.
MCKINLEY, D. W. R. 1951. Can. J. Phys. **29**: 403.
——— 1953a. Can. J. Phys. **31**: 758.
——— 1953b. Can. J. Phys. **31**: 1121.

DIFFRACTION OF 3.2 CM. ELECTROMAGNETIC WAVES BY DIELECTRIC RODS

I. LUCITE AND TENITE 1 IN. DIAMETER CYLINDERS¹

BY M. K. SUBBARAO² AND A. B. McLAY

ABSTRACT

Diffraction patterns of lucite and tenite cylindrical rods of approximately one inch diameter, in a nearly plane beam of square-wave modulated 3.2 cm. waves with electric vector parallel to the cylinder axis, have been measured in several planes transverse to the incident beam direction. Patterns are compared with theoretical ones (Froese and Wait 1954) and with ones obtained earlier, under similar experimental conditions, for brass and hard rubber cylinders (Wiles and McLay 1954). Some general marked trends in the patterns of the four rods, comprising a conductor, two nearly lossless dielectrics with different dielectric constants, and a lossier dielectric, are related to the effects of transmission and/or surface reflection expected from geometrical optics considerations.

1. INTRODUCTION

Diffraction patterns of a brass tube and a hard rubber rod were reported in a previous communication (Wiles and McLay 1954). Each was a cylinder of length 6 ft. and diameter 1 in. (2.54 cm.). Observations were made with each cylinder placed in a nearly plane beam of square-wave modulated 3.2 cm. waves, with electric vector parallel to the cylinder axis. Experimental patterns for the brass cylinder agreed quite closely with theoretical ones. Similar measurements have now been made using nearly lossless dielectric rods of lucite and tenite of approximately 1 in. diameter. Results for the four cylinders are compared.

Preliminary measurements on the lucite cylinder were sent to Dr. J. R. Wait of the Defence Research Board of Canada Telecommunications Laboratory, at his request. Froese and Wait (1954) calculated corresponding patterns, using theoretical equations derived by them, and compared the experimental and theoretical curves. They had also calculated patterns for a 1 in. diameter tenite cylinder, taken as a nearly lossless equivalent of our hard rubber one. They kindly sent us the tenite rod used in our present experiments. Results on this, as presented here, were sent to them but not in time to be included in their paper except by footnote, indicating fair agreement with their calculated curves.

Observations of diffraction of 1.25 cm. waves by polystyrene cylinders were made earlier by Kodis (1952). Patterns were obtained in two planes only for each of two cylinders of diameters 2λ and 4λ . Froese and Wait (1954) compared one of these four patterns with the theoretical one. Diffraction of 10 cm. waves by a tenite cylinder has been investigated recently by Keys (1955) and compared with calculated results.

The completed results of our measurements of diffraction by lucite and

¹Manuscript received January 31, 1956.

Contribution from the Department of Physics, Hamilton College, McMaster University, Hamilton, Ontario.

²Present address: Junior Scientific Officer, Indian Naval Physical Laboratory, Cochin, India.

tenite cylinders are reported in this paper. The present results for lucite, obtained subsequent to sending preliminary measurements to Froese and Wait, were made under improved experimental conditions and show better agreement with calculated patterns.

2. APPARATUS

The general arrangement of apparatus for the free-field diffraction observations is similar to that described earlier (Wiles and McLay 1954). The experiments were performed in the same location as before in a large laboratory, 75 ft. long and 25 ft. wide, with source at one end and beam directed toward the distant, far end of the room. The distance between the source, of nearly cylindrical waves, considered to be at the geometrical apex of the transmitting horn, and the probe when on the axis of propagation was 615 cm. as in the earlier work. The probe was a IN23A crystal diode with most of the brass cut away to approximate a symmetrical dipole.

A number of changes in the apparatus have been made, however: (a) The rectangular *H*-plane brass horn was replaced by an aluminum pyramidal one, with same axial length 80 cm. from center of square mouth to geometrical apex, same flare angle 20° in the *H*-plane, and about the same flare in the *E*-plane to fit the *E*-plane dimension of the RG52/U wave-guide feed line from the 723A/B klystron source. The axis of propagation was horizontal and the field vertically polarized as before. (b) The original broad band a-c. amplifier, with output to recorder clamped by a diode, was replaced by a narrow band amplifier with twin-T feedback, tuned to the 800 cycle/second fundamental frequency of the square-wave modulation. A vacuum tube voltmeter type coupling to the Brown Potentiometer recorder provided much more stable operation than formerly, elimination of much of the noise and parasitic oscillations of the original unit, and more stable simplified control of the input to the recorder. Good linearity of amplifier output was obtained in the gain range up to 50,000 as used. (c) The original drum and string drive of the probe carriage on the optical bench track was replaced by a long lead screw, driven by a $\frac{1}{8}$ h.p. synchronous motor and a Boston 1:100 reduction gear. This provided more positive and uniform drive than formerly and the probe carriage could be moved in either direction along the track.

In the earlier observations with brass and hard rubber cylinders and in the present ones, all diffraction patterns showed some asymmetry, the right side as seen looking toward the source being always more extended than the left. A number of variations in orientation of the axes involved, of source horn, propagation, probe run, and probe crystal, were tried in attempts to reduce or eliminate this effect. While the asymmetry varied a bit under different conditions, in no case was it reduced to a negligible amount or was a reversed asymmetry observed. It was concluded that the effect was an asymmetry in the incident field resulting from various small reflections from the room side walls, which were quite different in structure.* The field of the horn was nearly

*Confirmation of this has been found recently with the apparatus in a smaller room where, with plentiful use of microwave absorbing sheets, the asymmetry can be shifted to one side or other by altering the axis of propagation and the line of the probe run, and where a setting was found giving negligible asymmetry.

constant in intensity at the distance of the probe, over the range studied to not more than 15 cm. on either side of the axis of propagation. While it had local irregularities in this range, these were much less pronounced than in the investigations on brass and hard rubber.

The lucite rod was a commercial 1 in. diameter one, 6 ft. long and, by measurement, 2.45 cm. in diameter. Its permittivity is about 2.56 and the loss tangent about 0.01, or nearly negligible, these being means of various published values for a wave-length of 3 cm. The rod is closely equivalent to an infinitely long one for the observations made, at distances behind it not exceeding 8 cm.

The tenite rod material, sent to us by Dr. Wait, was in two sections, each 1 ft. long and 2.54 cm. in diameter. Froese and Wait (1954) quote a permittivity value of 3.20 and made calculations considering a loss tangent of about 0.03 to be negligible. The two sections were cemented together end to end with glyptal cement. The resulting single rod was cemented to a section of the 1 in. diameter hard rubber rod used in earlier work, as support for the tenite part, at the required height and without too great a discontinuity at the junction. The rubber has much the same permittivity value, 3.45, as tenite though a somewhat higher loss tangent, 0.1 (Wiles and McLay 1954). The three-section rod was placed with the center of the middle (tenite) section at the height of the axis of propagation of the horn. This compound rod, as placed, was as close as could be got, using the material available, to an infinitely long one of tenite.

3. RESULTS

The diffraction patterns obtained from measurements of the field of the lucite rod are shown in Fig. 1 and of the tenite rod in Fig. 2. The intensity ratio I/I_0 , used as ordinate, is that of the square of the modulus of the electric field E_z normalized to that of the incident field at the same point. Because of the marked asymmetry of fields mentioned above, the two sides of each pattern are shown rather than the mean. The full curves show the right sides of the patterns, as seen looking from behind the rod toward the source. The mirror images of the left sides are shown by thinner lines, drawn only where the L-R differences are more pronounced. The origin is at the intersection of the cylinder axis (vertical), taken as the z axis, and the x axis which is in the direction of the incident field propagation (horizontal). The probe runs were made parallel to the horizontal y axis. The probe in the $y = 0$ position was fixed at 615 cm. from the source at the apex of the horn. The cylinder (and thus the origin) was moved, from $x = 0$ in the yz plane of the probe, towards the source before taking each successive run, to change the x position of the probe. The cylinder and probe were always closely the same large distance from the source so that the fields at them can be considered to be very nearly plane and nearly the same in magnitude in all observations made.

The x positions chosen for placing the tenite rod, as marked on Fig. 2, are simple multiples of the wave-length 3.2 cm. plus, in each case, the radius 1.27 cm. of the rod. Owing to a misunderstanding before final experimental runs were made this not well chosen system was used in earlier studies of brass and

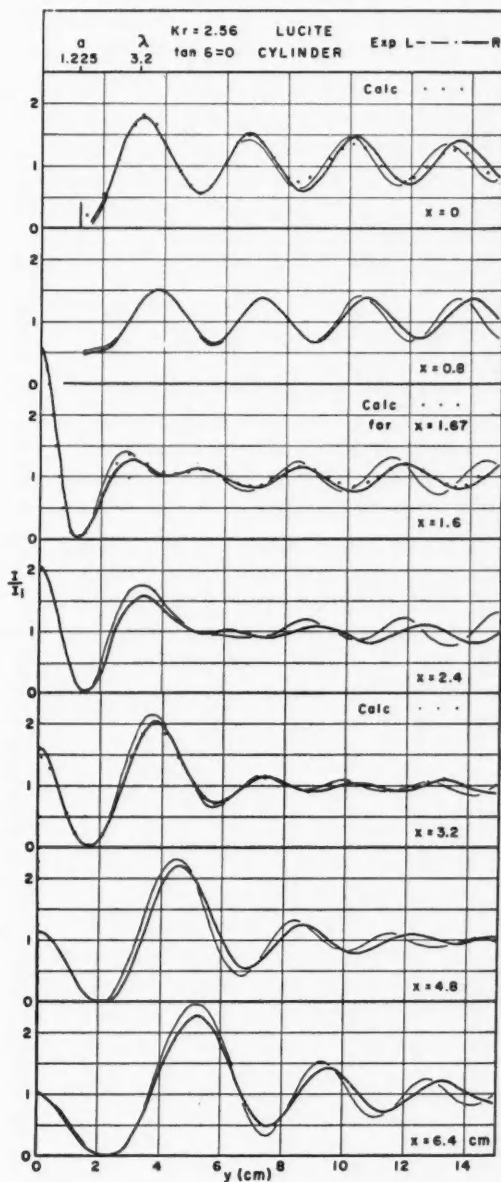


FIG. 1. Experimental and theoretical intensities in diffraction patterns of a lucite cylinder.

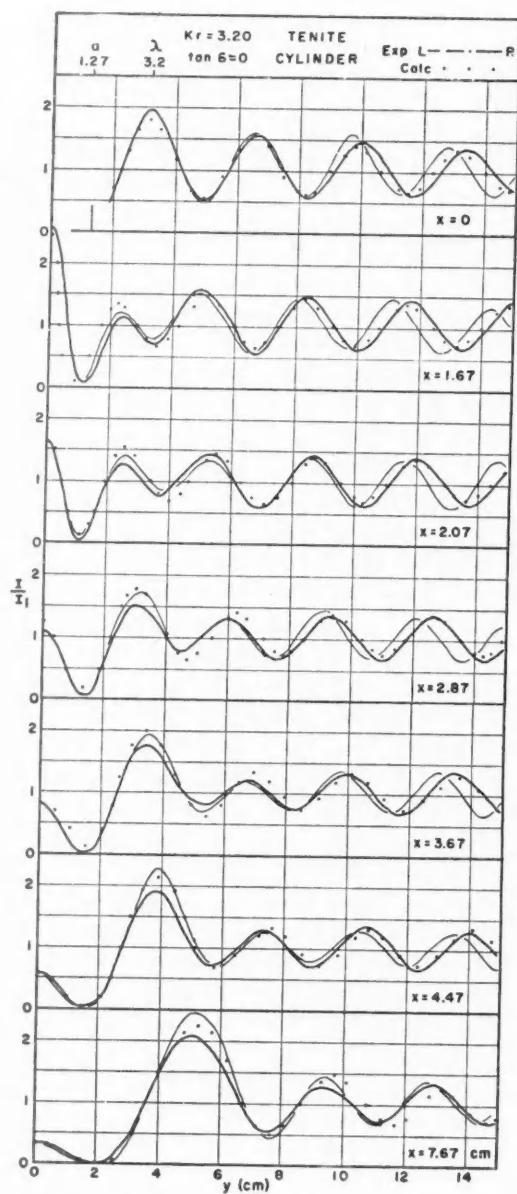


FIG. 2. Experimental and theoretical intensities in diffraction patterns of a tenite cylinder.

rubber rods (Wiles and McLay 1954). Froese and Wait had already made calculations for a tenite rod at some of these x positions before asking us to carry out experiments at these same positions.

The x positions chosen for placing the lucite rod, as marked on Fig. 1, are simple multiples of the wave-length measured from the origin and are independent of the radius of the rod, which was 1.225 cm. and not 1.27 cm. as in the former case. We changed the system to this more reasonable one for use in comparison of these results for lucite with those obtained for a lucite rod of $1\frac{1}{2}$ in. diameter, and for greater convenience in general. Results for the larger cylinder and the comparison are reported in Part II (McLay and Subbarao 1956), in the paper immediately following this.

The preliminary measurements on lucite sent to Froese and Wait (1954), and quoted by them, were made at a few x positions of both systems. They used a mean of our left and right side curves to compare with their calculated curves. The dotted points shown on Figs. 1 and 2 herein were taken from Froese and Wait's calculated curves. Points for $x = 1.67$ cm. on Fig. 1, third curve from top, are shown because they did not calculate values for $x = 1.6$ cm. and the change in pattern over the small change in x is practically within the limit of experimental error.

4. DISCUSSION OF RESULTS

Comparison of observed patterns of diffraction by the lucite cylinder, Fig. 1, with Froese and Wait's (1954) calculated ones shows quite good agreement. The calculated points for $x = 1.67$ cm. fall on a curve slightly outside a mean of the experimental curves for $x = 1.6$ cm. as they should. A similar difference for $x = 3.2$ cm. indicates a small experimental error. Corresponding comparison for tenite cylinder diffraction, Fig. 2, shows not as close agreement, especially for small values of y in the second to fourth patterns of Fig. 2. The maxima and minima in this region of the diffraction field of dielectric cylinders are resultants of three fairly intense beams (see further discussion based on geometrical optics) and are very sensitive to small changes of apparatus alignment. Also, disturbances may be caused by discontinuities at the cemented joins of the three-section rod and because its top end was probably not high enough above the $z = 0$ plane to make the approximation to an infinitely long cylinder as close as it should be.

Comparison of the diffraction fields of four cylinders comprising lucite and tenite, as reported herein, and brass and hard rubber (Wiles and McLay 1954) brings out a few very noticeable differences between the fields of a conducting and a dielectric rod and some similarities and differences in the fields of dielectric rods with different electrical properties. The fields can only be interpreted in all details by exact diffraction theory, using formulae given by Froese and Wait (1954) and used by them to calculate selected patterns of the lucite and tenite rods. It is proposed to show here, however, that a number of the main features and trends in the patterns can be accounted for quite well by a geometrical optics treatment, taking into account electromagnetic boundary conditions and interference. The discussion is presented for three

reasons: firstly, to show how well the above statement holds; secondly, to explain main features qualitatively and in simple physical terms; and thirdly, to indicate how well geometrical optics may be used to predict effects in the diffraction patterns of objects of other shapes than simple circular cylinders for which exact theoretical solutions may not be available.*

The resulting distribution, according to geometrical optics, of radiation incident in a parallel beam on a transparent cylinder, with its axis perpendicular to the incident propagation direction, is shown in Fig. 3, drawn to scale

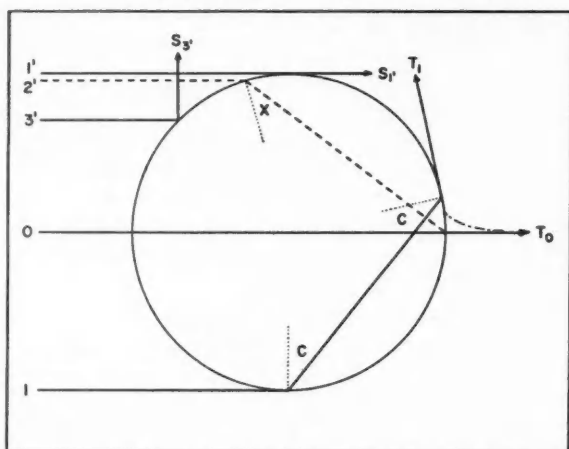


FIG. 3. Geometrical optics distribution of radiation in one quadrant behind a dielectric cylinder in plane incident waves.

for the case of lucite with dielectric constant 2.56, refractive index 1.6, and critical angle $C = 38^\circ 41'$. The discussion is confined to distribution in the upper right or first quadrant of the field. A finite beam will be referred to by the symbols of its two bounding rays. Thus the diverging beam $S_1'S_3'$ is the part of the incident parallel beam $1'3'$ that is surface reflected or scattered with π radians phase change. The obtuse-angled beam T_0T_1 is the transmitted part of the lower incident beam 01 . The transmitted part of $02'$ emerges, concentrated within the small region between the dash-dot line caustic curve and the OT_0 axis; that of $1'2'$ crosses this axis inside the cylinder and does not contribute to the field in the first quadrant. The incident beam above $1'$ is effective only in the first quadrant above the geometrical shadow line projection of S_1' , according to geometrical optics. For the rods considered here, with cylinder diameter of the order of a wave-length, this will be quite far from the actual case, except very closely behind the rod. For a conducting cylinder there are only two beams to consider in the first quadrant, namely, the incident beam above $1'S_1'$ and the scattered beam $S_1'S_3'$.

*The findings here have been very helpful in interpreting the observed diffraction patterns of a plano-semicylindrical lucite rod, as reported in Part II, and of a dielectric prism (Kneeland 1954).

The observed diffraction patterns of lucite and tenite cylinders at $x = 0$, $z = 0$, in the yz plane of the cylinder axis, shown in Figs. 1 and 2, and the corresponding ones of brass and hard rubber cylinders (Wiles and McLay 1954), are all very similar. The intensity approaches zero as the probe approaches the minimum position $y \doteq 1.6$ cm., which is limited by the sum of the radius of a cylinder and the radius 0.3 cm. of the probe crystal cartridge. This is in accordance with the boundary condition that the tangential electric field, polarized parallel to the z axis, must be zero over the surface of the conducting cylinder and zero at grazing incidence at a dielectric cylinder, with resulting phase change π of the 100% surface-scattered field. The first maximum out from the center is close to $y = \lambda = 3.2$ cm. in all cases and its intensity is higher for the conductor brass than for a dielectric rod, as expected because of greater surface scattering of the former. Successive maxima fall off regularly with increasing y and are of the order of λ apart.

The diffraction field behind a conducting cylinder is well known, both by theory and experiment. The intensity is small in the vicinity of the geometrical shadow (theoretically zero at the surface). Outside the shadow the maxima, mentioned above for $x \doteq 0$, shift outward from the x axis and decrease in intensity in a regular manner as x increases, the field being the resultant of two beams only, the incident and surface-scattered ones of Fig. 3.

In contrast to the field of a conducting cylinder, that of a dielectric rod has a maximum behind it at $y = 0$, x small, which decreases noticeably in intensity with increasing x . The first maximum out from the central one appears with small intensity at small x values, but increases rapidly with increasing x to become the main maximum at about $x = \lambda$ in the patterns of lucite and tenite rods in Figs. 1 and 2, as well as in that of hard rubber. The intensity of the next adjacent maximum out (this becomes the first and most intense one when $x = 0$ as noted above) falls noticeably with increasing x to a value less than that of the next maximum further out.

The above features are characteristics of the field distribution behind a dielectric cylinder, as distinct from that of a conducting one. In terms of geometrical optics, as illustrated in Fig. 3, the central maximum is the resultant of in-phase or near-in-phase convergence of the incident beam $02'$ and the corresponding broad beam from the lower half of the cylinder (not shown), i.e. as in lens focusing with aberrations. The maximum adjacent to the central one is the resultant of three beams, the incident, transmitted, and scattered ones, in the region above the geometrical shadow edge but most of its intensity is contributed by the transmitted beam only at small values of x behind the rod. The distribution of intensity about the maximum value of this peak when within or close to the shadow edge can of course only be understood if diffraction into the geometrical shadow region is considered. The noticeable falling off of intensity of the second maximum with increasing x is also the result of three-beam interference, in distinction to the regular fall off of intensity of this and all outer maxima in the simpler field of a conducting cylinder.

Differences in the fields of the three dielectric cylinders can also be interpreted in part, using the ray deviations of Fig. 3 and considering relative

Fresnel reflection coefficients for different permittivities and relative absorption depending on loss tangents. For tenite, $n = 1.79$, $C = 34^\circ$, $X = 26.5^\circ$, and hard rubber, $n = 1.85$, $C = 32.5^\circ$, $X = 22^\circ$, the incident beam $02'$ is much narrower than for lucite, $n = 1.6$, $C = 39^\circ$, $X = 37^\circ$, and the emergent transmitted beam T_0T_1 diverges more. A small absorption by tenite and considerably larger absorption by hard rubber further reduces the brightness of transmitted beams. Thus the whole transmitted field is fainter for tenite than for lucite and even fainter for hard rubber. Because of the much larger refractive indices of tenite and hard rubber the beam $1'3'$ scattered by each should be brighter than that scattered by lucite.

The intensity of the central maximum in the pattern of the lucite rod is larger than that of tenite and both are much larger than that of hard rubber, in keeping with the above prediction. Another effect can also be accounted for because of decreased transmission and increased scattering with increasing refractive index. A very noticeable feature in the diffraction field distribution of the lucite cylinder, as seen in Fig. 1, is that the field becomes nearly flat with intensity varying about unity in the region of the plane $x = 3.2$ cm., when y is larger than about 6 cm. This is understandable if the transmitted and scattered beams are of nearly equal amplitude in this region and out of phase by about π radians. (See also patterns of a larger diameter lucite cylinder in Part II.) In the case of tenite, Fig. 3 and Froese and Wait's (1954) calculated curves, and that of hard rubber, Wiles and McLay's (1954) curves, no such effects are noticeable. No doubt the scattered field predominates, in amplitude and phase, over the transmitted field in the whole region investigated, as might be expected from the foregoing discussion of qualitative dependence on refractive index.

It is concluded that geometrical optics considerations have been very useful in explaining most of the noticeable features in the near diffraction fields behind cylinders. Thus they should also be of considerable value in predicting effects in the fields of objects of other shapes, for which rigorous diffraction theory solutions may not be available. Further evidence to this effect is given in Part II.

ACKNOWLEDGMENTS

The financial support of a National Research Council of Canada grant-in-aid of research is gratefully acknowledged. We would also like to thank Dr. J. R. Wait for helpful discussion and for supplying the tenite rod used in this investigation.

REFERENCES

- FROESE, C. and WAIT, J. R. 1954. *Can. J. Phys.* **32**: 775.
KEYS, J. E. 1955. Defence Research Telecommunications Establishment of Canada, Radio Physics Laboratory Project Report 5-0-1. September 16.
KNEELAND, D. R. 1954. M.Sc. Thesis, Department of Physics, McMaster University, Hamilton, Ontario.
KODIS, R. D. 1952. *J. Appl. Phys.* **23**: 249.
McLAY, A. B. and SUBBARAO, M. K. 1956. *Can. J. Phys.* **34**: 555.
WILES, S. T. and McLAY, A. B. 1954. *Can. J. Phys.* **32**: 372.

DIFFRACTION OF 3.2 CM. ELECTROMAGNETIC WAVES BY DIELECTRIC RODS

II. LUCITE $1\frac{1}{2}$ IN. DIAMETER CYLINDER AND SEMICYLINDER¹

By A. B. McLAY AND M. K. SUBBARAO²

ABSTRACT

Diffraction patterns of a lucite cylinder and a half cylinder in a nearly plane beam of square-wave modulated 3.2 cm. waves, with electric vector parallel to the cylinder axis, have been measured in several planes transverse to the incident beam direction. Patterns of the half cylinder were obtained with the plane face toward and away from the source of radiation. Marked trends in the patterns are related qualitatively to the effects of transmission and surface reflection, both external and internal, expected from geometrical optics considerations.

1. INTRODUCTION

Diffraction patterns of lucite and tenite cylinders of about 1 in. diameter have been measured and are reported in Part I, in the preceding paper (Subbarao and McLay 1956). Observations were made with each cylinder placed in a nearly plane beam of square-wave modulated 3.2 cm. waves, with electric vector parallel to the cylinder axis. Experimental results for these rods agreed quite well with theoretical ones (Froese and Wait 1954). Similar results have been obtained using a larger lucite cylinder of diameter 3.90 cm. (about $1\frac{1}{2}$ in.) and length 1 meter, and using the same rod after machining accurately to a plano-convex half cylinder, placed with plane face either toward or away from the source of radiation. Results for the two cylindrical lucite rods of different diameters, and those for the larger lucite cylinder and the half cylinder of the same diameter, are compared with each other and with geometrical optics predictions.

The apparatus is the same as that described in Part I and present experiments were carried out under conditions identical with those used in the preceding investigation. The chosen coordinate system has the long cylinder axis of a rod as z axis, and the x axis as the direction of incident propagation. Patterns were observed on lines parallel to the y axis.

2. RESULTS

The diffraction patterns obtained from measurements of the field of the lucite full cylinder are shown in Figs. 1 and 2, of the half cylinder with plane face toward the source in Fig. 3, and with plane face away from the source in Figs. 4 and 5. The intensity ratio I/I_0 used as ordinate is that of the square of the modulus of the electric field E_z normalized to that of the incident field at the same point. Because of marked nearly constant asymmetry of fields in all diffraction experiments carried out with the apparatus in its present location the two sides of each pattern are shown, as in Part I and in an earlier paper by

¹Manuscript received January 31, 1956.

Contribution from the Department of Physics, Hamilton College, McMaster University, Hamilton, Ontario.

²Present address: Junior Scientific Officer, Indian Naval Physical Laboratory, Cochin, India.

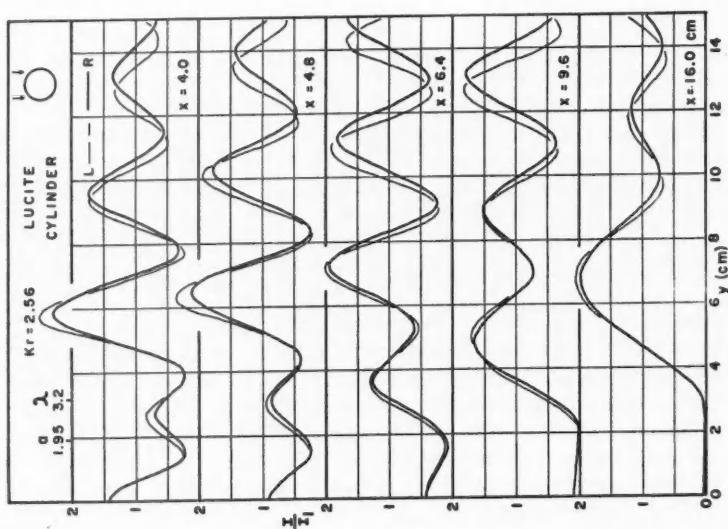


Fig. 2. Diffraction patterns of a lucite cylinder (continued).

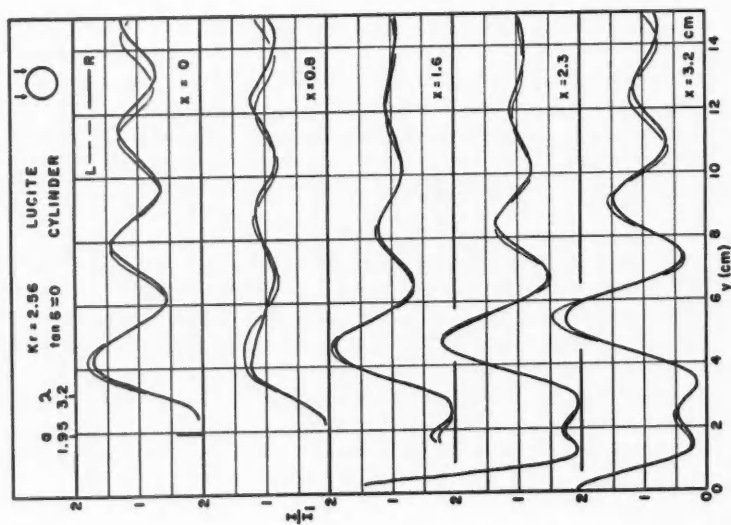


Fig. 1. Diffraction patterns of a lucite cylinder.

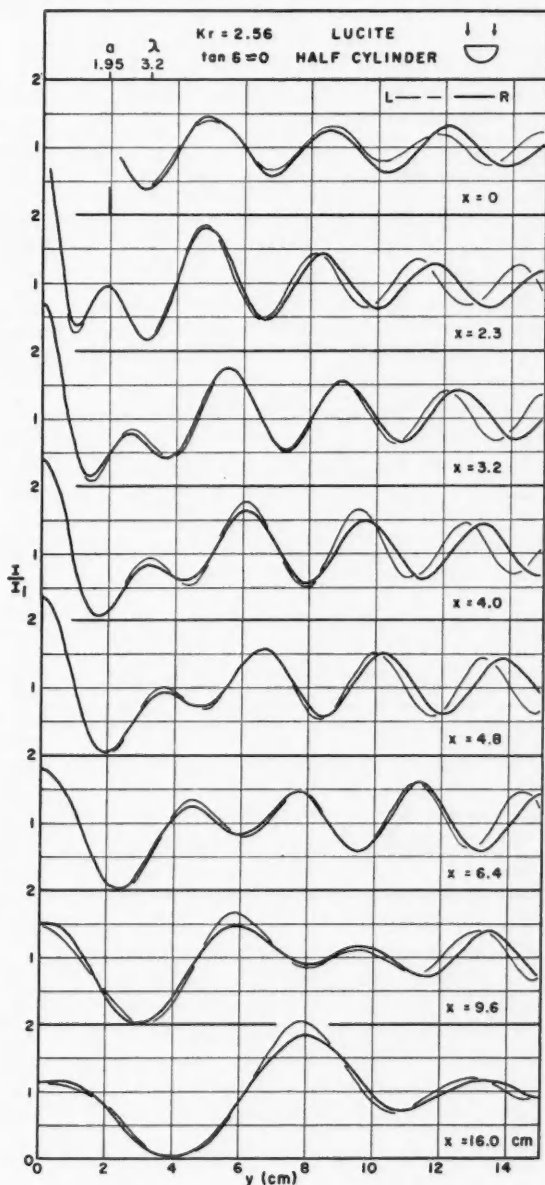


FIG. 3. Diffraction patterns of a lucite half cylinder with plane face toward the source.

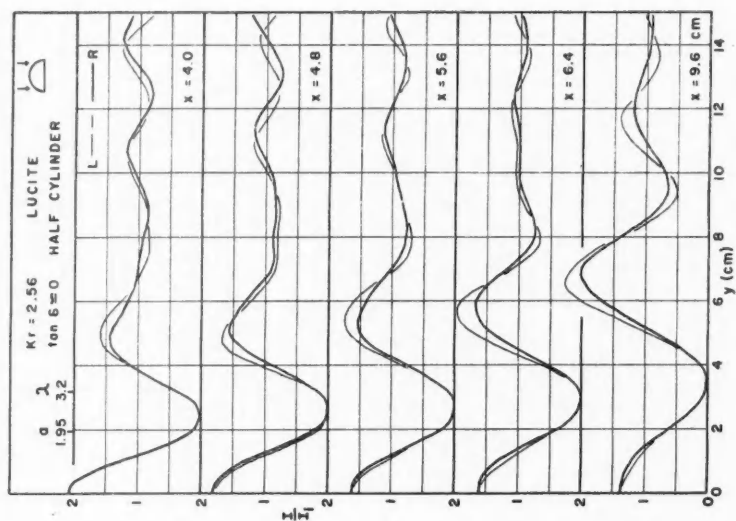


FIG. 5. Diffraction patterns of a lucite half cylinder with plane face away from the source (continued).

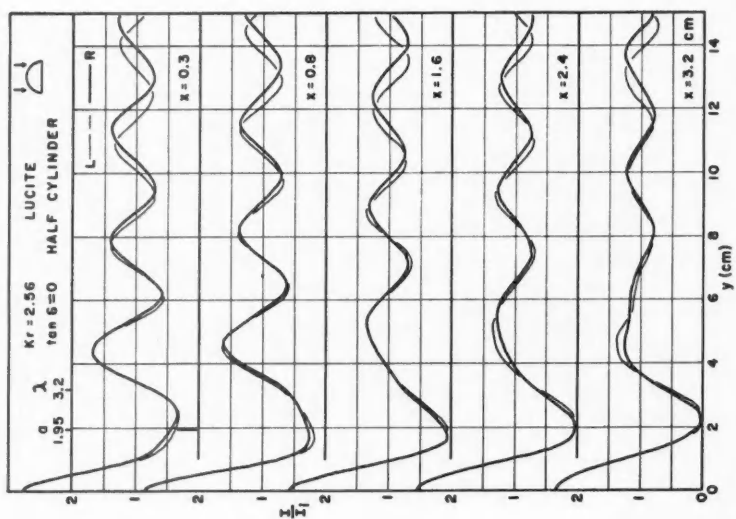


FIG. 4. Diffraction patterns of a lucite half cylinder with plane face away from the source.

Wiles and McLay (1954), rather than the mean. The full curves show the right sides of the patterns, as seen looking from behind the rod towards the source. The mirror images of the left sides are shown by thinner lines drawn only where the differences are more pronounced. The minimum distance of approach of the axis of the probe crystal to the surface of a rod is 0.3 cm., the radius of the cartridge.

3. DISCUSSION OF RESULTS

The observed diffraction patterns of the lucite cylinder, shown in Figs. 1 and 2, could be compared with theoretical ones by carrying out tedious computations with use of an equation given by Froese and Wait (1954). This has not been done yet but the present results are considered to be reasonably accurate because of the close agreement of observed and calculated patterns of the smaller lucite cylinder, reported in Part I. The diffraction problems in the cases of the half cylinder in its two experimental positions await solutions. Discussion, based on geometrical optics and taking into account electromagnetic boundary conditions and interference, as used in Part I, will be shown to be useful here also in explaining main features in the observed diffraction patterns.

The resulting distribution, according to geometrical optics, of radiation incident in a parallel beam on a transparent dielectric cylinder and on a half cylinder, in the two positions used, is shown in Fig. 6, drawn to scale for lucite with permittivity $K\epsilon = 2.56$, refractive index $n = 1.6$, and critical angle $C = 38^\circ 41'$. Boundary rays of transmitted and surface-scattered beams are distinguished by letters T and S respectively. The rays marked by R in the lower diagram are boundary ones of beams that emerge into the first quadrant of the field after double internal reflection. It will be shown that this radiation makes an effective contribution to the resultant field in this quadrant. Radiation that is internally reflected in each of the other two rods has considerable effect on the back scattered field, but it contributes only negligibly to the forward field after two or more internal reflections at one or more small angles of incidence, with corresponding low reflecting power.

The diffraction field of the full cylinder, shown in Figs. 1 and 2, has main features similar to that of the smaller 1 in. diameter lucite cylinder. The geometrical optics distribution of beams was discussed more fully in Part I, but is drawn again in Fig. 6 for convenient reference and comparison with the other two cases in that figure. There are a few noticeable differences in the patterns of the two cylinders because of the difference in diameters. While the central maximum at $y = 0$ has large intensity close to the rod and falls off rapidly with increasing y in both cases, the first maximum out from it is smaller and more nearly completely resolved in the field of the $1\frac{1}{2}$ in. diameter rod. Its intensity rises more slowly with increasing x to become the main maximum at about $x = 3\lambda$, in contrast to the corresponding effect closer to the rod, at about $x = \lambda$, in the field of the smaller rod. As previously pointed out, the central and first maxima in the very near fields of these rods are characteristic features of dielectric cylinder diffraction, as distinct from those of conducting

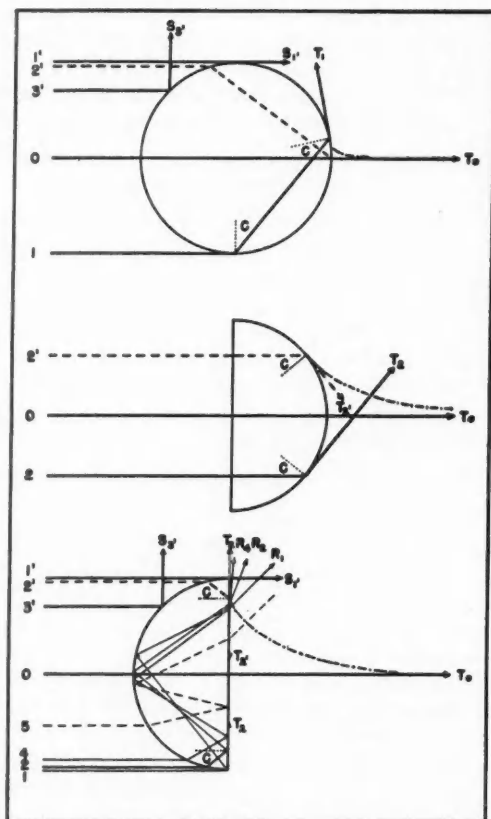


FIG. 6. Geometrical optics distribution of radiation in one quadrant behind dielectric rods in plane incident waves.

ones, since they result predominantly from transmission of beam 01, which emerges as beam T_0T_1 .

Inspection of Fig. 1 will show that the field becomes nearly flat, with intensity varying about unity, in the region $x = 1.6$ cm. when y is larger than about 9 cm. A similar effect was observed in the field of the 1 in. diameter lucite cylinder at a little larger value of x . The effect has been accounted for as the superposition of three beams in the general region outside the geometrical shadow edge above ray S_1 , namely, the incident beam of intensity unity and the transmitted and scattered beams, with nearly equal amplitudes and about π radians phase difference in the narrow region in question.

The field in the first quadrant of the half cylinder with plane face toward the source should be a particularly simple one according to geometrical optics, as shown in Fig. 6, since there is no surface scattering. Comparing with

the case of the whole cylinder, the incident beam 02 , which is transmitted as T_0T_2 by the half cylinder, is much narrower than the corresponding beam 01 , which is transmitted as T_0T_1 by the whole cylinder, but T_0T_2 is much less diverging than T_0T_1 . The beam $02'$ is narrower and is converged less by the half cylinder than the corresponding beam $02'$ is by the whole cylinder. Thus the caustic region, between the dash-dot line and the x axis, in the former case is much larger and more extended along the x axis. As a result of the above, the central maximum at $y = 0$ should not be as intense close to the half cylinder but should not fall off as much with increasing x . This prediction agrees with experimental observation as shown by comparison of patterns of Fig. 3 with those of Figs. 1 and 2.

The first maximum out from the center is small, and increases with increasing x to become the main maximum in the field, as in that of the cylinder. However the intensity is rising a bit on approaching the rod from $x = 3.2$ cm. to $x = 2.3$ cm., as seen in Fig. 3. Subsequent observations not yet completed at even smaller values of x show continued increase on closer approach and this is being investigated further. The field at $x = 0$, i.e., on the y axis, is also increasing on approach to the rod in contrast to a decrease toward zero in the similar case of the field of the cylinder and in the closely similar one, at $x = 0.3$ cm., of the half cylinder with plane face away from the source. The variations of intensity at and near $x = 0$ are not as marked as they are in the latter two fields, where surface scattering contributes markedly to the resultant in this region, as well as throughout the whole region above the geometrical shadow edge.

Since there is no surface scattering into the first quadrant, there should be no variation of intensity above the geometrical shadow edge, according to geometrical optics, until part of the transmitted beam T_0T_2 crosses it along T_2 . Below this edge and above the caustic curve line there should be no field at all. Thus geometrical optics is quite inadequate to explain the observed variations of field in these regions. Similar diffraction effects are, of course, important also in the fields of the other two rods, but are obscured in part because their fields are more complex. The usefulness of geometrical optics predictions is that main features in diffraction patterns tend to appear near geometrical optics paths, even in the cases investigated here when the object dimensions are of the order of the wave-length and diffraction effects are much more evident than in ordinary optics experiments.

The field of the half cylinder with plane face away from the source is the most complex one of the three, both experimentally and according to geometrical optics. In this case, as seen in Fig. 6, there is a scattered beam S_1S_2 , as for a whole cylinder. The field at $x = 0.3$ cm. outside the geometrical shadow should be closely identical in all respects to the field of the whole cylinder at $x = 0$. The convergence of the transmitted beam is greater than that transmitted by the half cylinder in reverse orientation, but the subsequent divergence is also greater. The caustic regions therefore have much the same extent and the fall off of intensity of the central maximum in Figs. 4 and 5 compares closely with that in Fig. 3, throughout the range of x investigated.

In distinction the small maximum that appears close to the central maximum in the patterns of the other two rods, and increases to become the main one at larger values of x , is not noticeably present in Figs. 4 and 5. Instead there is a small but easily noticed distortion of the inner side of the first trough at $x = 0.3$ cm., which moves to the outer side at the next two x positions, to the first peak at $x = 2.4$ and $x = 3.2$ cm., and a distortion of successive troughs and peaks follows at larger values of x . The center of the disturbance lies nearly in a straight line between rays R_1 and R_2 of Fig. 6 that makes an angle of about 50° with the direction of incident propagation.

The following explanation of the distortion is offered, with reference to Fig. 6. The incident beam 12 is totally reflected at the plane surface and converges before diverging. It is reflected again at angles less than, but near critical at the curved surface (ray 1 is the critical ray at external incidence and at the second reflection), is converged again, and emerges as a diverging beam R_1R_2 to affect the field in the region of distortion noted above. To complete the discussion of double internal reflection, ray 4 emerges as R_4 , the ray at maximum deviation, 85° , for double internal reflection. The deviations of incident rays between 4 and 0 decrease from the maximum value to zero for ray 0. The broken-line incident ray 5 is the one for which the deviation is the same as that for R_4 . Thus the part of the incident beam 15 that is doubly reflected emerges at deviation of 45° or greater to cause the distortion, which is maximum along a line at about 50° deviation as noted above.

It seems certain that the noticeable distortion observed in the diffraction field of a dielectric half cylinder with plane face away from the source is the effect of a beam, doubly internally reflected, that emerges in the first quadrant and is superposed on one or more of the incident, transmitted, and externally reflected beams, as applicable in or outside the geometrical shadow.

It is concluded that main features and marked trends in the diffraction fields of these rods appear close to regions predicted for such effects by geometrical optics and interference, even in the extreme circumstances of these experiments, where object size and field distances from the object are of the order of a wave-length of the incident radiation. Correlation of similar and dissimilar main features in the diffraction patterns of a half cylinder and full cylinder that have been observed experimentally may be of value in a theoretical treatment of diffraction by a dielectric half cylinder.

ACKNOWLEDGMENT

The financial support of a National Research Council grant-in-aid of research is gratefully acknowledged.

REFERENCES

- FROESE, C. and WAIT, J. R. 1954. Can. J. Phys. **32**: 775.
SUBBARAO, M. K. and McLAY, A. B. 1956. Can. J. Phys. **34**: 546.
WILES, S. T. and McLAY, A. B. 1954. Can. J. Phys. **32**: 372.

THE RESOLVER, A CIRCUIT FOR REDUCING THE COUNTING LOSSES OF A SCALER¹

By R. E. BELL²

ABSTRACT

The resolver is a circuit that reduces the counting losses of an ordinary scaler by storing up most of the pulses that otherwise would be lost in dead time, and releasing them uniformly at a safe rate for the scaler. Even for very short input pulses, the circuit contains no active elements that need to be fast enough to follow these pulses, and is thus simpler than an equivalent fast scaler. In a typical case the maximum permissible counting rate of the scaler is raised by a factor of the order of 30. The counting losses of such a circuit are computed. A detailed circuit and the results of tests on it are shown.

I. INTRODUCTION

The problem of counting random pulses at high rates is conventionally attacked by building scaling circuits of small dead time. An alternative approach, described here, is to use a circuit having a short-term memory to remove some of the randomness from the train of pulses. The ideal effect of such a circuit, which we call a "resolver", is to reproduce a train of random pulses with all the pulse intervals shorter than a time T (the "resolved time") stretched out to be equal to T . The modified pulse train can then be counted without loss by any scaler whose dead time τ is less than T . (Enquiries have shown that a similar proposal was made some years ago by Cooke-Yarborough (1947) but was not pursued.) It turns out that a resolver circuit can be built without any active circuit elements that have to follow the fast input pulses. The circuit is thus simpler to build and maintain than an equivalent fast scaler.

The present circuit works in the following way. Each input pulse goes directly to an integrator circuit and produces a voltage rise at the integrator output. This rise turns on a square wave oscillator of period T whose output is connected back to the integrator so as to produce a voltage fall roughly equal to the rise caused by the input pulse. For a single input pulse, therefore, the oscillator performs a single oscillation and in so doing turns itself off. Two input pulses close together produce double the integrator output and require two oscillations for their cancellation, and so on. The number of oscillations is always equal to the number of input pulses stored in the integrator, and the least possible interval between oscillator pulses is T . The only way a pulse can be lost in such a system is to have the integrator, or memory, full at the time the pulse arrives; such a pulse is not stored in the memory, and is lost. The oscillator output is sent to the slow scaler, thus completing a fast counting system that does not contain any fast active elements.

Another form of the resolver that suggests itself is one in which the integrator performs a linear run-down to its initial level in a time T after the receipt of the input pulse. A second pulse within this time causes a further step in the

¹Manuscript received February 27, 1956.

Contribution from the Radiation Laboratory, Department of Physics, McGill University, Montreal, Canada.

²On staff of Atomic Energy of Canada, Ltd., Chalk River, Ontario.

integrator output, and delays the return of the integrator by a further time T , and so on. The integrator waveform turns on an oscillator of period T , as before. Trials showed that this circuit can be made to work, but its timing must be held within close limits, and it is consequently more critical in adjustment than the circuit that was actually adopted.

The first step in the direction of the resolver has been made many times in the past when pulse integrators have been used as scalers. In these circuits a given number of pulses, typically 10, produces sufficient voltage at the output of an integrator to trigger a pulse generator which simultaneously discharges the integrator and passes a pulse on to succeeding scaling stages. Such a circuit is easy to build, but has a number of disadvantages. First, a fairly small drift in circuit conditions may change the effective scaling factor from 10 to 9 or 11. In the resolver, on the other hand, a drift of this kind would have to be considerably larger, and even then would operate only on some of the pulses that are being "saved" by the resolver, and not on the total counting rate. Second, at low counting rates the interval for accumulating 10 pulses is so long that the integrator fails to hold its charge. Third, in many such circuits the 10th pulse, discharging the integrator, is followed by a dead time that is distinctly longer than that following the other pulses. Both the latter two difficulties are eliminated in the resolver.

The resolver is at a disadvantage compared with a fast prescaler in one respect, because the resolver does not increase the maximum rate at which the system can count. To take an extreme example, a resolver clearly cannot be of any benefit when periodic pulses are being counted, and only a prescaler will suffice. On the other hand, most existing scalers used with random pulses reach their counting rate limit because of input dead time losses; for these cases the resolver can raise the permissible counting rate by a large factor.

II. COUNTING LOSSES

The counting losses of a conventional scaler and of the resolver-scaler can be estimated as follows. Let the dead time of the scaler be τ and the resolved time of the resolver be T . Let the true average counting rate of random pulses be n . The operative parameter for counting losses is the relative counting rate $n\tau$ or nT .

The probability that a pulse will be lost in the conventional scaler is equal to the probability that it has been preceded within a time τ by one or more other pulses. Using the Poisson distribution, this is

$$(1) \quad L_1 = e^{-n\tau} [n\tau + (n\tau)^2/2! + \dots] = e^{-n\tau} [e^{n\tau} - 1] = 1 - e^{-n\tau}.$$

This equation is strictly true only for a scaler with extending dead time (Elmore 1950), but can be applied with little error to any scaler so long as $n\tau$ is small. The counting rate of a scaler with a non-extending dead time τ is

$$(2) \quad n' = n/(1+n\tau),$$

so that the fractional losses are, for any value of $n\tau$,

$$(3) \quad L_1 = n\tau/(1+n\tau).$$

Equations (1) and (3) are equivalent when $n\tau$ is small.

The probability that a pulse will be lost in a resolver having a memory capacity of k pulses is equal to the probability that the memory is full; for nT small this is the probability that the pulse has been preceded within a time T by k or more other pulses, namely

$$(4) \quad L_k = e^{-nT} \left[\frac{(nT)^k}{k!} + \frac{(nT)^{k+1}}{(k+1)!} + \dots \right].$$

For values of nT that are not small, a more complex procedure is necessary for computing L_k . This procedure is outlined in Appendix I. Equation (4) reduces to equation (1) when $k = 1$, expressing the obvious fact that a resolver with a one-pulse memory is the same as a scaler with a dead time T , at least for small nT .

A particularly simple case is that for which the resolver has an infinite memory; then all rates less than $1/T$ are counted correctly, and all rates greater than $1/T$ are counted with loss $(n-1/T)$, so that the fractional loss is, for $nT > 1$,

$$(5) \quad L_\infty = (nT - 1)/nT.$$

Fig. 1 shows the fractional counting losses L_1 , L_2 , L_3 , L_4 , and L_∞ as a function of the relative counting rate nT . The curves for L_2 , L_3 , and L_4 were computed from equations (16) to (19) in Appendix I. The curve for $k = 1$ shows the well-known fact that if the maximum acceptable fractional counting loss is 0.01, a conventional scaler can be used only up to rates where $n\tau = 0.01$, even though the scaler is physically capable of counting 100 times faster. Using the same criterion, a resolver with a three-pulse memory can be run at rates up to

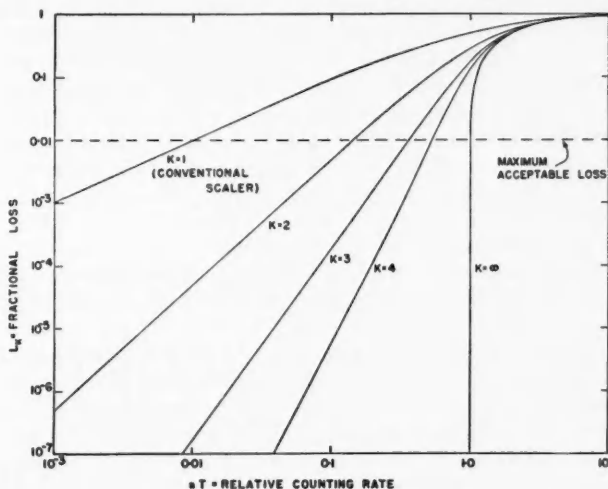


FIG. 1. Computed fractional counting losses for a resolver having memory capacities, k , of 1, 2, 3, 4, and an infinite number of pulses, plotted as a function of relative counting rate nT . A horizontal broken line shows the usual maximum acceptable fractional loss for a counting system. The curve for $k = 1$ applies to a conventional scaler with non-extending dead time.

$nT = 0.36$. Since the circuit cannot count faster than the rate where $nT = 1$, there is little point in straining for memory capacity past $k = 3$ or 4, and the present circuit has been designed with this capacity in mind.

To take a numerical example, a three-pulse memory resolver with $T = 4 \mu\text{sec.}$ feeding a scaler with $\tau = 3 \mu\text{sec.}$ can be run up to $nT = 0.36$, or $n = 90,000$ per sec. Since the scaler alone can be run only up to 3333 per sec., the advantage in counting rate achieved with the resolver is a factor of 27. For a four-pulse memory the corresponding factor is 40. The losses given above may be called the memory losses of the resolver. There may also be losses of the usual dead time variety in the source of pulses or at the resolver input. At the rate of 90,000 per sec. mentioned above, there will be a fractional dead time loss exceeding 0.01 if this first dead time exceeds $0.11 \mu\text{sec.}$ Performance of this order is automatically obtained at the resolver input, so that the final effect is to throw the burden where it belongs, viz., on the source of pulses.

It is natural to compare the losses of a resolver of memory k with those of a fast scale of k , both feeding a scaler of dead time τ . Assuming that the input losses of the fast scaler are zero, the fractional loss of pulses in the slow scaler fed by the fast one is given by Elmore (1950) as

$$(6) \quad f_k = \frac{(n\tau)^k}{k!} \frac{1}{1 + n + \frac{(n\tau)^2}{2!} + \dots + \frac{(n\tau)^k}{k!}}.$$

For small $n\tau$, both f_k from (6) and L_k from (4) approach $(n\tau)^k/k!$, proving that the two devices are equivalent for equal total counting rates. A comparison at higher values of $n\tau$ shows that the scaler has an advantage because it multiplies the limiting counting rate of the system by k . This advantage is never large—for example a fast scale of four will count only 1.6 times as fast as a resolver with a four-pulse memory before it reaches a fractional loss of 0.01—and may be nullified or reversed by the greater difficulty of achieving the necessary short input resolving time in the fast scaler. In addition, the resolver has the advantage that it does not interfere with the decimal or binary indication scheme of the existing scaler to which it is attached.

III. CIRCUIT DESIGN

The present resolver circuit was built to replace the standard plug-in pulse shaper unit in the Chalk River-Marconi scale of 1000 (Moody *et al.* 1951). This scaler supplies +130 volts and -100 volts d-c. to its component units, and the resolver was built to operate from these voltages. A somewhat higher positive supply voltage would have made the design easier. The resolved time T of the resolver circuit was made equal to $4 \mu\text{sec.}$, so that it could be used with any scaler having a τ less than, say, $3.5 \mu\text{sec.}$ The present scaler has $\tau = 3 \mu\text{sec.}$

The circuit is shown in Fig. 2. The input pulse is a 55-volt negative pulse of duration $0.3 \mu\text{sec.}$, which charges C_1 and C_2 through V_{1B} on its front edge and discharges C_1 through V_{1A} on its returning edge. (A pulse of half this size could be used if C_1 were doubled, and so on.) Since the integrator V_3 is not fast enough in its plate circuit to react fully within the charging time ($\sim 0.1 \mu\text{sec.}$),

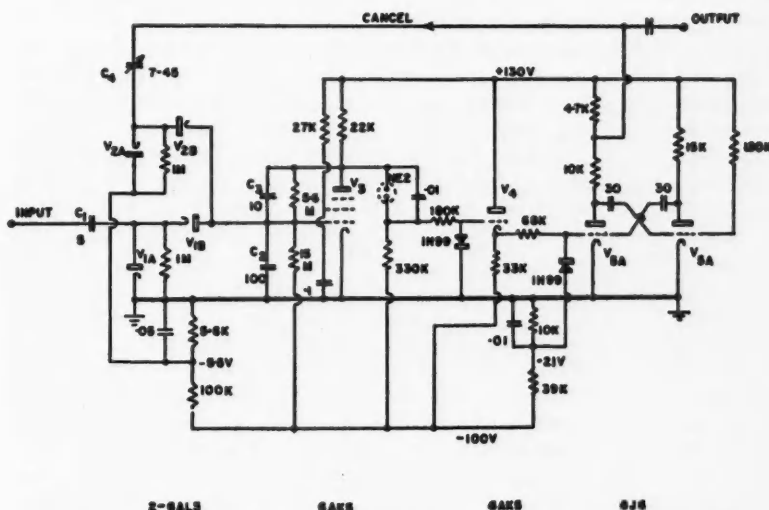


FIG. 2. Circuit diagram of the resolver. All resistors are $\frac{1}{2}$ watt except the plate loads of V_3 and V_5 and the cathode load of V_4 , which are 2 watt. Carbon resistors were used throughout. Capacitor values smaller than unity are in $\mu\text{f.}$, and those larger than unity are in $\mu\text{m.}$

most of the charge initially appears in C_2 , but is quickly transferred to C_3 , the main tank condenser, as the plate circuit of the integrator reacts. The presence of C_2 ensures that the integrator will work substantially the same way for a very fast pulse as for a slower one, and the only elements that "see" the fast pulse are C_1 and C_2 and the diodes V_1 . The condensers C_1 , C_2 , and C_3 are proportioned so that $C_1 \ll C_2 \ll GC_3$ where G is the gain of V_3 . The rise in voltage at the anode of V_3 is a little over 20 volts per input pulse. The quiescent conditions of V_3 are set by the 5.6 M and 15 M resistors connected from its grid to its anode and to -100 volts respectively; the d-c. feedback action of these resistors holds the anode of V_3 at $+40$ volts, and their presence gives the integrator a decay time constant of about $50 \mu\text{sec.}$ The grid of V_3 sits at about -2.5 volts. On account of the presence of the 1 M resistors across V_{1A} and V_{2A} , diode V_{1B} has a reverse bias of 2.5 volts and diode V_{2B} of 3.0 volts. These reverse biases prevent any leakage of charge through the diodes to or from the grid of V_3 .

The voltage at the anode of V_3 is dropped by 55 volts by the bypassed neon bulb NE2, with small loss of signal, and is applied through a 180 K resistor to the grid of V_4 . The quiescent voltage here is -15 volts, and V_4 's cathode is at -13 volts. The signal from the integrator is greater than 15 volts, and it raises the grid of V_4 to ground, where it is caught by the germanium diode 1N99. The cathode of V_4 is now at $+2$ volts, and the multivibrator V_5 is free to oscillate. The first pulse from the anode of V_{5A} is delayed by about $3 \mu\text{sec.}$ (the time for its grid to rise from -13 volts to about -4 volts where conduction starts) and is negative with duration $1.5 \mu\text{sec.}$ After this, if the multivibrator

is left running, the anode of V_{5A} produces 1.5 $\mu\text{sec.}$ negative pulses at intervals of 4 $\mu\text{sec.}$ (The 1N99 germanium diode from the grid of V_{5A} to a bypassed point at -21 volts limits the amount by which this grid is driven negative by the anode waveform of V_{5B} . This arrangement minimizes variations in the pulse spacing of the multivibrator.)

The returning edge of each 1.5 $\mu\text{sec.}$ negative pulse from the anode of V_{5A} produces, via C_4 and V_{2B} , an effect in the integrator opposite and roughly equal to the effect of each input pulse. The magnitude of this cancelling effect is adjusted by varying C_4 . The cancelling effect occurs just at the instant when the multivibrator is returning to its initial conditions, so that it can start again immediately if another input pulse should occur. If two or three input pulses have been stored in the integrator, an equal number of cancelling pulses occurs before the integrator is fully discharged and the multivibrator is turned off. A moment's reflection shows that this is true even if the integrator is somewhat non-linear. There is little interaction between the input pulse and the cancelling pulse in the integrator, and the circuit functions correctly when an input pulse happens to occur at the same instant as the cancelling effect from a previous pulse. There is thus no dead time due to the cancelling pulse.

For a complete unit to use on a scaler, the circuit of Fig. 2 should have added to it an input circuit providing pulses of the desired size, and an output circuit to feed the rest of the scaler and to relieve the circuit of Fig. 2 of output circuit loading. A complete unit of this kind, built to plug into a Chalk River-Marconi scaler, is described briefly in Appendix II. Most of the experimental tests of the resolver were carried out with the complete unit.

IV. EXPERIMENTAL TESTS

(a) *Tests with Periodic Pulses*

The initial tests of the circuit of Fig. 2 were carried out using a pulse generator giving rounded triangular pulses of base width 0.3 $\mu\text{sec.}$ The generator could provide up to four such pulses in a group, the pulse spacing within the group being variable up to 20 $\mu\text{sec.}$ and the group recurrence frequency variable up to 60,000 per sec. With these facilities almost any combination of pulse spacings likely to be encountered with random pulses could be duplicated. The results with these pulses were as follows:

(1) Three pulses are correctly integrated and cancelled at any spacing down to the point where the input pulses begin to overlap. If four pulses are put in in quick succession, that is within the resolved time of 4 $\mu\text{sec.}$, the integrator nearly saturates, but the fourth pulse is still correctly stored and cancelled. A fifth pulse was not available, but it would almost certainly not have been correctly stored, and so would have been lost. Since even the fourth pulse carried the circuit nearly to its limit, conservative practice would call this circuit a three-pulse memory. These remarks apply at total pulse rates up to the point where successive groups of pulses begin to overlap at the resolver output, i.e. to rates greater than 200,000 per sec.

(2) In the present circuit, though not in an earlier experimental version, d-c. coupling is used from the integrator output to the gated oscillator. If this

is not done, the integrator can get out of its normal voltage range at high pulse rates, and settle down to a stable state in which, for example, three pulses are fed in as a group, but only two cancelling pulses are produced. It is clear that a-c. coupling with "d-c. restoration" is not sufficient to cure this trouble, but d-c. coupling removes it entirely.

(3) Before the crystal diode was installed at the grid of V_{bA} , the gated oscillator's pulse spacing, T , tended to vary slightly with pulse rate. In any case a resolver having $T = 4 \mu\text{sec.}$ should probably not be used with a scaler having τ longer than, say, $3.5 \mu\text{sec.}$

(4) For best performance at all rates including the highest, the cancellation condenser C_4 should be adjusted to make the cancellation correct for a close group of three pulses, rather than for a single pulse. This setting is not at all critical, except in tests such as (1) above when the resolver is run at rates where nT is approaching unity.

(b) Waveforms

Figs. 3(a) and (b) are reproductions of photographs of oscilloscope traces made with the complete resolver unit (Appendix II) excited by the pulse generator mentioned above. The total length of the oscilloscope trace in all the photographs is $20 \mu\text{sec.}$ Fig. 3(a) shows the response of the resolver to two input pulses separated by $2 \mu\text{sec.}$, and Fig. 3(b) the response to four input pulses within $1.05 \mu\text{sec.}$ (pulse separation $0.35 \mu\text{sec.}$). In each figure, the first line is the input waveform (pulse amplitude ~ 2 volts), the second is the output of the pulse shaper stage applied to the integrator input (pulse amplitude 55 volts), the third is the integrator output waveform (step amplitude 21 volts), and the fourth is the output waveform (pulse amplitude 60 volts). The resolved time is $4 \mu\text{sec.}$ The oscilloscope sensitivity is different for the different traces in each figure, but the same for a given trace in one figure as in the other.

(c) Test with Random Pulses

In order to make a straightforward test of the resolver with random pulses, it would be necessary to have a source of random pulses with very small dead time (say less than $0.1 \mu\text{sec.}$) and a scaler of corresponding dead time with which to record these pulses. The test would then consist of a comparison between the fast scaler and a resolver plus slow scaler. Since the equipment necessary for the above test was not at hand, the following alternative procedure was followed.

The source of pulses was a Co^{60} source and a stilbene 1P21 scintillation counter feeding its output directly into a univibrator circuit of dead time approximately $0.5 \mu\text{sec.}$ The pulse rate of this combination was varied by changing the source-to-counter distance. The pulses were fed into a resolver and scaler combination (with the resolver T adjusted to $6 \mu\text{sec.}$), and also into a conventional scale of 1000 having a dead time of $3.2 \mu\text{sec.}$ (measured with a sliding pulser and oscilloscope). With this arrangement the resolver-scaler had dead time losses due to the $0.5 \mu\text{sec.}$ dead time of the source of the pulses, while the conventional scaler had dead time losses due to its own $3.2 \mu\text{sec.}$ dead time. The expected difference in counting losses between the two units can be com-

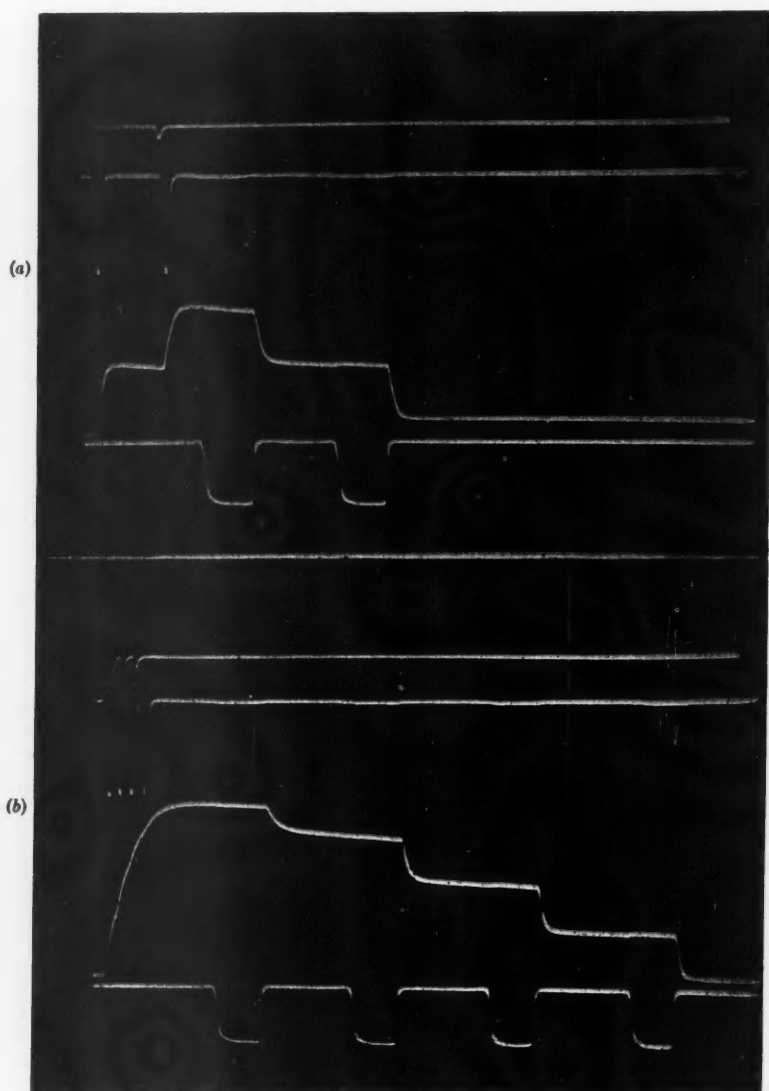


FIG. 3. Waveforms observed with the complete resolver unit of Appendix II. (a) Response to two input pulses spaced by $2 \mu\text{sec}$. (first line) of the input univibrator (second line), the integrator (third line), and the output circuit (fourth line). (b) The same set of responses to four pulses within $1.05 \mu\text{sec}$. The resolved time is $4 \mu\text{sec}$. in both (a) and (b). This figure shows that a moderate degree of non-linearity in the integrator has little effect on the performance of the unit.

puted for any counting rate from equation (3) using the appropriate dead times, to an accuracy better than 10%. The observed difference will be less than this amount by the memory loss of the resolver, if it is large enough to be appreciable.

In the experiment, the two instruments were run simultaneously at various pulse counting rates. Timing errors were eliminated by starting and stopping the common source of pulses rather than the instruments themselves. On account of the simultaneity of the observations, statistical errors arose only from the differences between the recorded counting rates, and not from the rates themselves.

The measured results for the fractional difference in counting rate between the two units are shown in Fig. 4 as a function of counting rate, together with the expected result computed as mentioned above. (In this computation the

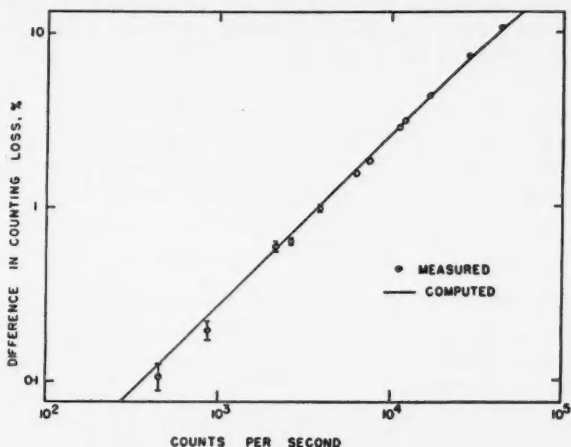


FIG. 4. Results of a test using random pulses. An appreciable memory loss in the resolver would cause the measured points to fall below the computed line at the higher counting rates.

result of the experiment has been anticipated by taking the counting rate as that of the resolver corrected for a dead time of 0.5 μ sec.) An appreciable memory loss in the resolver would make the measured points at high counting rates fall below the computed line. Within one per cent loss there is no such tendency at the highest measured rate, 44,000 counts per sec. At this rate the resolver was running at $nT = 0.26$, where from Fig. 1 the loss for a four-pulse memory is 0.037%, consistent with the experimental finding. At the same time the scaler was running at $n\tau = 0.14$ where its total loss was 12%. This crude experiment does not give a direct measurement of the memory loss of the resolver, but does verify that the resolver can raise the permissible counting rate of an ordinary scaler by a large factor.

I wish to thank Mr. Fred Jones for much patient work in bringing the circuit to its final form, and Dr. J. D. Jackson for valuable arguments about the computation of counting losses.

REFERENCES

- COOK-YARBOROUGH, E. H. 1947. Unpublished.
 ELMORE, W. C. 1950. *Nucleonics*, 6 (No. 1): 26.
 MOODY, N. F., HOWELL, W. D., BATTELL, W. J., and TAPLIN, R. H. 1951. *Rev. Sci. Instr.* 22: 439.

APPENDIX I. COUNTING LOSSES OF THE RESOLVER

We compute the probability, p_m , that the memory of the resolver contains m pulses at any given time, given that the memory capacity is k pulses. Calling the given time $t = 0$, we can call this probability $p_m(0)$. At time $t = T$ (i.e., one resolved time later) we have $p_m(T)$, which is the sum of the following probabilities, provided $m < k-2$:

that the memory contained no pulses at $t = 0$ and that m pulses arrived during T (none left during T if none were there at $t = 0$),

that the memory contained one pulse and that m pulses arrived during T (since there was something in the memory at $t = 0$, one pulse left during T),

that it contained two pulses and that $m-1$ pulses arrived during T , and so on up to

that it contained $m+1$ pulses and none arrived during T .

Under steady counting conditions p_m is not a function of time, and we have $p_m(0) = p_m(T) = p_m$. Writing $nT = x$, the above procedure yields the following set of equations for the p 's, with m going from 0 to $k-2$:

$$(7) \quad (m = 0) \quad p_0 = (p_0 + p_1)e^{-x},$$

$$(8) \quad (m = 1) \quad p_1 = [(p_0 + p_1)x + p_2]e^{-x},$$

$$(9) \quad (m = 2) \quad p_2 = [\frac{1}{2}(p_0 + p_1)x^2 + p_2x + p_3]e^{-x},$$

and so on up to $m = k-2$. This set of $k-1$ equations contains all the p 's up to p_{k-1} , and can be solved for p_1, \dots, p_{k-1} in terms of p_0 . The solutions for p_1, p_2 , and p_3 are as follows:

$$(10) \quad p_1 = p_0(e^x - 1),$$

$$(11) \quad p_2 = p_0e^x[e^x - (1+x)],$$

$$(12) \quad p_3 = p_0e^x[e^{2x} - (1+2x)e^x + x + \frac{1}{2}x^2],$$

it being understood that this solution for a given p_m is only meaningful when $k > m$. We have still not determined p_0 or p_k . The two equations needed to perform this solution are the necessary condition

$$(13) \quad \sum_{m=0}^k p_m = 1,$$

and

$$(14) \quad p_k = 1 - (1 - p_0)/x.$$

Equation (14) is an expression of the fact that the fraction of the time during which the gated oscillator is running is $(1 - p_0)$, and hence the number of counts registered per unit time is $(1 - p_0)/T$; the counting loss is therefore $n - (1 - p_0)/T$, or as a fraction, $1 - (1 - p_0)/nT = 1 - (1 - p_0)/x$. But the fractional counting loss is equal to the probability that the memory is full,

i.e. to p_k . Equation (14) follows. (It is possible to write an equation containing p_k in the manner of the set (7), (8), (9), but owing to the limiting action of the finite memory capacity the equation is algebraically complicated, and (14) is much simpler.)

For a given value of k there are $k+1$ probabilities p_m to be determined. The necessary $k+1$ equations consist of (13) and (14) and the first $k-1$ members of the sequence beginning with (10), (11), and (12). For $k=4$, for example, the complete set consists of equations (10) to (14) inclusive. We are interested finally in p_k , but it turns out to be easier to solve initially for p_0 . To do this we rewrite (13) as

$$(15) \quad \sum_{m=1}^{k-1} p_m = 1 - p_0 - p_k.$$

The left side of (15) is the sum of the sequence (10), (11), (12), ... to the appropriate number of terms, and contains only p_0 . The right side can be written in a form containing only p_0 by the use of (14). The resulting equation for p_0 alone reads as follows for the cases $k=2, 3$, and 4 :

$$(16) \quad p_0 = 1/(xe^x + 1), \quad (k=2)$$

$$(17) \quad p_0 = 1/(xe^{2x} - x^2e^x + 1), \quad (k=3)$$

$$(18) \quad p_0 = 1/(xe^{3x} - 2x^2e^{2x} + \frac{1}{2}x^3e^x + 1). \quad (k=4)$$

To compute the losses for a particular value of k we compute p_0 and then use

$$(19) \quad L_k = p_k = 1 - (1 - p_0)/x.$$

It is easily verified by expansion, at least for the above values of k , that for small $x = nT$,

$$(20) \quad L_k = (nT)^k/k!$$

in agreement with the leading term of (4).

For the trivial case $k=1$, equations (13) and (14) become respectively

$$(21) \quad p_0 + p_1 = 1, \quad (k=1)$$

and

$$(22) \quad p_1 = 1 - (1 - p_0)/x. \quad (k=1)$$

Solving these equations, one has immediately

$$(23) \quad p_1 = L_1 = x/(1+x) = nT/(1+nT), \quad (k=1)$$

in agreement with equation (3), verifying the expected fact that a resolver with a one-pulse memory is the same as a scaler of non-extending dead time T , for all values of nT .

For completeness, we write down the limiting form of the sequence (16) to (18) as the memory capacity k goes to infinity. In such a case there is no loss of pulses if $x \leq 1$, and we have from (19)

$$0 = 1 - (1 - p_0)/x,$$

hence

$$(24) \quad p_0 = 1 - x \quad (k = \infty, x \leq 1).$$

If $x \gg 1$, both (5) and (19) give the loss, so that

$$(x-1)/x = 1 - (1-p_0)/x,$$

hence

$$(25) \quad p_0 = 0 \quad (k = \infty, x \gg 1).$$

Equations (24) and (25) together constitute the limiting form of (16) to (18) as k becomes infinite.

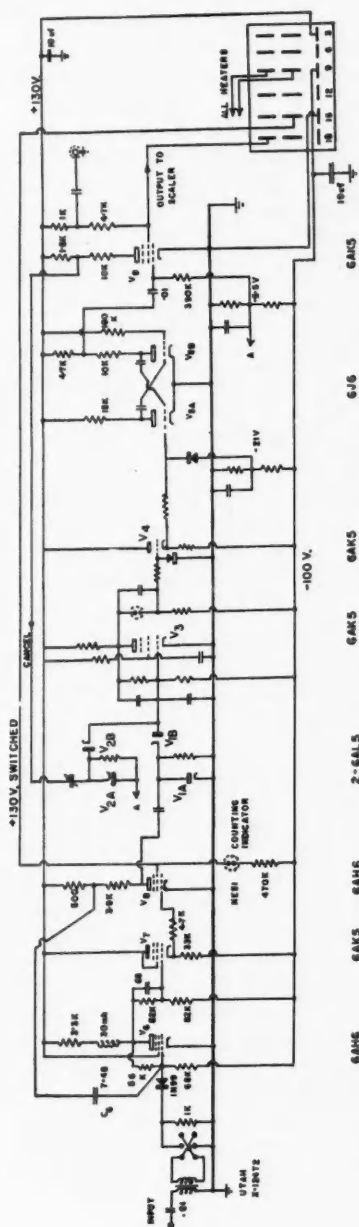
APPENDIX II. CIRCUIT OF A COMPLETE RESOLVER UNIT

The circuit diagram is shown in Fig. 5, drawn in the same form as the various functional units of the Chalk River-Marconi scaler in the paper by Moody *et al.* (1951). This unit is a direct replacement for the pulse shaper unit described there, except that no provision is made for a 60-cycle test.

The center section of the diagram (tubes V_1 to V_8 inclusive) is identical with Fig. 2 except that the cancel pulse to the integrator is brought back from a different point. The input to the complete unit goes to a pulse transformer (Utah X-124T2) fitted with a reversing switch so that pulses of either sign at the input may be converted to negative pulses for triggering the input univibrator. This univibrator (V_6, V_7, V_8) is a conventional one with the first tube current (V_6) stabilized by feedback resistors (56 K and 68 K). Shunt peaking is used in the anode circuit, and connection to the normally off tube of the univibrator is made via the cathode follower V_7 . This step prevents grid current charging of the coupling condenser. The circuit therefore shows no dead time; when two input pulses are brought steadily closer together, the output of the univibrator for the second pulse gradually merges with that for the first pulse, but at no point disappears except by coalescence with the first. The minimum duration of the pulse from the univibrator is set at 0.35 μ sec. by adjusting C_6 . The pentode V_8 (6AH6) "bottoms" during the pulse at about 75 volts, producing a relatively stable output pulse of 55 volts when the supply voltage is +130. The dead time performance of the whole unit is set by this input circuit rather than by the resolver itself.

At the output end of the unit, the pentode V_9 (6AK5) is held cut off by a fixed bias of -5.5 volts except during the 1.5 μ sec. positive pulses fed to it from the oscillator. While this pulse is on, the plate bottoms to about 30 volts (the screen voltage dropping by about 60 volts), producing a 100 volt pulse. Some 15 volts of this pulse is employed for the cancelling pulse to the integrator. Since both the input pulse and the cancelling pulse are supplied to the integrator from similar pentode circuits, a change in the unregulated positive supply voltage affects both pulses approximately equally. As a result the resolver circuit works correctly over a range of supply voltages of at least $\pm 10\%$ from nominal.

The output to the scaler is taken from the screen of V_9 . Counting is initiated and terminated by switching on and off the screen supply voltage of V_9 , thus starting and stopping the input univibrator. A neon bulb indicator on the front panel is also actuated by this switched voltage, showing when counting is in



progress. These provisions are copied from the original pulse shaper unit of this scaler. An additional plug is provided on which a pulse equal to about one sixth of the output pulse appears, for use with auxiliary equipment or as an inspection point.

The input sensitivity of this unit is about 1 volt, and it works well for input pulse lengths from 0.3 $\mu\text{sec.}$ upwards. (The output pulse from the univibrator $V_6V_7V_8$ extends with pulses longer than 0.35 $\mu\text{sec.}$) No testing has been done with pulses shorter than 0.3 $\mu\text{sec.}$ For long pulses, the rate of rise of the input pulse must be greater than about 0.15 volts per $\mu\text{sec.}$ to trip the input univibrator; this requirement includes any pulse shape normally used in the nuclear physics laboratory.

NUCLEAR QUADRUPOLE RESONANCE SPECTRUM OF B^{11} IN KERNITE¹

BY R. R. HAERING² AND G. M. VOLKOFF

ABSTRACT

The pure quadrupole resonance frequencies of B^{11} nuclei at two different sites (denoted by E and F) in a single crystal of kernite ($Na_2B_4O_7 \cdot 4H_2O$) have been determined both by observing the B^{11} resonances in zero external magnetic field, and also by investigating their Zeeman splitting in magnetic fields up to 30 gauss. The values obtained are 1281.1 ± 2 and 1287.0 ± 1 kc./sec. for the E and F sites respectively. These frequencies agree within experimental error with the values 1286 ± 4 and 1287 ± 3 kc./sec. predicted on the basis of studies in a magnetic field of 7000 gauss. The agreement for the F site is much better than for the E site. These zero field resonances have also been observed in a polycrystalline sample. The observed weak field Zeeman splitting for the single crystal agrees very well with that calculated from high field data for F sites, but at present disagrees with the corresponding calculation for E sites. A Na^{23} pure quadrupole resonance in kernite has also been measured at 1560.0 ± 1 kc./sec. The second Na^{23} resonance expected from high field work has not been observed to date.

1. INTRODUCTION

The work of Waterman and Volkoff (1955) at this laboratory carried out in a magnetic field of 7000 gauss has given a complete analysis of the quadrupole coupling tensors for B^{11} nuclei in kernite ($Na_2B_4O_7 \cdot 4H_2O$). This analysis showed that the B^{11} nuclei in kernite occur at four essentially different sites, which are repeated by a 180° rotation about the twofold symmetry axis of the crystal. The values of the asymmetry parameter and of the quadrupole coupling constant for each of these sites were derived from the high field observations, and the pure quadrupole frequencies expected in zero magnetic field were calculated. The predicted pure quadrupole resonance frequencies due to the B^{11} nuclei at the two sites with strong quadrupole coupling (denoted by E and F) are 1286 ± 4 and 1287 ± 3 kc./sec. Quite similar frequencies have been predicted independently by Proctor and co-workers (unpublished). A pure quadrupole resonance in kernite was first observed by Cranna (1954) at 1270 ± 10 kc./sec. with a superregenerative spectrometer. A later measurement by Proctor and co-workers (unpublished) gave 1279 ± 1 kc./sec. In both instances only one line was observed. It was decided to make a more detailed search to see whether the two predicted lines could be brought out separately, and a check obtained on the high field results. If the E and F site B^{11} pure quadrupole resonances occurred at the above predicted frequencies, then, because of line widths (about 15 kc./sec.), one could not expect to observe two resolved lines in zero magnetic field, or two pairs of resolved lines in very small magnetic fields. However, there is a possibility that the splitting of the two resonances by the magnetic field will be appreciably different in somewhat larger fields, and two pairs of resolved resonances should then be observed. Also, since the E

¹Manuscript received March 29, 1956.

Contribution from the Department of Physics, University of British Columbia, Vancouver, B.C. Work supported by grants from the National Research Council of Canada.

²Holder of National Research Council Bursary. Now at McGill University, Montreal, Que.

and F site nuclei are in nonequivalent positions with the principal axes of the field gradient tensor differently oriented, the transition probabilities for these two sites will be different functions of crystal orientation. Therefore there may exist certain orientations of the crystal for which any observed resonances are almost entirely due to one of these two sites. One might therefore expect to separate the contributions due to the E and F site B^{11} nuclei by suitable orientation of the crystal with respect to the spectrometer axes and the small perturbing magnetic field.

2. THEORY

The general case of the Zeeman splitting of a pure quadrupole resonance has been dealt with by Dean (1954). Only a brief summary of the theory needed to calculate the Zeeman splitting in weak magnetic fields of the pure quadrupole frequencies of B^{11} ($I = 3/2$) at E and F sites in kernite is given below. Since both the asymmetry parameter η and the perturbing magnetic field H_0 are small, it is convenient to consider the simultaneous perturbation of the axially symmetric pure quadrupole Hamiltonian by these two quantities.

The total Hamiltonian for the problem is

$$\mathfrak{H} = \frac{eQ\phi_{zz}}{4I(2I-1)}\{3I_z^2 - I^2 + \eta[I_x^2 - I_y^2]\} - g\beta_0 H_0[\alpha I_z + \beta I_y + \gamma I_x],$$

where α, β, γ are the direction cosines of the magnetic field H_0 relative to the principal axes of the electric field gradient tensor.

We break up the Hamiltonian as follows:

$$\mathfrak{H} = \mathfrak{H}_0 + \mathfrak{H}',$$

where

$$\mathfrak{H}_0 = \frac{eQ\phi_{zz}}{4I(2I-1)}\{3I_z^2 - I^2\},$$

$$\mathfrak{H}' = \frac{eQ\phi_{zz}}{4I(2I-1)}\eta[I_x^2 - I_y^2] - g\beta_0 H_0[\alpha I_z + \beta I_y + \gamma I_x].$$

The resulting first order energies are

$$(1) \quad \begin{aligned} W_{\pm 3/2} &= \frac{1}{4}eQ\phi_{zz} \pm g\beta_0 H_0\left(\frac{3}{2}|\gamma|\right), \\ W_{\pm 1/2} &= -\frac{1}{4}eQ\phi_{zz} \pm g\beta_0 H_0\left[\frac{1}{2}(4-3\gamma^2)^{1/2}\right]. \end{aligned}$$

The zero order wave functions corresponding to $W_{\pm 3/2}$ are the pure $m = \pm 3/2$ states, while the zero order wave functions corresponding to $W_{\pm 1/2}$ are linear combinations of the $m = \pm 1/2$ states with coefficients dependent on γ .

The lack of axial symmetry ($\eta \neq 0$) of the electric field gradient produces no first order effect. A second order calculation would lead to terms in η^2 , H_0^2 , and ηH_0 . In the present exploratory experiment the measurement of H_0 is not very accurate (5%) so that there is no point in keeping the small correction terms of order H_0^2 and $H_0\eta$. However, the η^2 term may be added to the expressions (1), since the accuracy of the frequency measurement (0.1%)

justifies a second order term, provided this term is independent of H_0 . The expressions (1) then become

$$(2) \quad \begin{aligned} W_{\pm 3/2} &= +\frac{1}{2}eQ\phi_{zz}[1+\frac{1}{2}\eta^2] \pm g\beta_0 H_0(\frac{3}{2}|\gamma|), \\ W_{\pm 1/2} &= -\frac{1}{2}eQ\phi_{zz}[1+\frac{1}{2}\eta^2] \pm g\beta_0 H_0[\frac{1}{2}(4-3\gamma^2)^{1/2}]. \end{aligned}$$

The expressions (2) predict the frequency shift of the perturbed quadrupole transitions in small magnetic fields for any given relative orientation of crystal and magnetic field H_0 . The required values of η , $eQ\phi_{zz}/h$, and γ are obtained from the high field analysis of Waterman and Volkoff (1955) and are listed in Tables I and II.

TABLE I

PURE QUADRUPOLE FREQUENCIES ν_0 AND ASYMMETRY PARAMETERS η FOR THE E AND F SITE B^{11} NUCLEI IN KERNITE (FROM WATERMAN AND VOLKOFF 1955)

Quadrupole coupling tensor parameters	At E sites	At F sites
$\nu_0 = \frac{eQ\phi_{zz}}{2h} [1 + \frac{1}{2}\eta^2]$, kc./sec.	1286 ± 4	1287 ± 3
$\eta \equiv (\phi_{xx} - \phi_{yy})/\phi_{zz}$	0.163 ± 0.010	0.117 ± 0.010

TABLE II

DIRECTION COSINES OF THE FIELD GRADIENT TENSOR PRINCIPAL AXES (x, y, z) WITH RESPECT TO X, Y, Z (CRYSTALLOGRAPHIC $b, b \times c, c$) AXES AT THE E AND F B^{11} SITES IN KERNITE (FROM WATERMAN AND VOLKOFF 1955)

The double signs refer to the pair of sites E_1, E_2 (and similarly F_1, F_2) related by a 180° rotation about the b symmetry axis

Sites	Axes	x	y	z
E_1	X	$-.76 \pm .04$	$-.60 \pm .03$	$-.21 \pm .01$
and	Y	$\mp (.22 \pm .03)$	$\mp (.05 \pm .01)$	$\mp (.97 \pm .02)$
E_2	Z	$\mp (.60 \pm .07)$	$\pm (.79 \pm .07)$	$\mp (.10 \pm .01)$
F_1	X	$-.05 \pm .03$	$-.94 \pm .04$	$+.340 \pm .005$
and	Y	$\pm (.92 \pm .04)$	$\pm (.09 \pm .03)$	$\pm (.368 \pm .005)$
F_2	Z	$\mp (.37 \pm .02)$	$\pm (.33 \pm .02)$	$\pm (.865 \pm .001)$

Table III gives the calculated low field spectrum for the E and F site B^{11} nuclei for the two cases when the crystallographic b -axis is perpendicular to H_0 and the crystallographic c -axis is either parallel or perpendicular to H_0 . The numerical values in Table III are based on the expressions (2), the data in Tables I and II, and the known value (1.367 kc./sec. per gauss) of $g\beta_0/h$ for B^{11} . In the approximation used for the previous calculation, the selection rule $\Delta m_z = \pm 1$ shows that the magnetic field splits the pure quadrupole line at each site into only two components (lines E_+ and E_- above and below the pure quadrupole frequency E_0 at the E sites, and similarly F_+ and F_- above and below F_0 at the F sites), the amount of splitting being directly proportional to H_0 and depending on the angle between H_0 and the z principal axis of the field gradient tensor.

TABLE III
PREDICTED LOW FIELD SPECTRUM FOR THE *E* AND *F* SITE B^{11} NUCLEI IN KERNITE
(Calculations based on data of Waterman and Volkoff 1955)

<i>b</i> -axis perpendicular to H_0			
<i>c</i> -axis parallel to H_0 , perpendicular to H_1		<i>c</i> -axis perpendicular to H_0 , parallel to H_1	
Frequency in kc./sec. (H_0 in gauss)		Frequency in kc./sec. (H_0 in gauss)	
<i>E</i> sites	$E_{\pm} = 1286 \pm 1.16H_0$ (weak)	$E_{\pm} = 1286 \pm 1.25H_0$ (strong)	
<i>F</i> sites	$F_{\pm} = 1287 \pm 0.86H_0$ (strong)	$F_{\pm} = 1287 \pm 0.54H_0$ (weak)	

The expected uncertainty arising from the experimental errors quoted in Tables I and II is not explicitly shown in Table III. These errors, together with the experimental error of the present experiment, are referred to in the discussion.

3. APPARATUS AND EXPERIMENTAL PROCEDURE

The apparatus used in this experiment is an r-f. spectrometer of the Bloch type. The apparatus closely resembles that described by Proctor (1950) and Weaver (1953). The derivative of the *u*-mode resonance (dispersion) was recorded most of the time, and occasionally compared with that of the *v*-mode (absorption).

Since the predicted *E* and *F* site B^{11} pure quadrupole resonances cannot be expected to be resolved because of line widths, one must make use of crystal orientation in order to untangle the low field spectrum of nuclei at these two sites. Under the action of a small magnetic field, the pure quadrupole resonance of B^{11} nuclei at a particular site (*E* or *F*) splits up into two resonances. Equations (2) show that for small magnetic fields this splitting is linear. Therefore, two pairs of resonances should be observed in the low field spectrum of the *E* and *F* site B^{11} nuclei. However, the intensity of these lines is strongly dependent on crystal orientation (Volkoff and Lamarche 1954), being a maximum when the long axis of the electric field gradient tensor is perpendicular to the r-f. field H_1 and a minimum when the two are parallel. For all measurements the *b*-axis of the crystal was along the receiver coil axis which is perpendicular to both H_0 and H_1 . Making use of the data in Table II, it may be shown that choosing the crystallographic *c*-axis perpendicular to H_1 strongly favors the *F* sites, while the *E* sites will be efficiently suppressed. When the *c*-axis is placed parallel to H_1 , the *E* sites will be favored. In this case, the *F* sites are not very efficiently suppressed, since their long axis does not lie parallel to H_1 in this orientation. In fact, because the *F* sites fall into two categories, F_1 and F_2 , (related by a rotation about a twofold symmetry axis) and because the angle between the long axes of F_1 and F_2 is appreciably different from 180° , it is impossible to suppress both *F* sites completely in any orientation. The reason is simply that if H_1 were chosen parallel to the long axis of one of the *F* sites, say F_1 , the long axis at the F_2 site would not be simultaneously parallel to H_1 , and hence a resonance could be expected.

Three methods of measuring the pure quadrupole frequencies now suggest themselves. They all depend upon crystal orientation for separating the *E* and *F* site resonances.

1. *Extrapolation Method Based on the Linearity of the Low Field Spectrum*

For small fields, the expressions (2) show that the spectrum is linear in H_0 . Hence a least square fit to the experimental points can be made. The common intersection of the best straight lines through the points with the line $H_0 = 0$ will give the pure quadrupole frequency.

2. *Method Based on Symmetry of Low Field Spectrum*

The theory shows that, for a given site, the low field spectrum is symmetric about the line $\nu = \nu_0$. Hence, in any given small field, in which two lines ν_+ and ν_- are observed, the estimated pure quadrupole frequency ν_0 is given by $\nu_0 = (\nu_+ + \nu_-)/2$. A series of measurements of ν_+ and ν_- in different fields can be made, and the resulting estimates of ν_0 are then averaged. This method does not require an accurate knowledge of H_0 for each pair of points.

3. *Direct Method*

The pure quadrupole frequencies can be measured directly in zero external magnetic field. Different crystal orientations are used to separate the *E* and *F* site contributions.

4. RESULTS

The low field spectrum due to the *E* and *F* site B^{11} nuclei in kernite was observed in order to establish the pure quadrupole frequencies due to nuclei at these two sites. In order to obtain both of these frequencies, two easily reproducible orientations of the crystal were used.

Figs. 1 and 2 are plots of the observed and predicted low field spectra of the *E* and *F* site B^{11} nuclei in kernite. Fig. 1 exhibits the results obtained with the crystallographic *c*-axis perpendicular to the r-f. field H_1 and parallel to the small d-c. field H_0 . The straight lines of Fig. 1 are plots of the expressions in the second column of Table III, the solid lines representing the expected strong resonances due to the B^{11} nuclei at the *F* sites and the dotted lines the expected weak resonances due to the B^{11} nuclei at the *E* sites. Similarly, Fig. 2 exhibits the results obtained with the *c*-axis parallel to H_1 and perpendicular to H_0 . Here the solid lines represent the expected strong resonances due to the B^{11} nuclei at the *E* sites, and the dotted lines the expected weak resonances due to the B^{11} nuclei at the *F* sites as listed in the last column of Table III.

The pure quadrupole frequencies of the *E* and *F* site B^{11} nuclei were measured by each of the three methods discussed earlier. The results of these measurements, together with the averaged pure quadrupole frequencies, are given in Table IV. The first two methods reported in Table IV make use of all the points plotted in Figs. 1 and 2 except those for $H_0 = 0$. These zero field points represent the results of the third method listed in Table IV.

All frequencies were measured with a BC221-A type frequency meter which had been previously calibrated against WWV. The uncertainties quoted in

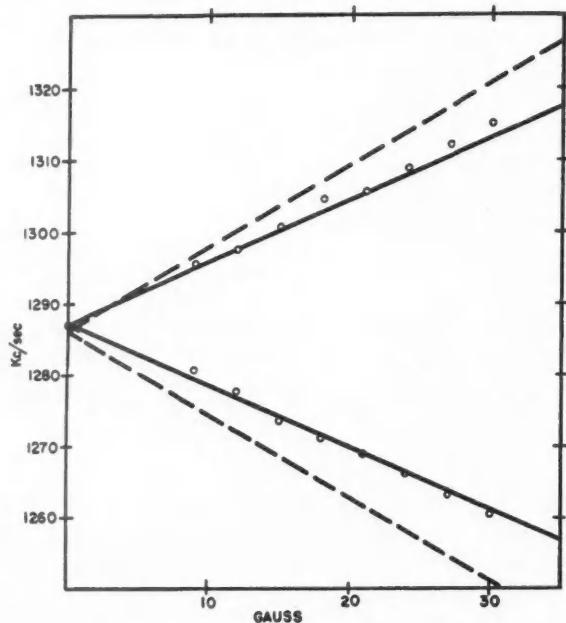


FIG. 1. Low field spectrum of B^{11} nuclei in kernite. Crystal c -axis perpendicular to H_1 and parallel to H_0 . Circles are the observed experimental points; solid and dotted lines are the expected strong B^{11} resonances at the F sites, and the weak resonances at the E sites respectively, calculated on the basis of the high field work of Waterman and Volkoff (1955). Since points fall on solid curves high and low field results are consistent for F sites.

TABLE IV
MEASURED PURE QUADRUPOLE FREQUENCIES OF B^{11} NUCLEI AT E AND F
SITES IN KERNITE
(All frequencies are in kc./sec.)

Method of determination	Site	
	E	F
Least square fit to low field spectrum	1282.0 ± 2	1286.7 ± 1
Symmetry of low field spectrum	1281.4 ± 2	1287.4 ± 1
Direct measurement in zero field	1280.0 ± 2	1286.8 ± 1
Average pure quadrupole frequency	1281.1 ± 2	1287.0 ± 1

Table IV are rather larger than the uncertainties in the actual frequency measurements, in order to make some allowance for systematic error introduced by impure modes and unresolved line structure.

Incomplete F site suppression has been mentioned earlier. In fields of about 30 gauss, this should lead to the presence of two additional weak lines in the spectrum of Fig. 2 which emphasizes the E sites. Only two lines were observed for this orientation. However, a slight asymmetry of the lines was noticed, which may indicate unresolved line structure.

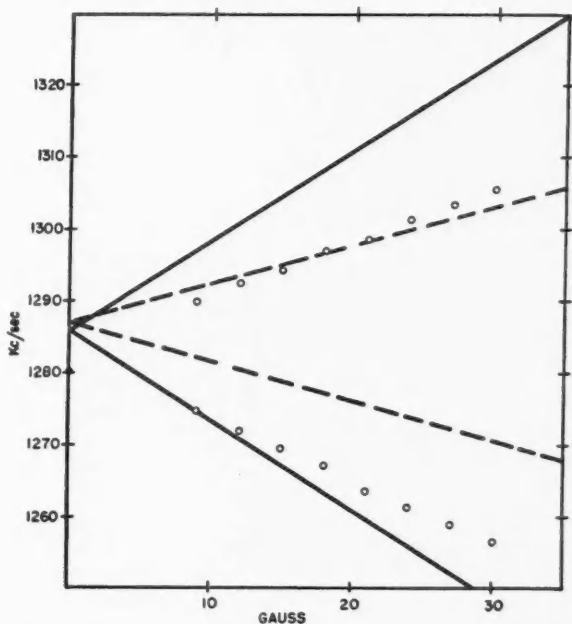


FIG. 2. Low field spectrum of B^{11} nuclei in kernite. Crystal c -axis parallel to H_1 and perpendicular to H_0 . Circles are the observed experimental points; solid and dotted lines are the expected strong B^{11} resonances for the E sites and the weak resonances for the F sites respectively, calculated on the basis of the high field work of Waterman and Volkoff (1955). Since points do not fall on solid curves high and low field results are at present not consistent for E sites.

A check on the presence of two nonequivalent nuclear sites can be made with a polycrystalline sample. A measurement in zero field with this sample resulted in a doubly peaked pure quadrupole resonance. The line peaks were measured to be 1280 and 1286 kc./sec. These values are in good agreement with the values given in Table IV.

An additional check can be obtained by making a measurement in an orientation with the c -axis at about 45° both to H_1 and to H_0 . The E and F sites are then approximately equally favored and four fairly weak resolved lines are observed in fields larger than about 30 gauss. The average frequency of the two members of an appropriate pair of lines again is in good agreement with the average value of the corresponding pure quadrupole frequency. Fig. 3(c) is a picture of a typical trace obtained in this intermediate orientation.

A pure quadrupole resonance due to Na^{23} in kernite has also been observed at 1560 ± 1 kc./sec. No change in this frequency was noted as the crystal was rotated about its b -axis. No evidence of the second Na^{23} resonance expected from high field work has been observed to date. Indications of the B^{10} resonance, which from the work of Dehmelt (1952) is expected at 1335 kc./sec., have been seen but the signal to noise ratio is in this case very poor (2:1).

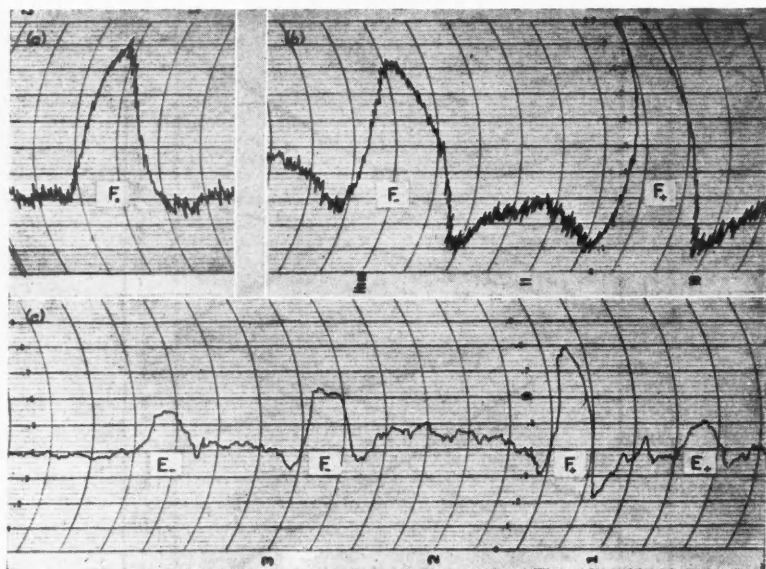


FIG. 3. Selected traces of the derivative of the u -mode B^{11} quadrupole resonances in a single crystal of kernite. (For all traces $H_{\text{mod}} \approx 5$ gauss.)

(a) c -axis perpendicular to H_1 ; $H_0 = 0$ gauss; time constant = 5 sec.; 1 chart division ≈ 8 kc./sec.; frequency of peak F_0 is 1287.0 kc./sec.

(b) c -axis perpendicular to H_1 and parallel to H_0 ; $H_0 = 30$ gauss; time constant = 5 sec.; 1 chart division ≈ 8 kc./sec.; frequencies of peaks: $F_- = 1260.2$ kc./sec.; $F_+ = 1312.8$ kc./sec.; $F_0 =$ average of F_- and $F_+ = 1286.5$ kc./sec.

(c) c -axis at approximately 45° to both H_0 and H_1 ; $H_0 = 45$ gauss; time constant = 20 sec.; 1 chart division ≈ 11 kc./sec.; frequencies of peaks: $E_- = 1208.0$ kc./sec.; $F_- = 1256.0$ kc./sec.; $F_+ = 1317.0$ kc./sec.; $E_+ = 1354.0$ kc./sec.; $E_0 =$ average of E_- and $E_+ = 1281.0$ kc./sec.; $F_0 =$ average of F_- and $F_+ = 1286.5$ kc./sec. The small narrower peak between F_+ and E_+ is probably a B^{10} line.

5. DISCUSSION

This experiment was designed as a check on the high field work on kernite carried out by Waterman and Volkoff (1955). Both the observed pure quadrupole frequency of B^{11} at the F site and its splitting in an applied weak magnetic field agree very well with the predictions made on the basis of the high field work as shown in Fig. 1. The zero field pure quadrupole frequency of B^{11} at the E site falls just barely within the quoted experimental uncertainty. The observed rate of increase in the splitting of this frequency with H_0 differs by about a factor of 2 from the predicted one, as may be seen by comparing the experimental points with the solid curves of Fig. 2. This discrepancy may be due to several causes. The high field results on the quadrupole coupling tensor for B^{11} at the E sites may be in error. It is possible that an error in the orientation of the principal axes of the field gradient tensor can be compensated by a corresponding error in the asymmetry parameter at high magnetic fields, with the compensation no longer holding at low fields. The values of H_0 in the

present exploratory experiment were not determined to better than 5%, and no particular pains were taken to align the crystal to better than two or three degrees. All the above points remain to be investigated more fully. If the discrepancy is not removed in this way, the possibility of asymmetric nuclear shielding mentioned by Waterman and Volkoff (1955) should be investigated. Further work is in progress.

ACKNOWLEDGMENTS

The authors would like to thank Dr. W. G. Proctor of the University of Washington and his group for several valuable discussions regarding this work and for communication of unpublished results. Thanks also go to the members of the Physics Department shop staff for their aid with the construction of the spectrometer. The support of the National Research Council in the form of a research grant to one of us (G. M. V.) and a Bursary to the other is gratefully acknowledged.

REFERENCES

- CRANNA, N. G. 1954. Ph.D. Thesis, University of British Columbia, Vancouver, B.C.
DEAN, C. 1954. *Phys. Rev.* **96**: 1053.
DEHMELT, H. G. 1952. *Z. Physik*, **133**: 528.
PROCTOR, W. G. 1950. *Phys. Rev.* **79**: 35.
PROCTOR, W. G. and co-workers. Unpublished.
VOLKOFF, G. M. and LAMARCHE, G. 1954. *Can. J. Phys.* **32**: 493.
WATERMAN, H. H. and VOLKOFF, G. M. 1955. *Can. J. Phys.* **33**: 156.
WEAVER, H. E. JR. 1953. *Phys. Rev.* **89**: 923.

LOW FREQUENCY RADIATION FROM A HORIZONTAL ANTENNA OVER A SPHERICAL EARTH¹

BY JAMES R. WAIT²

ABSTRACT

The problem of the radiation from a horizontal antenna at low radio frequencies over a spherical earth is discussed. The solution is facilitated by considering that the surface of the earth can be characterized by a boundary impedance. It is shown that, in general, both vertically and horizontally polarized waves are radiated along the surface of the earth. At short distances for a homogeneous earth, the expressions are in agreement with Norton's formulas for the radiation field of a horizontal dipole over a flat earth.

INTRODUCTION

The diffraction of electromagnetic waves by a spherical obstacle has been discussed by many authors. The classical papers by Mie (1908) and Debye (1909) formed the starting point for nearly all these analyses. An excellent summary of this earlier work is given by Stratton (1941) in his book. In connection with the propagation of radio waves over the surface of the earth, Watson (1918) developed a technique to evaluate the fields of a radially oriented dipole over a large sphere. His work was extended by Van der Pol and Bremmer (1937, 1938, 1939) and Gray (1939). This later work is discussed in detail by Bremmer (1949). He presents general formulas that can be used to calculate the ground wave field of vertical electric or magnetic dipoles over a homogeneous spherical earth.

It is interesting to note that Bremmer (1949) states in his book on many occasions that the field of a horizontal electric dipole in the *direction of maximum field* is proportional to the field of a vertical magnetic dipole. It will be shown here that this is not true in general. In fact, at low radio frequencies, the field radiated from a low horizontal antenna on a flat earth is predominantly vertically polarized (Norton 1937). To further support this contention, a solution is carried out for a horizontal dipole outside a sphere. This problem is intrinsically more complicated than for the case of radial dipoles since symmetry in the azimuthal direction is no longer present. A general method for treating problems of this type has been elegantly presented by Tai (1953) using dyadic Green functions. In the present instance it is more convenient, however, to employ scalar wave functions in a manner similar to that used by the author (1953a) in treating the induction of a conducting permeable sphere by a solenoidal coil.

SOLUTION FOR HORIZONTAL DIPOLE

The sphere is of radius a and is located at the center of a spherical coordinate system (r, θ, ϕ) . An electric dipole of moment p is located at $r = b$, $\theta = 0$, on the polar axis and directed towards increasing θ and is contained in the

¹Manuscript received February 13, 1956.

Contribution from the Department of Electrical Engineering, University of Toronto, Toronto, Ontario.

²Present address: National Bureau of Standards, Boulder, Colorado, U.S.A.

$\phi = 0$ plane. With reference to a usual cartesian coordinate system (x, y, z) , the dipole is located at $z = b$ and is oriented in the x direction as shown in Fig. 1.

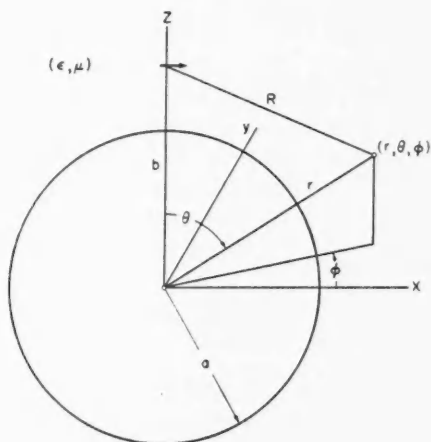


FIG. 1. Horizontal electric dipole outside a spherical body.

The primary field of the dipole, in the absence of the sphere, can be obtained from an electric Hertz vector which has only an x component given by

$$(1) \quad \pi_x^D = p e^{-ikR}/R$$

where R is the distance from the dipole to the observer and $k = 2\pi/\text{free space wavelength}$. The time factor $\exp(i\omega t)$ is implied. The components of the Hertz vector in the spherical coordinates are then

$$(2) \quad \begin{aligned} \pi_r^D &= p(e^{-ikR}/R) \cos \phi \sin \theta, \\ \pi_\theta^D &= p(e^{-ikR}/R) \cos \phi \cos \theta, \\ \pi_\phi^D &= -p(e^{-ikR}/R) \sin \phi. \end{aligned}$$

The primary field components can then be found from the relations

$$(3) \quad \begin{aligned} \mathbf{E}^D &= (k^2 + \text{grad div}) \boldsymbol{\pi}^D, \\ \mathbf{H}^D &= i\epsilon\omega \text{curl } \boldsymbol{\pi}^D, \end{aligned}$$

where ϵ is the dielectric constant of the homogeneous space surrounding the sphere. Unfortunately, the Hertz vector expressed in this form does not lend itself readily to the solution of the boundary value problem of the sphere. As shown originally by Debye (1909), it is more convenient to express the total field in terms of magnetic or H modes and electric or E modes which can be derived from two scalar functions W and V , respectively, as follows:

$$\begin{aligned}
 H_r &= \left(k^2 + \frac{\partial^2}{\partial r^2}\right)(rW) + 0, \\
 H_\theta &= \frac{1}{r} \frac{\partial^2}{\partial r \partial \theta}(rW) + \frac{i\epsilon\omega}{r \sin \theta} \frac{\partial}{\partial \phi}(rV), \\
 H_\phi &= \frac{1}{r \sin \theta} \frac{\partial^2}{\partial r \partial \phi}(rW) - \frac{i\epsilon\omega}{r} \frac{\partial}{\partial \theta}(rV), \\
 E_r &= 0 + \left(k^2 + \frac{\partial^2}{\partial r^2}\right)(rV), \\
 E_\theta &= -\frac{i\mu\omega}{r \sin \theta} \frac{\partial(rW)}{\partial \phi} + \frac{1}{r} \frac{\partial^2}{\partial r \partial \theta}(rV), \\
 E_\phi &= \frac{i\mu\omega}{r} \frac{\partial(rW)}{\partial \theta} + \frac{1}{r \sin \theta} \frac{\partial^2(rV)}{\partial r \partial \phi},
 \end{aligned}
 \tag{4}$$

where μ is the permeability of the surrounding space. The functions W and V satisfy the wave equation

$$(\nabla^2 + k^2) \frac{W}{V} = 0. \tag{5}$$

The first step in the solution of the problem is to find the functions W and V that will give rise to the primary field. These will be denoted W^p and V^p . The functions W and V can be written as a superposition of modes of the type

$$\begin{aligned}
 j_n(kr) & P_n^m(\cos \theta) \cos m\phi \\
 h_n^{(1),(2)}(kr) & \sin m\phi
 \end{aligned}
 \tag{6}$$

where m and n are integers. The radial functions are spherical Bessel functions* and P_n^m is an associated Legendre function.* In view of this fact, the primary field component can be expressed in terms of these spherical wave functions by performing the operation

$$H_r^p = i\epsilon\omega \operatorname{curl}_r \pi^p = \frac{i\epsilon\omega}{r \sin \theta} \left[\frac{\partial}{\partial \theta} \sin \theta \pi_\phi^p - \frac{\partial \pi_\theta^p}{\partial \phi} \right] \tag{7}$$

and using the addition theorem

$$\frac{e^{-ikR^*}}{R} = \sum_{n=0}^{\infty} D_n j_n(kr) P_n(\cos \theta), \quad \text{for } r < b, \tag{8}$$

where $D_n = -ik(2n+1)h_n^{(2)}(kb)$. The result is

$$H_r^p = +\frac{pi\epsilon\omega}{r} \sin \phi \sum_{n=1}^{\infty} D_n j_n(kr) P_n^1(\cos \theta), \tag{9}$$

where we have also used the relation

$$P_n^1(\cos \theta) = -\frac{\partial}{\partial \theta} P_n(\cos \theta). \tag{10}$$

*As defined by Stratton (1941).

It is now apparent that W^p must be of the form

$$(11) \quad W^p = \sin \phi \, p \sum_{n=1}^{\infty} a_n j_n(kr) P_n^1(\cos \theta)$$

corresponding to $m = 1$. Using equation (4) the equivalent form of H_r^p can be written

$$(12) \quad H_r^p = \sin \phi \, p \sum_{n=1}^{\infty} a_n \left(k^2 + \frac{\partial^2}{\partial r^2} \right) j_n(kr) r P_n^1(\cos \theta).$$

Noting that the differential equation satisfied by these spherical Bessel functions is

$$(13) \quad \left[k^2 + \frac{\partial^2}{\partial r^2} - \frac{n(n+1)}{r^2} \right] [j_n(kr) r] = 0,$$

it is seen that

$$(14) \quad H_r^p = \sin \phi \, p \sum_{n=1}^{\infty} a_n \frac{n(n+1)}{r} j_n(kr) P_n^1(\cos \theta).$$

On comparing equations (9) and (14), it follows that

$$(15) \quad a_n = \frac{\epsilon \omega (2n+1) k}{n(n+1)} h_n^{(2)}(kb).$$

With similar reasoning, and working with the E_r^p component, it can be shown that

$$(16) \quad V^p = \cos \phi \, p \sum_{n=1}^{\infty} b_n j_n(kr) P_n^1(\cos \theta),$$

where

$$(17) \quad b_n = \frac{-ik(2n+1)}{n(n+1)b} \left\{ \frac{d}{dx} [x h_n^{(2)}(x)] \right\}_{x=kb}.$$

The secondary fields, due to the presence of the sphere, can now be denoted by a superscript s . Remembering that V^s and W^s must give rise to outgoing waves at infinity, they are written in the form

$$(18) \quad W^s = p \sin \phi \sum_{n=1}^{\infty} a_n^s h_n^{(2)}(kr) P_n^1(\cos \theta)$$

and

$$(19) \quad V^s = p \cos \phi \sum_{n=1}^{\infty} b_n^s h_n^{(2)}(kr) P_n^1(\cos \theta),$$

where a_n^s and b_n^s are unknown coefficients. The potentials for the total field outside the sphere are then

$$(20) \quad \begin{aligned} W &= W^p + W^s, \\ V &= V^p + V^s. \end{aligned}$$

Since $2j_n(kr) = h_n^{(1)}(kr) + h_n^{(2)}(kr)$, it proves to be convenient to express the potentials in the following form before applying the boundary conditions:

$$\begin{aligned}
 (21) \quad W &= \frac{\rho \sin \phi}{2} \sum_{n=1}^{\infty} [a_n h_n^{(1)}(kr) + c_n h_n^{(2)}(kr)] P_n^1(\cos \theta), \\
 V &= \frac{\rho \cos \phi}{2} \sum_{n=1}^{\infty} [b_n h_n^{(1)}(kr) + d_n h_n^{(2)}(kr)] P_n^1(\cos \theta).
 \end{aligned}$$

The coefficients a_n and b_n are the same as given above. The new coefficients c_n and d_n are not yet determined.

APPLICATION OF THE BOUNDARY CONDITIONS

As pointed out in detail in another paper (Wait 1956), a great simplification is made if approximate boundary conditions are introduced. It is assumed that the tangential electric and magnetic fields are related by a complex constant of proportionality which can be termed the surface impedance. It readily follows that the boundary condition at the surface of the sphere can be stated

$$(22) \quad \left. \begin{aligned} \frac{1}{r} \frac{\partial}{\partial r} (rW) &= \frac{i\mu\omega}{Z^h} W \\ \frac{1}{r} \frac{\partial}{\partial r} (rV) &= Z^e i\epsilon\omega V \end{aligned} \right\} \quad r = a.$$

The surface impedance Z^e for the E modes is set equal to the surface impedance for a horizontally polarized wave at grazing incidence on a flat earth. The validity of this assumption was investigated and it was shown that the resulting error was negligible if the propagation constant ik_e in the ground was large compared to the propagation constant ik in the air. For a homogeneous earth

$$Z^h = \eta[1 - k^2/k_e^2]^{-\frac{1}{2}} \quad \text{with } \eta = \mu\omega/k_e.$$

Correspondingly, the surface impedance for the H modes is taken to be equal to the ratio of the tangential electric and magnetic fields for a vertically polarized wave at grazing incidence on a flat earth. Therefore

$$Z^e = \eta[1 - k^2/k_e^2]^{\frac{1}{2}}.$$

When the earth is stratified it is necessary to employ the appropriate form for the surface impedances Z^h and Z^e . Such expressions have been given previously (Wait 1953b).

On applying the boundary equations, the coefficients c_n and d_n can be expressed in terms of a_n and b_n , respectively. The potentials W and V are then given by

$$\begin{aligned}
 (23) \quad W &= \sin \phi \sum_{n=1}^{\infty} \frac{2n+1}{n(n+1)} f^h(n) P_n^1(\cos \theta), \\
 V &= \cos \phi \sum_{n=1}^{\infty} \frac{2n+1}{n(n+1)} f^e(n) P_n^1(\cos \theta),
 \end{aligned}$$

where

$$(24) \quad f^h(n) = \frac{\rho k^3}{2\mu\omega} h_n^{(2)}(kb) \left[h_n^{(1)}(kr) - \frac{R_n^h h_n^{(2)}(kr) h_n^{(1)}(ka)}{h_n^{(2)}(ka)} \right]$$

and

$$(25) \quad f^e(n) = -\frac{ipk}{2b} \left[\frac{\partial}{\partial y} [y h_n^{(2)}(y)] \right]_{y=kb} \times \left[h_n^{(1)}(kr) - \frac{R_n^e h_n^{(2)}(kr) h_n^{(1)}(ka)}{h_n^{(2)}(ka)} \right]$$

where

$$(26) \quad R_n^h = \left(\frac{d}{dx} \log [x h_n^{(1)}(x)] - i\Delta^h \right) / \left(\frac{d}{dx} \log [x h_n^{(2)}(x)] - i\Delta^h \right)$$

and

$$(27) \quad R_n^e = \left(\frac{d}{dx} \log [x h_n^{(1)}(x)] - i\Delta^e \right) / \left(\frac{d}{dx} \log [x h_n^{(2)}(x)] - i\Delta^e \right)$$

with $\Delta^h = \eta_0/Z^h$, $\Delta^e = Z^e/\eta_0$, and $\eta_0 = \mu\omega/k = 120\pi$. The radial fields are then expressible in the form

$$(28) \quad H_r = -\frac{1}{r} \sin \phi \frac{\partial}{\partial \theta} \sum_{n=0}^{\infty} (2n+1) f^h(n) P_n(\cos \theta)$$

and

$$(29) \quad E_r = -\frac{1}{r} \cos \phi \frac{\partial}{\partial \theta} \sum_{n=0}^{\infty} (2n+1) f^e(n) P_n(\cos \theta),$$

where the differential equation satisfied by the spherical Bessel function has again been made use of. The form of these infinite series is identical to that of the ones occurring in the corresponding development for the vertical electric dipole (Bremmer 1949). Furthermore, in view of the fact that $f^e(n - \frac{1}{2})$ and $f^h(n - \frac{1}{2})$ are even functions of n , the above series formulas for H_r and E_r can be converted to a more rapidly converging series via the Watson transformation, to yield

$$(30) \quad \eta_0 H_r = 2\pi i \sin \phi \frac{k^2 p}{(ka)^3} \frac{\partial}{r \partial \theta} \sum_{s=0,1,2,\dots} \frac{(\nu_s + \frac{1}{2})}{\sin \pi \nu_s} \times \frac{h_{\nu_s}^{(2)}(kr) h_{\nu_s}^{(2)}(kb)}{[h_{\nu_s}^{(2)}(ka)]^2 \left[\frac{\partial M^h(\nu)}{\partial \nu} \right]_{\nu=\nu_s}} P_{\nu_s}[\cos(\pi - \theta)]$$

and

$$(31) \quad E_r = 2\pi \cos \phi \frac{pk^2}{kb(ka)^3} \frac{\partial}{r \partial \theta} \sum_{s=0,1,2,\dots} \frac{(\nu_s + \frac{1}{2})}{\sin \pi \nu_s} \times \frac{[\partial y h_{\nu_s}^{(2)}(y)/\partial y]_{y=kb} h_{\nu_s}^{(2)}(kr)}{[h_{\nu_s}^{(2)}(ka)]^2 [\partial M^e(\nu)/\partial \nu]_{\nu=\nu_s}} P_{\nu_s}[\cos(\pi - \theta)],$$

where

$$(32) \quad M^{h,e}(\nu) = \left[\frac{d}{dx} \log x h_{\nu}^{(2)}(x) - i\Delta^{h,e} \right]_{x=ka}.$$

The summation is over the values ν_s which are the roots of the equations $M^{h,e}(\nu) = 0$. In the distant field, such that $D (=a\theta)$ is large compared to the

wavelength, it follows that the leading term of the asymptotic expansion for P_{ν_s} can be used. This is given by (Bremmer 1949)

$$(33) \quad P_{\nu_s}[\cos(\pi - \theta)] \approx \frac{\exp[i(\nu_s + \frac{1}{2})(\pi - \theta) - i\pi/4] + \exp[-i(\nu_s + \frac{1}{2})(\pi - \theta) + i\pi/4]}{[2\pi(\nu_s + 1) \sin \theta]^{\frac{1}{2}}}.$$

Utilizing the fact that $\nu_s(\pi - \theta)$ has a large negative imaginary part (Bremmer 1949) it can be seen that the second exponential term in the numerator is negligible. Furthermore, $\sin \nu_s \pi$ can be approximated by $-i \exp(+i\nu_s \pi)/2$. Also it can be assumed that the ratios b/a and r/a are near unity. The radiation fields can now be expressed in the following compact form, for a dipole of moment $I ds$:

$$(34) \quad E_\phi = \eta_0 H_r = \frac{I ds i \mu \omega \sin \phi}{2\pi D} U^h e^{-ikD},$$

$$(35) \quad E_r = -\eta_0 H_\phi = \frac{I ds i \mu \omega \cos \phi}{2\pi D} \Delta^e U^e e^{-ikD},$$

where

$$(36) \quad U^{h,e} = \sqrt{-2\pi i \chi} \sum_s f_s^{h,e}(h_1) f_s^{h,e}(h_2) \frac{\exp(-i\tau_s \chi)}{2\tau_s - 1/\delta^2}$$

with

$$\chi = (ka)^{1/3} \theta, \quad \tau_s = (\nu_s - ka)/(ka)^{1/3},$$

and

$$\delta = -i/(ka)^{1/3} \Delta^{h,e}.$$

The "height gain" functions are given by*

$$(37) \quad f_s^{h,e}(h_1) = \frac{h_{\nu_s}^{(2)}(kr)}{h_{\nu_s}^{(2)}(ka)}, \quad h_1 = r - a,$$

$$(38) \quad f_s^{h,e}(h_2) = \frac{h_{\nu_s}^{(2)}(kb)}{h_{\nu_s}^{(2)}(ka)}, \quad h_2 = b - a,$$

and

$$(39) \quad f_s^e(h_2) = \left[\frac{\partial}{\partial y} y h_{\nu_s}^{(2)}(y) \right]_{y=kb} / \left[\frac{\partial}{\partial y} y h_{\nu_s}^{(2)}(y) \right]_{y=ka}.$$

These height functions approach unity as h_1 and h_2 approach zero. The determination of the coefficients ν_s for the E and H modes must be obtained from equation (32). A method for doing this has been described in detail by Bremmer (1949). Furthermore, the height gain functions $f_s^h(h_1)$, $f_s^h(h_2)$, and $f_s^e(h_1)$ are identical in form to those treated by Bremmer (1949) for vertical source dipoles. The height gain function $f_s^e(h_2)$ on the other hand does not occur in the solutions for either the vertical electric or the vertical magnetic dipole. Surprisingly enough, $f_s^e(h_2)$ can be expressed in simple form. For example, if the numerator on the right-hand side of equation (39) is expanded in a Taylor series about $h_2 = 0$ it follows that

$$(40) \quad f_s^e(h_2) = \exp(i\Delta^e kh_2),$$

*It is to be understood that the values of ν_s , in general, are different for the H and E modes.

where repeated use has been made of equation (32), enabling the series to be summed. For small heights, these gain functions can all be approximated by (Bremmer 1949; Wait 1956)

$$f_s^{e,h}(h_i) \simeq 1 + i\Delta^{e,h} kh_i \quad (i = 1 \text{ or } 2).$$

The functions U^h and U^e , occurring in equations (34) and (35), can be represented in the following alternative form:

$$(41) \quad U^{e,h} = G \{ F(\rho) - \frac{1}{2}\delta^3 [1 - i(\pi\rho)^{\frac{1}{2}} - (1+2\rho)F(\rho)] \\ + \delta^6 [1 - i(\pi\rho)^{\frac{1}{2}}(1-\rho) - 2\rho + \frac{5}{6}\rho^2 + (\frac{1}{2}\rho^2 - 1)F(\rho)] \\ + \text{terms containing } \delta^9, \delta^{12}, \text{ etc.} \},$$

where

$$(42) \quad F(\rho) = 1 - i2\rho^{\frac{1}{2}}e^{-\rho} \int_{\rho^{\frac{1}{2}}}^{\infty} e^{-x^2} dx$$

with

$$\rho = -\frac{1}{2}ikD[\Delta^{e,h}]^2,$$

$$G \simeq (1 + i\Delta^{e,h} kh_1)(1 + i\Delta^{e,h} kh_2),$$

and

$$\delta = -i/(ka)^{1/3} \Delta^{e,h}.$$

This type of expansion in powers of δ^3 was first invented by Bremmer (1949) in connection with the radiation from a vertical dipole on a gently curved homogeneous ground. The technique has been recently generalized and extended by the present author (1956) in collaboration with Dr. Bremmer.

It is very significant to note that equations (34) and (35), when used in conjunction with equation (41) in the limiting case of $\delta = 0$, correspond to the formulas of Norton (1937) for the radiation fields of a horizontal electric dipole over a flat earth. The agreement with Norton's formulas is complete even to the extent of the definitions of the numerical distance ρ .

In the case where the source is a horizontal antenna of finite length, the fields are obtained by an integration of the horizontal dipole formulas. For an antenna of length L , which is considered to be small compared to D , it readily follows that the fields are given by

$$(43) \quad E_r = \frac{i\mu\omega \cos \phi}{2\pi D} e^{-ikD} \Delta^e U^e I_0 S(\phi)$$

and

$$(44) \quad E_\phi = \frac{i\mu\omega \sin \phi}{2\pi D} e^{-ikD} U^h I_0 S(\phi),$$

where I_0 is the current at the terminals of the antenna and $S(\phi)$ is a space factor. In the case where the heights h_1 and h_2 are small compared to D , the space factor is given by

$$(45) \quad S(\phi) = \int_{-L/2}^{L/2} \frac{I(x)}{I_0} \exp(ikx \cos \phi) dx,$$

where $I(x)$ is the current on the antenna. For very short antennas, such that $kL \ll 1$, equations (43) and (44) reduce to the horizontal dipole formulas since

$$S(\phi) \simeq (\bar{I}/I_0)L$$

where \bar{I} is the average current on the antenna. In the case of a thin center-fed wire antenna with a sinusoidal current being assumed, the space factor is

$$(46) \quad S(\phi) = \frac{\lambda}{\pi \sin^2 \phi} \left[\cos\left(\pi \frac{L}{\lambda} \cos \phi\right) - \cos\left(\pi \frac{L}{\lambda}\right) \right];$$

for a half-wave antenna, this reduces to

$$S(\phi) = \frac{\lambda}{\pi \sin^2 \phi} \cos\left(\frac{\pi}{2} \cos \phi\right).$$

It is of interest to examine the ratio E_ϕ/E_r of the radiated field. This actually describes the state of polarization of the wave. From equations (43) and (44) it is seen that

$$(47) \quad E_\phi/E_r = \tan \phi (U^h/\Delta^e U^e).$$

For a flat earth, with $h_1 = h_2 \simeq 0$,

$$U^h \simeq -1/2\rho^h \quad \text{and} \quad U^e \simeq F(\rho^e),$$

so that

$$\left| \frac{E_\phi}{E_r} \right| = \frac{\tan \phi}{kD \Delta^e (\Delta^h)^2 F(\rho^e)}.$$

At large distances such that $|\rho^e| \gg 1$, $F(\rho^e) \simeq -1/2\rho^e$, and then

$$\left| \frac{E_\phi}{E_r} \right| \simeq \tan \phi \left| \frac{\Delta^e}{(\Delta^h)^2} \right|.$$

At low radio frequencies, $\Delta^e \simeq \eta/\eta_0$ and $\Delta^h \simeq \eta_0/\eta$, so that

$$\left| \frac{E_\phi}{E_r} \right| \simeq \left| \frac{\eta}{\eta_0} \right|^3 \tan \phi.$$

Since the quantity $|\eta/\eta_0|^3$ is small, the field is predominantly vertically polarized except where ϕ is near 90° .

At shorter distances where the attenuation of the vertically polarized waves is small ($|\rho^e| \ll 1$), then

$$U^e \simeq F(\rho^e) \simeq 1$$

and consequently for low radio frequencies

$$\left| \frac{E_\phi}{E_r} \right| \simeq \left| \frac{\eta}{\eta_0} \right| \frac{\tan \phi}{kD},$$

which is also a very small quantity except in a very small region near $\phi = 90^\circ$.

In general it is necessary to examine the residue series for U^e and U^h in order to describe the complex polarization factor E_ϕ/E_r . At higher frequencies and greater antenna heights, the E_ϕ component becomes comparable to E_r .

CONCLUDING REMARKS

It is believed this analysis demonstrates conclusively that a horizontal antenna radiates both vertically and horizontally polarized ground waves over

a spherical earth. In the particular case of low radio frequencies, the horizontally polarized component has a negligible magnitude as was pointed out originally by Norton (1937).

REFERENCES

- BREMMER, H. 1949. Terrestrial radio waves. Elsevier Pub. Co., New York.
DEBYE, P. 1909. Ann. Physik, **30**: 57.
GRAY, M. C. 1939. Phil. Mag. **27**: 421.
MIE, G. 1908. Ann. Physik, **25**: 377.
NORTON, K. A. 1937. Proc. Inst. Radio Engrs. **25**: 1203.
STRATTON, J. A. 1941. Electromagnetic theory. McGraw-Hill Book Company, Inc., New York.
TAI, C. T. 1953. Tech. Rept. No. 41, Stanford Research Institute, Stanford, Calif.
VAN DER POL, B. and BREMMER, H. 1937. Phil. Mag. **24**: 857.
——— 1938. Phil. Mag. **25**: 817.
——— 1939. Phil. Mag. **27**: 261.
WAIT, J. R. 1953a. Can. J. Phys. **31**: 670.
——— 1953b. Geophysics, **18**: 416.
——— 1956. J. Research Natl. Bur. Standards. In press.
WATSON, G. N. 1918. Proc. Roy. Soc. (London), A, **95**: 83.

ABSORPTION SPECTRA OF BENZENE AND BENZENE- d_6 IN THE VACUUM ULTRAVIOLET¹

By P. G. WILKINSON

ABSTRACT

The absorption spectra of benzene and benzene- d_6 have been photographed from 1300Å to 1850Å in the first order of a 21-ft. normal incidence vacuum spectrograph. The band analysis resulted in the identification of four Rydberg series (over one hundred vibrational bands) in each molecule, converging to ionization potentials of 9.247 ev. (benzene) and 9.251 ev. (benzene- d_6). Progressions of the ν_2 , ν_{18} , and ν_{20} vibrations are associated with most of the 31 observed Rydberg transitions, and vibrational constants are tabulated for each. The strong intensity and the unusual length of the upper state ν_{18} (e_{2g}) progression in comparison with the $\nu_2(a_{1g})$ progression are interpreted in terms of the Jahn-Teller theorem, and it is concluded that the stable equilibrium nuclear configuration in the Rydberg states is of D_{2h} symmetry.

I. INTRODUCTION

The absorption spectrum of benzene in the vacuum ultraviolet may be divided into three regions: (1) a diffuse region from 1850Å to 2000Å, which has been classified as due to the forbidden transition, $^1B_{1u}-^1A_{1g}$, made allowed by vibrations of the type e_{2g} and b_{2g} (Nordheim, Sponer, and Teller 1940); (2) a strong apparent continuum with maxima at 1781Å and 1804Å, which is interpreted as the allowed $^1E_{1u}-^1A_{1g}$ transition (Mulliken 1939; Roothaan and Mulliken 1948); (3) an extensive series of Rydberg transitions, the first member of which lies at 1788Å (superposed on the continuum), extending to the ionization limit at 1340Å.

The absorption spectra of benzene and benzene- d_6 were first photographed by Price and co-workers (1935, 1947) from 1000Å to 2000Å, and two Rydberg series were identified leading to an ionization potential of 9.24 ev. Absorption coefficients of benzene vapor were determined in the region 1700Å to 2100Å by Morton and Stubbs (1940), Pickett *et al.* (1951), and Romand and Vodar (1951) by photographic methods. More recently, absorption coefficients have been determined photoelectrically by Jones and Taylor (1955) and Hammond and Price (1955) in the 1500Å to 2100Å region, and by Zelikoff (unpublished) from 1050Å to 2000Å.

In the present work, benzene and benzene- d_6 were photographed in the 1300Å to 1850Å region under high dispersion. From these new photographs, it has been possible to classify nearly all the observed bands and to make new estimates of the ionization potentials and vibrational constants.

II. EXPERIMENTAL

The light sources used to produce the continuous background were the xenon continuum from 1500Å to 1900Å (Wilkinson and Tanaka 1955) and the krypton continuum from 1250Å to 1600Å (Wilkinson 1955b). Atomic impurity lines, mainly CI, NI, and OI, occurring in these sources, were used as wave-

¹Manuscript received February 16, 1956.

Contribution from the Laboratory of Molecular Structure and Spectra, Department of Physics, The University of Chicago, Chicago 37, Illinois, U.S.A.

length standards (Wilkinson 1955*a, b*). The photographs were taken on a 21-ft. normal incidence vacuum grating spectrograph with a dispersion of 1.3 Å/mm. in the first order using Eastman "SWR" photographic plates (Wilkinson and Mulliken 1955). Since there was no possibility of resolving rotational structure, slit widths of 20 μ and 50 μ were used which are wider than the optimum opening (10 μ) for maximum resolving power (100,000).

The benzene used was vacuum distilled Merck and Co. reagent grade material; the benzene- d_6 was a sample kindly loaned by Dr. L. C. Leitch of the National Research Council (Canada) which analyzed 78% C_6D_6 , the principal impurities being C_6D_5H and $C_6D_4H_2$. In most of the experiments, an absorption cell, 17 cm. long, was placed between the spectrographic slit and the light source; the benzene vapor was flowed through the cell at pressures varying from a few microns to 3 mm. In a few experiments, benzene vapor was admitted to the body of the spectrograph during the exposure (path length about 13 meters).

The error in determining the position of the peak of an absorption band varied between 2 and 10 cm^{-1} and was a function of the relative sharpness of the bands.² In general, the positions of the stronger bands agreed well (within $\pm 10\text{ }cm^{-1}$) with those given by Price and Wood (1935) except for a few in the region below 1400 Å. Many of the weaker bands were not reported by Price and Wood and were found only when higher pressure was used.

III. THEORY

The ground state nuclear configuration of benzene belongs to point group D_{6h} (Herzberg 1945), and it is reasonable to expect the Rydberg nuclear configuration to belong to D_{6h} also, since only one weakly bonding electron of a total of 18 bonding electrons has been excited. (This neglects the Jahn-Teller effect which will be discussed in Section V.B.) Of the 20 ground state fundamentals, 10 are degenerate and 10 non-degenerate. Of these, 11 have been observed experimentally and most of the others have been calculated by normal coordinate treatments (Herzberg 1945). The symmetry of the vibrationless ground state is $^1A_{1g}$ and the only allowed transitions are to states of symmetry $^1E_{1u}$ and $^1A_{2u}$ (Sponer and Teller 1941); since the Rydberg transitions are quite strong, it is reasonable to attribute these to either $^1E_{1u} \leftarrow ^1A_{1g}$ or $^1A_{2u} \leftarrow ^1A_{1g}$.

For allowed transitions between electronic states in which the symmetry of the equilibrium nuclear positions is the *same* in both (Sponer and Teller 1941), only totally symmetrical vibrations are expected to appear strongly with the selection rule $\Delta v = 0, 1, 2, 3$ etc., while non-totally symmetric vibrations may sometimes appear with weakened intensity and according to the selection rule $\Delta v = 0, 2, 4$, etc. This means, in general, that only the non-totally symmetric 0-0, 1-1, . . . $v-v$ transitions will be strong but those with higher v''

²The use of the absorption maxima as band origins seems the most logical compromise since many of the bands were quite sharp and symmetrical. The peak positions were quite reproducible while any other choice, such as the short wavelength band edge, would be considerably more arbitrary.

will be weakened owing to Boltzman factors. The transitions 2-0, 4-0, etc. would be expected to be relatively weak from the following considerations. If one assumes harmonic vibrations, it is easy to show (Nordheim *et al.* 1940; Sponer and Teller 1941) that the intensity ratio for changes in quanta of non-totally symmetric vibrations is as follows:

$$(1) \quad \frac{I_{00}}{\sum_v I_{v0}} = \frac{2(\nu'\nu'')^{\frac{1}{2}}}{(\nu' + \nu'')},$$

where I_{00} is the intensity of the 0-0 band, $\sum_v I_{v0}$ is the sum of the intensities of all the v -0 bands, and ν' and ν'' are the vibrational frequencies in the upper and lower states, respectively. Even when the upper state frequency is considerably smaller than that in the ground state, equation (1) predicts that nearly all the intensity will be concentrated in the 0-0 band. However, when the upper state geometry differs from the ground state, the intensity of the 2-0, 4-0, etc. transitions may be considerably changed. A well-known example of an effect such as this probably occurs in ethylene (Wilkinson and Mulliken 1955).

In the case of a forbidden transition made allowed by excitation of a degenerate vibration (e.g. e_{2g} in the case of the near ultraviolet bands of benzene (Nordheim *et al.* 1940; Sponer and Teller 1941; Sponer *et al.* 1939)), the predictions are somewhat different in that now no 0-0 band will be observed and v -0 transitions of the totally symmetrical as well as of the non-totally symmetrical vibrations are possible. In the ${}^1B_{2u} \rightarrow {}^1A_{1g}$ (near ultraviolet) bands of benzene, upper state spacings of 923 cm^{-1} are found which are attributed to the ν_2 (a_{1g}) totally symmetrical C-C vibration (992 cm^{-1} in the ground state). In addition, the totally symmetric C-H vibration ν_1 (a_{1g}), the non-totally symmetric vibrations ν_{18} (e_{2g}), ν_{20} (e_{2u}), and ν_{16} (e_{2g}) may also be identified. These have values of 2565, 520, 240, and 1480 cm^{-1} , respectively, in the ${}^1B_{2u}$ state (3062, 606, 404, 1596 cm^{-1} , respectively, in the ground state). The ground state vibrations ν_{18} and ν_{20} occur also as "hot bands" and combination bands.

In the Rydberg bands of benzene, one may expect to find strong v -0 bands of the totally symmetric ν_2 vibration; "hot bands", 1-1, 2-2, . . . v - v , of the non-totally symmetric low frequency vibrations (ν_{18} and ν_{20}); and weak bands of at least some of the non-totally symmetrical vibrations as 2-0, 4-0, etc. progressions; and combination bands of some of these same vibrations. Since the electron excited is a π electron, no C-H vibration would be expected.

IV. EXPERIMENTAL DATA

The observed absorption bands are given in Table I for benzene and benzene- d_6 and most of these may be found in the microphotometer tracings of Figs. 1, 2, 3, and 4 (in each of these the pressure increases from A to C). With the present resolving power no rotational structure is observed. These data indicate Rydberg transitions converging to the ionization potential of 74587 cm^{-1} (9.247 ev.) and, associated with each electronic transition, vibrational structure may be observed. Tentatively, we have identified four different such Rydberg series and have named them (Figs. 1, 2, 3, 4) as follows: R - A ,

TABLE I

ABSORPTION BANDS OF BENZENE AND BENZENE- d_6

See Part IV of text for explanation of notation (D—diffuse band)

Benzene				Benzene- d_6			
Int.	λ , Å	ν , cm $^{-1}$	Transition	Int.	λ , Å	ν , cm $^{-1}$	Transition
500	1804.12	55429	$E-A^i$				
5	1797.99	55618	$2R_{002}-A_{002}$	15	1795.28	55702	$2R_{002}-A_{002}$
			$2R_{010}-A_{010}$				$2R_{010}-A_{010}$
10	1795.50	55695	$2R_{002}-A_{002}$	10	1792.73	55781	$2R_{002}-A_{002}$
60	1792.33	55793	$2R_{001}-A_{001}$	60	1789.98	55866	$2R_{001}-A_{001}$
500	1789.51	55881	$2R_{000}-A_{000}$	500	1787.44	55946	$2R_{000}-A_{000}$
500	1781.5	56132	$E-A^i$	500	1770.83	56471	$E-A^i$
20	1769.84	56502	$2R_{021}-A_{001}$	30	1768.60	56542	$2R_{021}-A_{001}$
60	1766.68	56603	$2R_{020}-A_{000}$	60	1765.65	56636	$2R_{020}-A_{000}$
15	1764.22	56682	$2R_{102}-A_{002}$	15	1763.89	56693	$2R_{102}-A_{002}$
30	1761.60	56767	$2R_{101}-A_{001}$	30	1760.95	56788	$2R_{101}-A_{001}$
60	1758.94	56852	$2R_{100}-A_{000}$	60	1758.59	56864	$2R_{100}-A_{000}$
3	1737.98	57538	$2R_{120}-A_{000}^*$	3	1737.48	57555	$2R_{120}-A_{002}$
10	1735.20	57630	$2R_{202}-A_{002}$	10	1734.56	57652	$2R_{201}-A_{001}$
2D	1731.87	57741	$2R_{201}-A_{001}$	2D	1731.45	57755	$2R_{200}-A_{000}$
2D	1729.46	57822	$2R_{200}-A_{000}$	2D	1726.86	57908	
				2D	1723.45	58020	
2D	1721.90	58075		2D	1719.94	58142	
5D	1717.46	58226		5D	1714.50	58326	
10D	1672.37	59795	$2R_{000}-A_{000}$	Not observed ^a			$2R_{000}-A_{000}$
2D	1654.91	60426	$2R_{020}-A_{000}$	2D	1657.33	60338	$2R_{020}-A_{000}$
3D	1635.78	61138	$2R_{040}-A_{000}$	3D	1640.44	60959	$2R_{040}-A_{000}$
				Not observed			$2R_{000}-A_{000}^b$
1D	1628.11	61421	$2R_{000}-A_{000}$	1D	1624.54	61556	$2R_{000}-A_{000}$
2D	1618.06	61802	$2R_{000}-A_{000}$				
1D	1610.44	62095	$2R_{020}-A_{000}^*$	1D	1616.14	61876	$2R_{020}-A_{000}$
1	1554.79	64317	$2R_{001}-A_{001}$	1D	1555.35	64294	$2R_{001}-A_{001}$
3	1553.11	64387	$2R_{000}-A_{000}$	3	1553.71	64362	$2R_{000}-A_{000}$
3	1536.94	65064	$2R_{020}-A_{000}$	1D	1538.71	64990	$2R_{020}-A_{000}$
3	1534.08	65186	$3R_{020}-A_{020}^i$	1D	1534.63	65162	
3	1530.06	65357	$3R_{004}-A_{004}^i$	6	1532.73	65243	$3R_{020}-A_{020}^i$
3	1527.86	65451	$3R_{003}-A_{003}$	1	1528.08	65442	$3R_{004}-A_{004}$
				3	1526.38	65514	$3R_{003}-A_{003}$
10	1525.89	65536	$3R_{010}-A_{010}$				$3R_{010}-A_{010}$
30	1523.73	65628	$3R_{002}-A_{002}$	11	1524.56	65593	$3R_{002}-A_{002}$
80	1521.65	65718	$3R_{001}-A_{001}$	33	1522.76	65670	$3R_{001}-A_{001}$
2	1514.38	66034	$3R_{000}-A_{000}$	80	1521.06	65744	$3R_{000}-A_{000}$
5	1511.78	66147	$3R_{024}-A_{004}^i$	1	1513.26	66082	$3R_{024}-A_{004}^i$
7	1507.84	66320	$3R_{003}-A_{010}$	3	1511.14	66175	$3R_{020}-A_{010}$
20	1505.72	66413	$3R_{001}-A_{001}$	9	1507.38	66340	$3R_{021}-A_{001}$
5	1501.37	66606	$3R_{020}-A_{000}$	20	1505.58	66420	$3R_{020}-A_{000}$
15	1499.42	66692	$3R_{100}-A_{000}$	6	1501.72	66590	$3R_{101}-A_{001}$
0	1493.73	66947	$3R_{041}-A_{001}$	15	1500.01	66666	$3R_{100}-A_{000}$
				0	1493.03	66978	$3R_{041}-A_{001}$
1	1492.10	67020	$3R_{020}-A_{020}$				
1	1491.32	67055	$3R_{040}-A_{000}$	1	1491.35	67035	$3R_{040}-A_{000}$
							$3R_{020}-A_{020}$
2	1488.15	67198	$3R_{004}-A_{004}$	2	1489.05	67157	$3R_{004}-A_{004}$
3	1486.93	67253	$3R_{010}-A_{010}$				
			$3R_{002}-A_{002}$				
6	1486.00	67295	$3R_{002}-A_{002}$	10	1484.90	67345	$3R_{010}-A_{010}$
							$3R_{002}-A_{002}$
20	1482.88	67436	$3R_{001}-A_{001}$	20	1481.96	67478	$3R_{001}-A_{001}$
							$3R_{201}-A_{001}$
300	1480.81	67531	$3R_{000}-A_{000}$	300	1480.16	67560	$3R_{000}-A_{000}$
			$3R_{201}-A_{001}$				$3R_{200}-A_{000}$

TABLE I (Continued)

Benzene				Benzene-d ₆			
Int.	λ , Å	ν , cm ⁻¹	Transition	Int.	λ , Å	ν , cm ⁻¹	Transition
10	1479.13	67607	$3R_{000}''-A_{000}$ $3R_{100}''-A_{000}$	10	1478.87	67619	$3R_{000}''-A_{000}$
				2	1477.93	67662	$3R_{000}''-A_{000}$
60	1477.48	67683	$3R_{000}''-A_{000}$ $3R_{000}''-A_{000}$	70	1476.18	67742	$3R_{000}''-A_{000}$
0	1472.53	67910	$3R_{000}'-A_{010}$	0	1470.61	67999	$3R_{000}'-A_{001}$
2	1470.25	68016	$3R_{000}'-A_{001}$	0	1471.83	67943	$3R_{000}'-A_{010}$
				1	1469.06	68071	$3R_{000}'-A_{000}$
5	1468.28	68107	$3R_{001}'-A_{001}$	5	1467.76	68131	$3R_{001}'-A_{001}$
35	1466.00	68213	$3R_{000}'-A_{000}$	20	1466.14	68206	$3R_{000}'-A_{000}$
4	1464.51	68282	$3R_{000}''-A_{000}$ $3R_{000}''-A_{000}$	4	1465.55	68234	$3R_{000}''-A_{000}$ $3R_{000}''-A_{000}$
10	1463.01	68352	$3R_{000}''-A_{000}$	10	1462.88	68358	$3R_{000}''-A_{000}$
10	1461.98	68400	$3R_{101}'-A_{001}$				
30	1459.81	68502	$3R_{100}'-A_{000}$	20	1460.40	68474	$3R_{100}'-A_{000}$
1	1458.42	68567	$3R_{100}''-A_{000}$	1	1458.02	68586	$3R_{100}''-A_{000}$
10	1456.62	68652	$3R_{100}''-A_{000}$	10	1456.47	68659	$3R_{100}''-A_{000}$
10	1455.50	68705	$3R_{001}'-A_{001}$				
5	1453.51	68799	$3R_{000}'-A_{000}$	1	1454.49	68753	$3R_{000}'-A_{000}$
1	1449.69	68980	$4R_{010}-A_{010}$				
15	1445.57	69177	$4R_{001}-A_{001}$	7	1446.72	69122	$4R_{001}-A_{001}$
				20	1444.42	69232	$4R_{001}-A_{001}$
50	1443.72	69265	$4R_{000}-A_{000}$	60	1442.66	69316	$4R_{000}-A_{000}$ $4R_{000}-A_{000}$
8	1442.66	69316	$3R_{000}'-A_{000}$				
8	1441.33	69380	$3R_{000}'-A_{100}$				
8	1440.75	69408					
4	1439.80	69454	$3R_{100}'-A_{000}$	4	1440.91	69401	$3R_{100}'-A_{000}$
				1	1439.00	69493	$4R_{000}-A_{001}$
1	1437.99	69542	$4R_{001}-A_{000}$	0	1437.38	69571	$4R_{001}-A_{000}$
3	1432.86	69790	$3R_{000}'-A_{000}$ $4R_{010}-A_{010}$	2	1434.97	69688	$3R_{000}'-A_{000}$
				2	1432.08	69828	$4R_{000}-A_{000}$
3	1431.53	69855	$4R_{001}-A_{001}$	3	1431.07	69878	$4R_{001}-A_{001}$
6	1429.56	69952	$4R_{000}'-A_{000}$	6	1428.90	69980	$4R_{000}'-A_{000}$
18	1429.21	69969	$4R_{001}-A_{001}$	20	1428.55	70001	$4R_{001}-A_{001}$
200	1427.52	70052	$4R_{000}'-A_{000}$	300	1426.98	70078	$4R_{000}'-A_{000}$
30	1426.66	70094	$4R_{000}'-A_{000}$	30	1425.90	70131	$4R_{000}'-A_{000}$ $4R_{101}-A_{001}$
20	1424.94	70178	$4R_{000}'-A_{000}$ $4R_{101}-A_{001}$ $4R_{100}-A_{000}$	20	1424.43	70204	$4R_{000}'-A_{000}$ $4R_{100}-A_{000}$
2	1423.89	70230	$4R_{001}-A_{001}$	3	1417.73	70535	$4R_{001}-A_{001}$
2	1417.22	70561	$4R_{000}'-A_{000}$	5	1415.92	70625	$4R_{000}'-A_{000}$
3	1415.99	70622	$4R_{001}-A_{001}$				
25	1413.84	70729	$4R_{000}'-A_{000}$	20	1414.21	70711	$4R_{000}'-A_{000}$

TABLE I (Continued)

Benzene				Benzene-d ₆			
Int.	λ , Å	ν , cm ⁻¹	Transition	Int.	λ , Å	ν , cm ⁻¹	Transition
15	1412.98	70772	$4R_{020}^{\prime\prime}-A_{000}$	10	1413.19	70762	$4R_{020}^{\prime\prime}-A_{000}$
8	1411.51	70846	$4R_{020}^{\prime\prime\prime}-A_{000}$	2	1411.81	70831	$4R_{020}^{\prime\prime\prime}-A_{000}$
				12	1409.39	70953	$5R_{022}^{\prime\prime}-A_{002}$
5	1409.82	70931	$5R_{001}^{\prime}-A_{001}$	30	1408.38	71004	$4R_{101}^{\prime}-A_{001}$
40	1408.10	71018	$5R_{000}^{\prime}-A_{000}$	40	1407.48	71050	$5R_{001}^{\prime}-A_{001}$
			$4R_{100}^{\prime}-A_{000}$				$4R_{100}^{\prime}-A_{000}$
20	1407.28	71059	$4R_{100}^{\prime\prime}-A_{000}$				$5R_{000}^{\prime}-A_{000}$
			$5R_{010}^{\prime}-A_{010}$				$4R_{100}^{\prime\prime}-A_{000}$
18	1405.61	71143	$4R_{100}^{\prime\prime\prime}-A_{000}$	16	1406.03	71122	$4R_{100}^{\prime\prime\prime}-A_{000}$
2	1404.42	71204	$4R_{000}^{\prime}-A_{000}^*$	1	1404.48	71201	$4R_{000}^{\prime}-A_{000}^*$
							$5R_{010}^{\prime}-A_{010}$
30	1402.02	71326	$5R_{001}^{\prime}-A_{001}$	20	1400.87	71384	$5R_{001}^{\prime}-A_{001}$
100	1400.20	71418	$5R_{000}^{\prime}-A_{000}$	100	1399.50	71454	$5R_{000}^{\prime}-A_{000}$
60	1399.38	71460	$5R_{000}^{\prime\prime}-A_{000}$	60	1398.84	71488	$5R_{000}^{\prime\prime}-A_{000}$
15	1398.34	71513	$5R_{000}^{\prime\prime\prime}-A_{000}$	15	1397.80	71541	$5R_{000}^{\prime\prime\prime}-A_{000}$
10	1396.27	71619	$5R_{021}^{\prime}-A_{001}$	10	1396.17	71624	$5R_{021}^{\prime}-A_{001}$
15	1394.86	71692	$5R_{020}^{\prime}-A_{000}$	15	1394.75	71697	$5R_{020}^{\prime}-A_{000}$
20	1392.50	71813	$4R_{000}^{\prime}-A_{000}$	18	1393.08	71783	$4R_{000}^{\prime}-A_{000}$
			$5R_{101}^{\prime}-A_{001}$	10	1391.36	71872	$5R_{101}^{\prime}-A_{001}$
				20	1390.02	71941	$5R_{100}^{\prime}-A_{000}^*$
35	1388.59	72015	$6R_{000}^{\prime}-A_{000}$	25	1388.73	72008	$5R_{100}^{\prime}-A_{000}$
			$5R_{021}^{\prime}-A_{001}$				$5R_{021}^{\prime}-A_{001}$
15	1389.13	71987	$5R_{100}^{\prime}-A_{000}$	30	1387.82	72055	$6R_{000}^{\prime}-A_{000}$
30	1387.07	72094	$5R_{020}^{\prime}-A_{000}^*$	30	1387.05	72095	$5R_{020}^{\prime}-A_{000}$
25	1386.31	72134	$5R_{020}^{\prime\prime}-A_{000}$				
0	1385.67	72167	$5R_{021}^{\prime\prime}-A_{001}^*$	50	1386.44	72127	$5R_{020}^{\prime\prime}-A_{000}$
				1	1385.50	72176	$5R_{020}^{\prime\prime\prime}-A_{000}$
10	1385.35	72184	$5R_{020}^{\prime\prime\prime}-A_{000}$	20	1384.89	72208	$6R_{001}^{\prime}-A_{001}$
			$6R_{001}^{\prime}-A_{001}$				
100	1384.17	72245	$6R_{000}^{\prime}-A_{000}$	100	1383.48	72281	$6R_{000}^{\prime}-A_{000}$
95	1383.48	72281	$6R_{000}^{\prime\prime}-A_{000}$	95	1382.90	72312	$6R_{000}^{\prime\prime}-A_{000}$
30	1382.67	72324	$6R_{000}^{\prime\prime\prime}-A_{000}$	30	1381.91	72364	$6R_{000}^{\prime\prime\prime}-A_{000}$
							$5R_{100}^{\prime}-A_{000}$
				10	1380.84	72420	$5R_{100}^{\prime\prime}-A_{000}$
10	1381.62	72379	$5R_{100}^{\prime}-A_{000}$				
10	1380.77	72423	$5R_{100}^{\prime\prime}-A_{000}$				
6	1379.69	72480	$5R_{000}^{\prime}-A_{000}$	4	1379.78	72475	$5R_{100}^{\prime\prime\prime}-A_{000}$
15	1375.70	72690	$7R_{000}^{\prime}-A_{000}$	20	1375.80	72685	$7R_{000}^{\prime}-A_{000}$
50	1373.61	72801	$7R_{000}^{\prime\prime}-A_{000}$	60	1373.02	72832	$7R_{000}^{\prime\prime}-A_{000}$
60	1373.27	72819	$7R_{000}^{\prime\prime\prime}-A_{000}$	60	1372.62	72853	$7R_{000}^{\prime\prime\prime}-A_{000}$
							$6R_{021}^{\prime}-A_{001}$
15	1372.72	72848	$7R_{000}^{\prime\prime\prime}-A_{000}$	15	1372.00	72886	$7R_{000}^{\prime\prime\prime}-A_{000}$
15	1372.50	72860	$6R_{021}^{\prime}-A_{001}$				

TABLE I (Concluded)

Benzene				Benzene- <i>d</i> ₆			
Int.	λ , Å	ν , cm ⁻¹	Transition	Int.	λ , Å	ν , cm ⁻¹	Transition
18	1371.34	72921	$6R'_{020}-A_{000}$	12	1371.32	72922	$6R'_{020}-A_{000}$
20	1370.64	72959	$6R'_{020}-A_{100}$	15	1370.71	72955	$6R'_{020}-A_{000}$
20	1368.66	73064	$6R'_{100}-A_{000}$	10	1369.76	73005	$8R'_{001}-A_{001}$
20	1368.48	73074	$8R'_{000}-A_{000}$	20	1367.61	73120	$8R'_{000}-A_{000}$
10	1367.59	73121	$8R'_{001}-A_{001}$				
60	1366.31	73190	$8R'_{100}-A_{000}$	60	1365.98	73208	$8R'_{000}-A_{000}$
			$8R'_{100}-A_{000}$				$6R'_{100}-A_{000}$
40	1365.75	73220	$8R''_{000}-A_{000}$	40	1365.41	73238	$8R''_{000}-A_{000}$
			$6R'_{100}-A_{000}$				
			$8R'_{000}-A_{100}$				
15	1365.16	73251	$6R''_{100}-A_{000}$	40	1365.18	73250	$6R''_{100}-A_{000}$
							$8R'_{000}-A_{000}$
15	1364.38	73293	$6R'''_{100}-A_{000}$	15	1364.29	73298	$6R'''_{100}-A_{000}$
20D	1363.20	73357	$9R'_{001}-A_{001}$	20	1362.45	73397	$9R'_{001}-A_{001}$
			$9R'_{000}-A_{000}$				$9R'_{000}-A_{000}$
60	1361.48	73449	$9R'_{000}-A_{000}$	50	1360.84	73484	$9R'_{000}-A_{000}$
			$7R'_{020}-A_{000}$	60	1361.29	73460	$7R'_{020}-A_{000}$
40	1357.69	73655	$10R'_{000}-A_{000}$	40	1357.07	73688	$10R'_{000}-A_{000}$
200	1353.43	73886		200	1348.55	74154	
100	1348.64	74149		100	1343.8	74416	
150	1342.5	74490		150	1338.28	74723	
150	1341.5	74544		150	1335.41	74883	

^aCalculated position—59692 cm⁻¹; assumes regularity of ν_{18} progression.

^bCalculated position—61246 cm⁻¹; assumes regularity of ν_{18} progression.

^cIdentification probably correct. But $\Delta G_{1/2} = 967$ cm⁻¹, which is about 50 cm⁻¹ too high.

^dThe $4R_{002}-A_{002}$ band is probably present but is overlapped with an impurity band in the light source.

^eIdentification uncertain.

^fBand identification uncertain since transition is forbidden.

^g $4R_{010}-A_{010}$ possibly present but is overlapped with impurity band in the light source.

^h $3R_{002}-A_{002}$ band present but could not be measured accurately.

ⁱBroad vibrational bands of the $V-N$ ($^1E_{1u}-A_{1g}$) transition.

^jIdentification uncertain from intensity considerations.

$R'-A$, $R''-A$, $R'''-A$, where relative term values increase in that order, i.e., $R < R' < R'' < R'''$. R is used as a general symbol for a Rydberg state and each series will be discussed in detail in Section V. The electronic ground state has symmetry A_{1g} , abbreviated here as A , and all states under discussion shall be understood as being singlet states. The different Rydberg states of a given series are designated $2R$, $3R$, $4R$, etc. where the number preceding the R is the whole number in the denominator of the Rydberg series term expression (Section VI). Since this denominator can be expressed as either $n+a$ or $m-b$, where $n = m-1 = 2, 3, \dots$ and $a = 1-b$ (the "quantum defect"), n may not actually be the principal quantum number but for purposes of identification it will be so considered (Nelson and Simpson 1955).

In general the vibrational structure will be designated as $R_{v_1 v_2 v_3 \dots}$ where v_1, v_2, v_3 , etc. are vibrational quantum numbers of the various normal vibrations listed in order numerically according to the usual ground state notation (Herzberg 1945). In the present work only the C-C "breathing" vibration

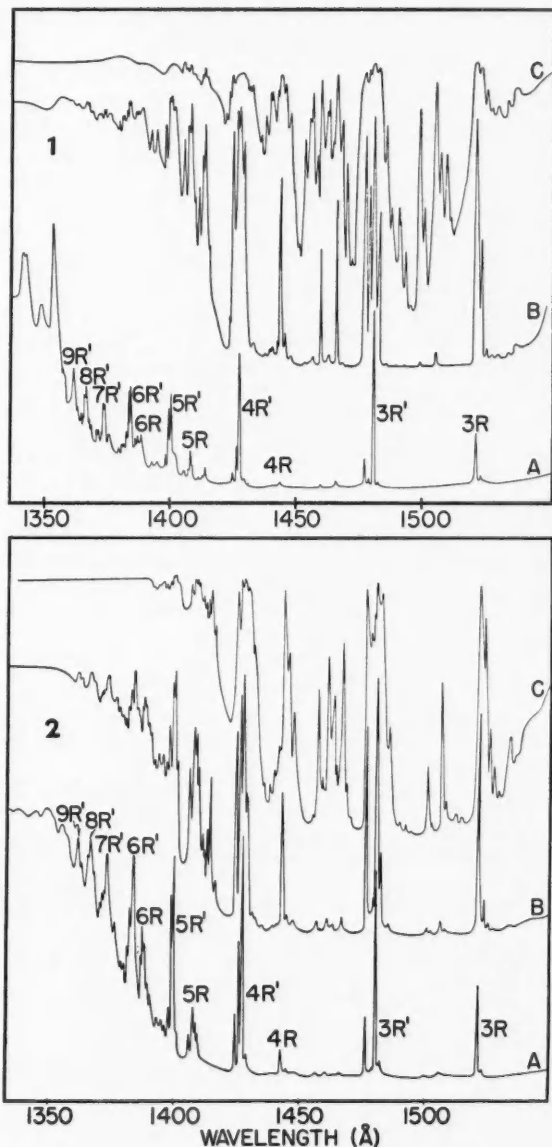


FIG. 1. Microphotometer tracings of the absorption spectra of benzene, 1330-1550Å. Cell path—17 cm. (A) pressure ~ 0.5 mm.; (B) pressure ~ 1 mm.; (C) pressure ~ 3 mm.

FIG. 2. Microphotometer tracings of the absorption spectra of benzene-d₆, 1330-1550Å. Cell path—17 cm. (A) pressure ~ 0.5 mm.; (B) pressure ~ 1 mm.; (C) pressure $\sim 2\frac{1}{2}$ mm.

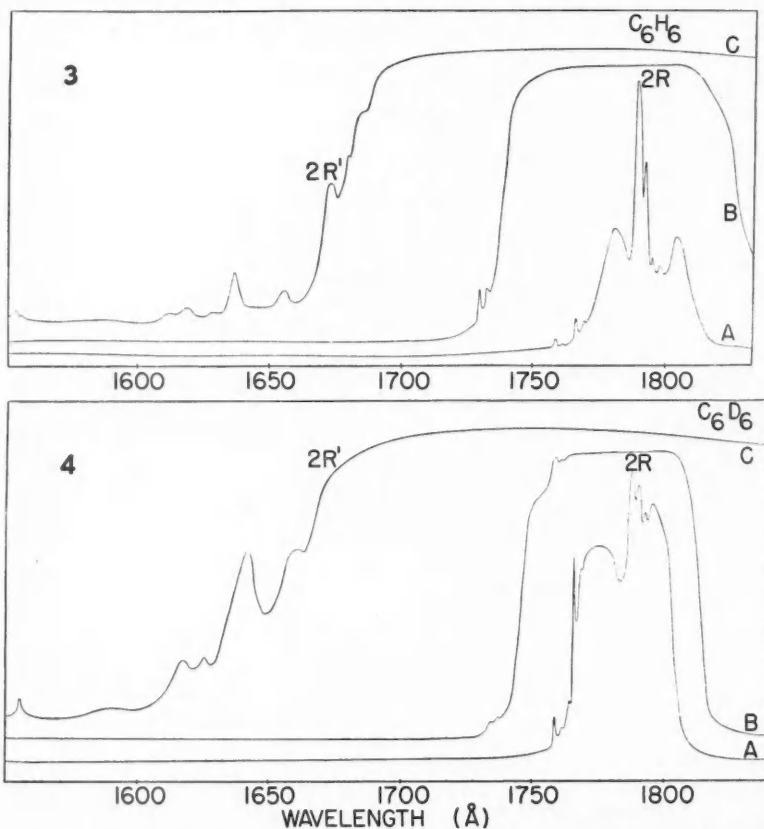


FIG. 3. Microphotometer tracings of the absorption spectra of benzene, 1550–1850Å. Cell path—17 cm. (A) pressure ~ 0.2 mm.; (B) pressure ~ 0.5 mm.; (C) pressure ~ 2 mm.

FIG. 4. Microphotometer tracings of the absorption spectra of benzene- d_6 , 1550–1850Å. Cell path—17 cm. (A) pressure ~ 0.2 mm.; (B) pressure ~ 0.5 mm.; (C) pressure ~ 2 mm.

(ν_2), the ring distortion vibration (ν_{18}), and the out-of-plane bending vibration (ν_{20}) may be identified in the Rydberg transitions (Section V). For example, the designation $2R_{mnp}$ is used for the vibrational level $v_2 = m$, $v_{18} = n$, and $v_{20} = p$, $v_1 = v_3 = v_4 \dots = v_{17} = v_{19} = 0$, for the lowest lying observed electronically excited Rydberg state, $2R$. Thus the transition $2R_{021}-A_{001}$ represents two quanta of ν_{18} , one quantum of ν_{20} in the upper state combining with one quantum of ν_{20} in the ground state, and might be termed an electronic combination band.

In Table I the bands are identified using the above notation and this is given in columns 4 and 8 for benzene and benzene- d_6 , respectively. Only a few bands remain unidentified; a considerable number are superposed giving rise to some

uncertainty in the corresponding frequency differences. The relative intensities, which are only approximate estimates based on photographic densities, are given in columns 1 and 5. The measured wavelengths and frequencies are shown in columns 2 and 3, 6 and 7, for benzene and benzene- d_6 , respectively. In Figs. 1-4 only the vibrationless transitions $nR_{000}-A_{000}$ and $nR'_{000}-A_{000}$ are indicated and are abbreviated nR and nR' .

V. VIBRATIONAL ANALYSIS

A. Identification of Vibrations

As may be seen in Figs. 1-4, the absorption spectrum of benzene below 1850 Å consists of a series of main groups, each possessing nearly identical structure and converging to the ionization limit. The groups can be divided into two types: one fairly simple (Fig. 5) and one somewhat more complicated (Fig. 8). These two examples at 1521 Å and 1481 Å represent the second members ($n = 3$) of the two previously identified Rydberg series (Price and Wood 1935).

The series with the simpler structure (nR) lies lowest in energy and each member readily submits to a vibrational analysis. The vibrationless transition, $3R_{000}-A_{000}$ at 65718 cm^{-1} (Fig. 5A, benzene), is identified without question since it is the strongest band in the system, shows an isotope shift to the violet of 26 cm^{-1} on complete deuterium substitution, and possesses a series of satellite bands to the red which look much like bands originating from thermally excited vibrational states, i.e., "hot bands". Further inspection reveals two

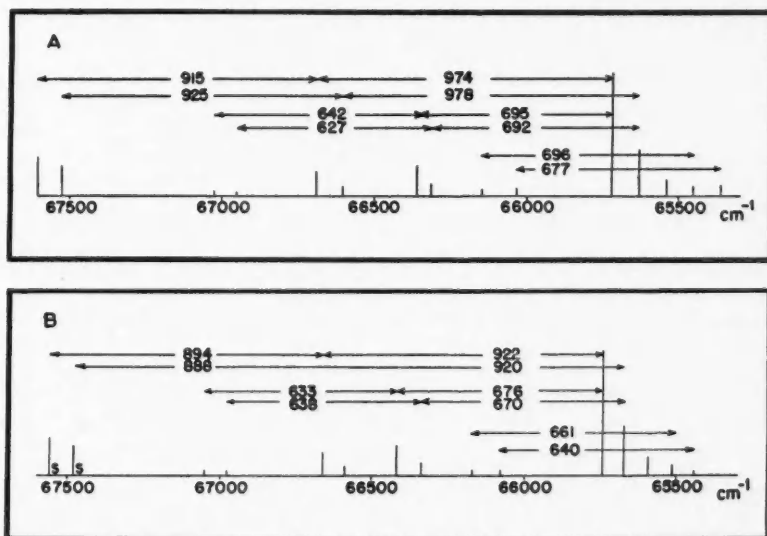


Fig. 5. Main bands of the 1521 Å $3R-A$ transition in benzene (A) and in benzene- d_6 (B). S indicates superposed bands.

successive spacings to higher frequencies from the system origin of 974 and 915 cm^{-1} ; the analogous spacings in benzene- d_6 are 922 and 894 cm^{-1} . These occur with moderate intensity and are reasonably interpreted as progressions of the totally symmetric "breathing vibration" (ν_2) in the upper state and were predicted by theory (Section III). The isotope ratio $974/922 = 1.056$ is quite close to the ground state ratio $992/945 = 1.050$ and that found in the near ultraviolet bands (${}^1B_{2u} \rightarrow {}^1A_{1g}$) $923/879 = 1.050$ (Nordheim *et al.* 1940), and is predicted approximately from simple theory assuming an harmonic oscillator ($((14/13)^{1/2} = 1.038)$). The other spacing readily identifiable is a strongly anharmonic progression beginning with 695 cm^{-1} in benzene (675 cm^{-1} in benzene- d_6) and extending to three (or perhaps four) series members with strong intensity. The weak red bands adjoining the system origin have an average spacing of 90 cm^{-1} in benzene and 75 cm^{-1} in benzene- d_6 .

From the general predictions previously made (Section III) and the intensity distribution in these hot bands, one can only conclude that they must be $v-v$ type transitions of the non-totally symmetric ν_{20} vibration (404 cm^{-1} in benzene and 337 cm^{-1} in benzene- d_6 , ground state); the upper state frequencies may then be calculated as 314 and 262 cm^{-1} , respectively, for the two molecules.

The only other totally symmetric vibration is the C-H stretching vibration, ν_1 , with a ground state value of 3062 cm^{-1} . It is clearly not present in any of the Rydberg transitions, and the 695 cm^{-1} spacing must represent two quanta of some low frequency which has a low value in the ground state. The magnitude and isotopic frequency ratio (1.030) eliminate all other low frequencies from consideration and suggest that the 695 cm^{-1} spacing is two quanta of ν_{18} , which has a ground state value of 606 cm^{-1} (isotopic frequency ratio = 1.052). This is strongly supported by the clear identification of the $3R_{030} \rightarrow A_{010}$ transition in both molecules. However, the identification of ν_{18} should be reconsidered in view of the Jahn-Teller theorem (see Section B). The normal vibrations, ν_2 , ν_{18} , and ν_{20} , in point group D_{6h} are illustrated in Fig. 6.

Clearly, isotope frequency ratios in the excited states may not be necessarily

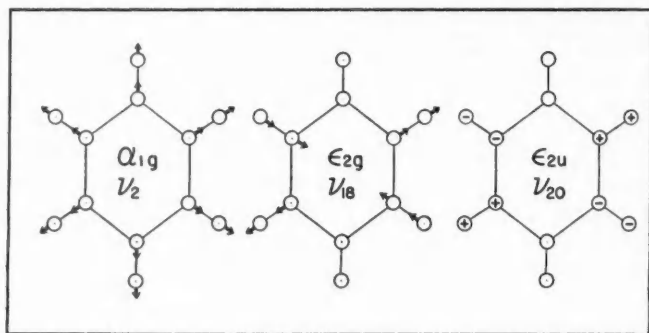


FIG. 6. Normal vibrations excited in the Rydberg bands of benzene. The symmetry symbols should be lower case letters instead of Greek letters.

the same as in the ground state. Where a large number of vibrations are observed as in the ground state (from infrared and Raman data), the so-called Teller-Redlich product rule (Herzberg 1945) may be applied to determine the correctness of assignments. Briefly, this rule states that the ratio of the products in two isotopic molecules of the frequencies of all vibrations of a given symmetry species is a constant depending only on the nuclear masses and the molecular geometry. This rule cannot, in general, be applied to an excited electronic state where, usually, only a few vibrations are excited. However, if a given vibration is identified without unusual anharmonicity, and the molecule retains a geometry very similar to the ground state, the isotope ratio in the excited state should not differ greatly from that in the ground state. This is certainly true in the B_{2u} state and should be approximately true in the Rydberg states although in the latter the magnitude of ν_{18} (350 cm^{-1}) is considerably smaller than the ground state value (606 cm^{-1}).

One might expect to find a few $v-v$ type bands involving the 606 cm^{-1} ν_{18} vibration. The first such hot band ($3R_{020}-A_{020}$) can be found in both molecules (65186 cm^{-1} in benzene; 65243 cm^{-1} in benzene- d_6).³ Since the ν_2 vibration is the only totally symmetric one identified, one might have expected such a progression to be the strongest one in the band system; actually, the first member of the ν_{18} progression is somewhat stronger although theory would predict this type of transition to be quite weak. Also identified in the system (Fig. 5A and 5B) are weak combination bands of the type $2\nu_{18} + \nu_{20}$ and $\nu_2 + \nu_{20}$. Such bands are identified in Table I as $3R_{021}-A_{001}$, $3R_{101}-A_{001}$, etc. The energy level diagram for the $3R-A$ transition is shown in Fig. 7. Here the spacings are drawn to scale except for the electronic energy which is con-

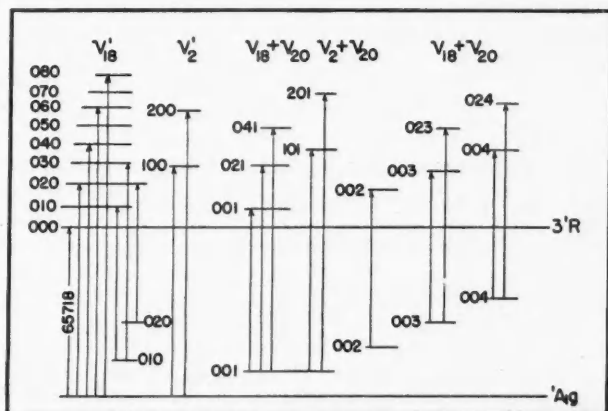


FIG. 7. Energy level diagram showing observed transitions in the 1521 Å $3R-A$ band of benzene.

³The identification of $3R_{020}-A_{020}$ must be considered somewhat uncertain from intensity considerations. The transition $3R_{010}-A_{010}$ would occur 258 cm^{-1} (benzene) and 239 cm^{-1} (benzene- d_6) to the red of the system origin and is obscured by the $3R_{001}-A_{001}$ bands.

siderably reduced. All observed transitions are included (some involve superposed bands). It may be seen that no ν_{18} vibrations combine with the upper state level, 002; there is no apparent reason for this as $3R_{023}-A_{003}$ and $3R_{034}-A_{004}$ are observed.

The 1481\AA band ($3R'-A$) is a typical system of the more complicated Rydberg series and is drawn schematically in Fig. 8A (benzene) and Fig. 8B

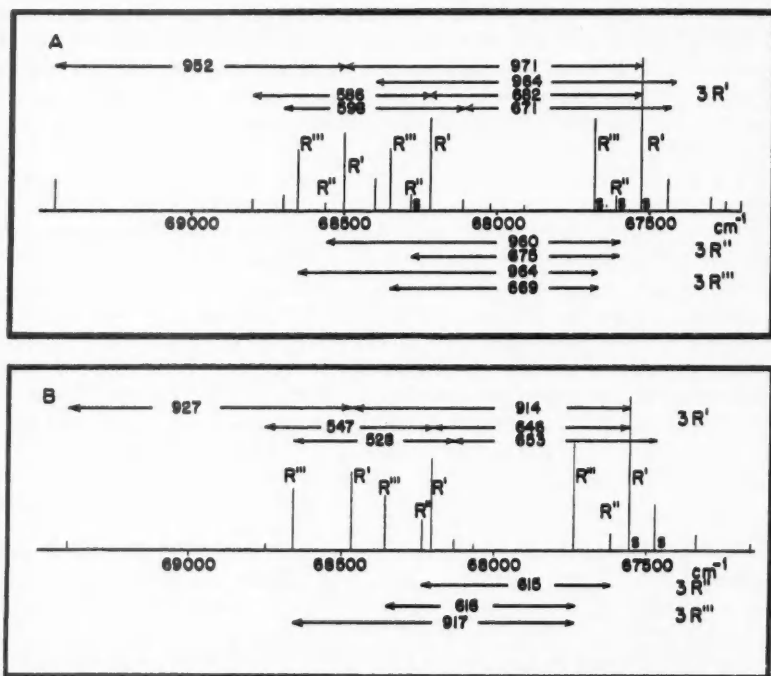


FIG. 8. Main bands of the 1481\AA $3R'-A$, $3R''-A$, $3R'''-A$ transitions in benzene (A) and in benzene- d_6 (B). S indicates superposed bands. A possible perturbation in the $3R'_{100}-A_{000}$ transition in benzene- d_6 makes its assignment doubtful and it is omitted from the figure.

(benzene- d_6). The characteristic feature of this system is the subgrouping consisting of a very strong transition (labelled $3R'$), a weak band ($3R''$), and a moderately strong band ($3R'''$). This grouping is repeated two more times in the same band system. The spacing in the subgrouping is too small to be considered as a new vibrational progression and the intensity of at least R''' is such that further members would be required. Furthermore, deuterium substitution discourages this interpretation as no reduction in spacing is observed. Price and Wood (1935) cautiously suggested that this peculiar substructure was due to some multiplicity of the electronic states. From intensity considerations it seems obvious that this cannot be spin multiplicity, but

some other type of electronic splitting is reasonable. In Fig. 8 the totally symmetric ν_2 vibration and two quanta of the non-totally symmetric ν_{18} vibration are readily identified, as in the $3R-A$ transition, from their magnitude and isotope effect. Again the clear identification of the $3R_{080}-A_{010}$ transition in both molecules supports the ν_{18} interpretation. Furthermore, at least one hot band of the $v-v$ type due to the ν_{20} vibration may be observed⁴ as well as combination bands of the type $\nu_{20}+\nu_2$, $\nu_{20}+2\nu_{18}$. The vibrational structure of R'' and R''' reveals spacings of 960 and 969 cm^{-1} and 675 and 669 cm^{-1} , which are ν_2 and $2\nu_{18}$, respectively. The same structure as observed in the 1481 Å system is repeated in the other Rydberg members of the series except for minor variations.

As the principal quantum number, n , increases, the relative intensity of R'' increases and R''' decreases and the spacing between them also decreases, finally becoming nearly zero at $n = 8$. This observation suggests that these are three quite different electronic states but arising from the same electronic configuration.

B. The Jahn-Teller Effect

It has been suggested (Nordheim *et al.* 1940) that the most satisfactory theoretical interpretation of the benzene Rydberg transitions is that some of them represent ${}^1E_{1u}-{}^1A_{1g}$ and others are ${}^1A_{2u}-{}^1A_{1g}$. According to the Jahn-Teller theorem (Jahn and Teller 1937; Mulliken 1939; Spomer and Teller 1941), the stable equilibrium configuration of a degenerate state in a non-linear molecule is not the symmetrical one. Accordingly, a degenerate state would be expected to split into two non-degenerate states and produce a more complicated spectrum. If the expected magnitude of the Jahn-Teller splitting could be calculated, even approximately, one might reasonably assign the observed members to these transitions. However, Jahn-Teller components would be expected to have equal intensities and this is not observed for any pair of the Rydberg transitions in all of the members.

No experimental Jahn-Teller splitting has ever been observed and it is difficult to calculate how much splitting would be expected in any given molecule. It is conceivable that if the nuclear positions were displaced only a small amount from the symmetrical configuration, no splitting would result. The potential curves corresponding to each Jahn-Teller component would be displaced in the direction of some normal coordinate but the vibronic levels would lie at equal energies, and, therefore, remain degenerate. However, there may be an effect on the intensities of some of the vibrational progressions. In the benzene Rydberg states, the degeneracy may be removed by a nuclear displacement of e_{2g} symmetry (Jahn and Teller 1937), resulting in a stable equilibrium configuration which is not quite a symmetrical hexagon (Nordheim *et al.* 1940). Such a nuclear displacement, however slight, might be expected to enhance vibrations of symmetry e_{2g} . The anomalously high intensities noted in transitions involving the non-totally symmetric ν_{18} (e_{2g}) vibra-

⁴Hot band identification is difficult in this region owing to the more complicated substructure and consequent overlapping.

tion may be explained in just this way. This is supported by the clear identification of at least three members of the ν_{18} progression in at least three systems ($3R-A$, $4R-A$, $3R'-A$, Table I). The usual intensity rule (equation 1) would not permit observation of such a long progression.⁵ Since these high intensities are found in all the Rydberg transitions, it is concluded that all the observed excited states have been distorted into a nuclear configuration of D_{2h} symmetry. It must be admitted, however, that this explanation may be extremely oversimplified and a detailed theoretical treatment should be applied in an effort to determine the following: (1) the stable nuclear configurations resulting from a Jahn-Teller displacement; (2) the vibration of the e_{2g} species which is most likely to be observed; (3) its approximate magnitude; and (4) selection rules governing its appearance.

The transition moment of the ${}^1E_{1u} \leftarrow {}^1A_{1g}$ transition is polarized parallel to the ring (xy polarized) and that of the ${}^1A_{2u} \leftarrow {}^1A_{1g}$ transition is polarized in a perpendicular direction (z polarized). Recent measurements of extinction coefficients of hexamethylbenzene (absorption spectrum analogous to benzene) using polarized light suggest that the benzene absorption spectrum in the 1800 Å region should consist of two transitions, one xy polarized and one z polarized (Nelson and Simpson 1955). Since there is strong theoretical evidence for assigning the $V-N$ background at 1790 Å (Figs. 3 and 4) to ${}^1E_{1u} \leftarrow {}^1A_{1g}$ (Mulliken 1939; Roothaan and Mulliken 1948), the identified $2R-A$ transition, which lies at the same energy, should be z polarized and therefore assigned to ${}^1A_{2u} \leftarrow {}^1A_{1g}$. This means that all members of the $nR-A$ series should also be so assigned, at least formally.⁶

C. Vibrational Constants

In Table II are given the vibrational constants of the ground state (Herzberg 1945) and all the observed Rydberg states of benzene and benzene- d_6 as well as the band origins, the electronic isotope shift, and the isotope frequency ratios. In most cases it is useful to give only the first vibrational quantum, $\Delta G_{\frac{1}{2}}$ (and not ω^0), as frequently only two members of each progression are identified with certainty. The $\Delta G_{\frac{1}{2}}$ values were derived from Table I; in general, ν_2 shows only a small anharmonicity and ν_{18} shows a larger effect. In principle a polyatomic molecule may dissociate in much the same manner as a diatomic molecule; a vibration like the ν_2 C-C vibration in benzene is excited to higher and higher vibrational states until dissociation occurs. However, since in benzene all C-C bonds are equivalent, such a dissociation

⁵In a private communication, Dr. L. E. Orgel of Cambridge University, England, disclosed that he had independently arrived at this same interpretation from studying the present data.

⁶In a further communication, Dr. Orgel emphasized that while the formal assignment of the nR' , nR'' , $nR'''-A$ series is not yet clear, nevertheless, it appears that $nR'-A$ might be correlated reasonably with a strong allowed transition and $nR''-A$ and $nR'''-A$ might be group theoretically forbidden but become relatively strong by "borrowing" intensity from the allowed transition. It is to be noted that the Jahn-Teller effect is assumed to be important even though the excited state may be formally non-degenerate. This is reasonable if the excited electron is weakly bonding and the Rydberg states are very much like the ground state of the molecular ion (${}^2E_{1g}$). If this is not true, then either the $V-N$ background continuum is ${}^1A_{2u} \leftarrow {}^1A_{1g}$ or the $2R-N$ and the $V-N$ transitions are both ${}^1E_{1u} \leftarrow {}^1A_{1g}$, and, for some reason not now understood, no electronic perturbation (mixing) takes place.

TABLE II

VIBRATIONAL CONSTANTS AND BAND SYSTEM ORIGINS FOR THE RYDBERG STATES OF BENZENE AND BENZENE- d_6

Electronic state	Benzene			Band system origin, $\Delta G_{\frac{1}{2}}$ cm ⁻¹	Benzene- d_6			Band system origin	Isotope shift, cm ⁻¹	Isotope ratio ν_2	Isotope ratio ν_{18}	Isotope ratio ν_{20}
	ν_2 $\Delta G_{\frac{1}{2}}$ cm ⁻¹	ν_{18} $\Delta G_{\frac{1}{2}}$ cm ⁻¹	ν_{20} $\Delta G_{\frac{1}{2}}$ cm ⁻¹		ν_2 $\Delta G_{\frac{1}{2}}$ cm ⁻¹	ν_{18} $\Delta G_{\frac{1}{2}}$ cm ⁻¹	ν_{20} $\Delta G_{\frac{1}{2}}$ cm ⁻¹					
A_{1g}	992 ^b	606 ^b	404 ^b	0	945 ^b	577 ^b	337 ^b	0	0	1.050	1.050	1.20
$2R$	974	361	316	55881	922	345	256	55946	65	1.056	1.046	1.23
$2R'$	—	372	—	59795	—	323	—	59692 ⁱ	—	—	1.15	—
$2R''$	—	337	—	61421	—	—	—	61246 ⁱ	—	—	—	—
$2R'''$	—	338	334	64387	—	314	269	64362	—	—	1.076	1.24
$3R$	974	348 ^c	314	65718	922	338 ^d	262	65744	26	1.056	1.030	1.20
$3R'$	971	341 ^e	309	67531	914	323 ^f	255	67560	29	1.062	1.056	1.21
$3R''$	960	338	—	67607	967 ^a	308	—	67619	12	—	1.097	—
$3R'''$	969	335	—	67683	917	308	—	67742	59	1.057	1.088	—
$4R$	965	344 ^d	302	69265	888 ^g	332 ^h	251	69316	51	—	1.036	1.20
$4R'$	966	338	321	70052	926	316	260	70078	26	1.043	1.070	1.23
$4R''$	965	339	—	70094	919	316	—	70131	37	1.050	1.073	—
$4R'''$	965	334	—	70178	918	314	—	70204	26	1.051	1.064	—
$5R$	969	337	317	71018	892 ⁱ	323	289	71050	32	—	1.043	1.10
$5R'$	961	338	312	71418	910	320	267	71454	36	1.056	1.056	1.17
$5R''$	963	337	—	71460	932	320	—	71488	28	1.033	1.053	—
$5R'''$	967	336	—	71513	934	318	—	71541	28	1.035	1.057	—
$6R$	972	—	—	72015	—	—	—	72055	40	—	—	—
$6R'$	975	338	343	72245	927	322	264	72281	36	1.052	1.050	1.30
$6R''$	970	339	—	72281	938	322	—	72312	31	1.034	1.053	—
$6R'''$	969	—	—	72324	934	—	—	72364	40	1.037	—	—

Electronic state	Benzene		Isotope shift, cm ⁻¹	Isotope ratio
	ν_{18} $\Delta G_{\frac{1}{2}}$ cm ⁻¹	Band system origin		
$7R$	—	72690	—	—
$7R'$	324	72801	31	1.01
$7R''$	—	72819	34	—
$7R'''$	—	72848	38	—
$8R$	—	73066	54	—
$8R'$	—	73190	18	—
$8R''$	—	73220	18	—
$8R'''$	—	73220	30	—
$9R$	—	73357	40	—
$9R'$	—	73449	35	—
$10R'$	—	73655	33	—

^aIdentification uncertain due to abnormal $\Delta G_{\frac{1}{2}}$.^bHerzberg, G. 1945. Infrared and Raman spectra. D. Van Nostrand Co., New York.^c $\omega_{18}^0 = 360.2$; $x_{18}^0 = -4.23$ cm⁻¹.^d $\omega_{18}^0 = 349.1$ cm⁻¹; $x_{18}^0 = -4.07$ cm⁻¹.^e $\omega_{18}^0 = 377.2$ cm⁻¹; $x_{18}^0 = -12.16$ cm⁻¹.^f $\omega_{18}^0 = 357.8$ cm⁻¹; $x_{18}^0 = -11.84$ cm⁻¹.^g $\omega_{18}^0 = 351.5$ cm⁻¹; $x_{18}^0 = -2.5$ cm⁻¹.^h $\omega_{18}^0 = 339.3$ cm⁻¹; $x_{18}^0 = -2.3$ cm⁻¹.ⁱBand not observed. Figure given is an estimated position.^j ΔG uncertain due to overlapping bands.

must break all C-C bonds, and would require six times the energy to break a single bond. The result is that the observed upper state levels of ν_2 are so far

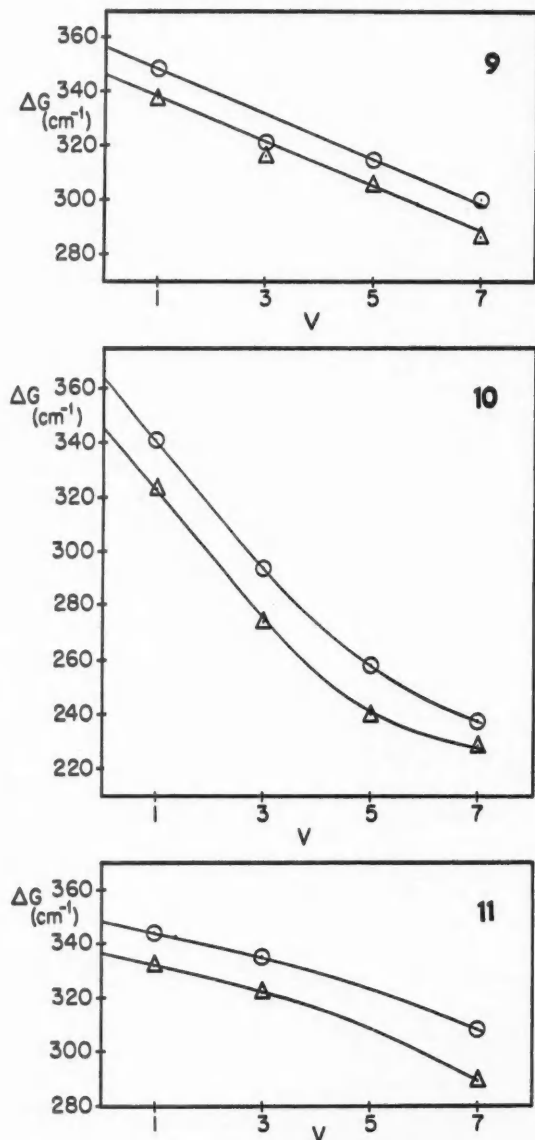


FIG. 9. ΔG versus ν plot for the ν_{18} progression in the 3R state of benzene (circles) and benzene- d_6 (triangles).

FIG. 10. ΔG versus ν plot for the ν_{18} progression in the 3R' state of benzene (circles) and benzene- d_6 (triangles).

FIG. 11. ΔG versus ν plot for the ν_{18} progression in the 4R state of benzene (circles) and benzene- d_6 (triangles).

from the dissociation limit that ν_2 is almost completely harmonic. If strong anharmonic behavior is observed, a perturbation process is almost certain to be responsible.

In a few cases, up to four members of the ν_{18} progression may be identified ($3R'$, $3R$, $4R$), although not without some overlapping with other bands, and determinations of approximate values of ω_{18}^0 and x_{18}^0 are possible (see footnotes to Table II). ΔG_v versus v plots in these states are shown in Figs. 9, 10, and 11. Only the $3R$ state shows a straight line relationship; in the other states some curvature is found for higher v' values; this may not be a real effect.

As may be seen from columns 11, 12, and 13 (Table II), the isotopic frequency ratios in the excited states are very nearly equal to the ground state values, 1.050, 1.050, and 1.20, for the ν_2 , ν_{18} , and ν_{20} vibrations respectively. The average values of these ratios for the excited states are 1.047, 1.058, and 1.205. The magnitudes of these frequencies do not change much as the ionization limit is approached; this is in accordance with the usual views that the electron excited to Rydberg orbitals is a weakly-bonding π electron.

VI. RYDBERG SERIES AND IONIZATION POTENTIALS

The location of the band system origin ("vibrationless transition") of each Rydberg transition was usually made without ambiguity from consideration of the following information: (1) this transition is expected to be the strongest in the system; (2) isotope shift on deuteration should be 25–40 cm^{-1} (towards higher frequencies)⁷; and (3) observation of expected vibrational transitions combining with each system origin. The first condition is true in every case except the benzene- d_6 $2R'-A$ and $2R''-A$ transitions; the second was usually true but some rather large deviations were noted namely in the $2R-A$, $2R'-A$, and $7R-A$ systems (see Table II); for the third condition, reasonable vibrational progressions were observed for all systems except those near the ionization limit.

Price and Wood (1935) were able to fit their data to the usual Rydberg equation:

$$(2) \quad \nu = I - R/(n+a)^2,$$

where ν is the observed system origin, I is the ionization potential, R is the Rydberg constant for infinite mass (109737 cm^{-1}), n is the "principal quantum number", and a is the "quantum defect". They obtained for the $nR-A$ series, $I = 74590 \text{ cm}^{-1}$ with $a = 0.55$ and for $nR'-A$, $I = 74495 \text{ cm}^{-1}$ with $a = 0.97$. In the present experiments, four series are identified and a few more members in each series closer to the ionization limit were observed. By the use of a Rydberg term table (Paschen 1928), the data were fitted to an equation of the form of (2) such that: (1) the "quantum defect", a , approaches a constant value for the higher members and is the same function of n for both molecules; and (2) all series extrapolate to the same ionization potential. This procedure is necessary since the lower members would be expected to deviate appreciably

⁷A shift in this range is observed in most of those transitions which permit a clear vibrational analysis and it is reasonable that such a shift should be rather general.

from equation (2) and there is no justification for obtaining four (or even two) slightly different ionization potentials.⁸ The results are shown in Table III for each of the four series in both molecules. It may be seen that the calculated values deviate appreciably from the observed ones for the lower values of n

TABLE III

RYDBERG SERIES FOR BENZENE AND BENZENE- d_6

n is the principal quantum number

a is the quantum defect

Ionization potential (benzene) = 74587 cm^{-1} (9.247 ev.)

Ionization potential (benzene- d_6) = 74620 cm^{-1} (9.251 ev.)

Series	n	a	Benzene		Benzene- d_6	
			ν_{calc}	ν_{obs}	ν_{calc}	ν_{obs}
$R-A$	2	0.54	57578	55881	57611	55946
	3		65830	65718	65863	65744
	4		69263	69265	69296	69316
	5		71012	71018	71045	71050
	6		72021	72015	72054	72055
	7		72657	72690	72690	72685
	8		73082	73074	73115	73120
	9		73381	73357	73414	73397
	10		73653	73655	73686	73688
$R'-A$	2	0.84	60981	59795	61014	59692
	3		67145	67531	67178	67560
	4		69903	70052	69936	70085
	5		71369	71418	71402	71454
	6		72241	72245	72274	72281
	7		72802	72801	72835	72832
	8		73183	73190	73216	73208
	9		73454	73449	73487	73484
	10		73653	73655	73686	73688
$R''-A$	2	0.89	61448	61421	61481	—
	3		67335	67607	67368	67619
	4		69998	70094	70031	70131
	5		71424	71460	71457	71488
	6		72275	72281	72308	72312
	7		72824	72819	72857	72853
	8		73198	73220	73231	73238
$R'''-A$	2	0.96	62063	64387	62096	64362
	3		67589	67683	67622	67742
	4		70127	70178	70160	70204
	5		71498	71513	71531	71541
	6		72322	72324	72355	72364
	7		72855	72848	72888	72886
	8		73220	73220	73253	73250

but agree well in the higher members. The ionization potential thus obtained for benzene is $74587 \pm 15 \text{ cm}^{-1}$ (9.247 \pm .002 ev.) which is in good agreement with recent photoionization experiments (9.245 \pm .01 ev.) (Watanabe 1954). The result for benzene- d_6 is $74620 \pm 15 \text{ cm}^{-1}$ (9.251 \pm .002 ev.) and the difference between the two (33 cm^{-1}) represents the differences in zero point energies in the ground states of the molecular ions and the neutral molecules.

The identification of the $2R-A$ transition seems rather certain from its vibrational structure and quantum defect (Price and Walsh 1947; Hammond *et al.* 1950; Platt and Kleven's 1947); the identification of $2R'-A$, $2R''-A$,

⁸The doublet splitting in the 2E_g ground state of the molecular ion is probably very small.

$2R'''-A$ is not nearly so certain since the region in which these should fall (1550–1700 Å) contains many diffuse bands. However, more or less regular spacings of 620–680 cm^{-1} can be found (corresponding probably to $2\nu_{18}$) and a provisional assignment of these transitions has been made (Table I).

The most recent work on the ionization potential of benzene by electron impact was done by Fox and Hickam (1954), Morrison (1954), and Nief (1951) who obtained 9.21, 9.3, and 9.3 ev., respectively. The good agreement of the spectroscopic value with those obtained by electron impact and photoionization is gratifying and goes a long way towards confirming the analysis in the present work. The ionization limits calculated from the present data lie very close (within 100–200 cm^{-1}) to a strong absorption doublet which may be seen in Fig. 3 for benzene (1342.5 Å, 1341.5 Å) and in Fig. 4 for benzene- d_6 (1335.4 Å, 1338.3 Å). It is not certain whether these are transitions to the molecular ion or the neutral molecule.

ACKNOWLEDGMENTS

I wish to thank Professors R. S. Mulliken, J. R. Platt, C. C. J. Roothaan, and Dr. L. E. Orgel for many helpful discussions. In particular, I wish to acknowledge the help of Professor Platt and Dr. Orgel for discussions on the Jahn-Teller effect and the identification of the Rydberg series. Finally, I am indebted to Dr. L. C. Leitch of the National Research Council (Canada) for the loan of a sample of benzene- d_6 .

This research was assisted in part by the Office of Ordnance Research under Project TB 2-0001 of Contract DA-11-022-ORD-1002 with the University of Chicago.

REFERENCES

- FOX, R. E. and HICKAM, N. M. 1954. *J. Chem. Phys.* **22**: 2054.
 HAMMOND, V. J. and PRICE, W. C. 1955. *Trans. Faraday Soc.* **51**: 605.
 HAMMOND, V. J., PRICE, W. C., TEEGAN, J. P., and WALSH, A. D. 1950. *Discussions Faraday Soc.* **No. 9**: 53.
 HERZBERG, G. 1945. *Infrared and Raman spectra*. D. Van Nostrand Company, Inc., New York.
 JAHN, A. H. and TELLER, E. 1937. *Proc. Roy. Soc. (London)*, **A**, **161**: 220.
 JONES, L. C. and TAYLOR, L. W. 1955. *Anal. Chem.* **27**: 228.
 MORRISON, J. D. 1954. *J. Chem. Phys.* **22**: 1219.
 MORTON, R. A. and STUBBS, A. L. 1940. *J. Chem. Soc.* 1347.
 MULLIKEN, R. S. 1939. *J. Chem. Phys.* **7**: 20.
 NELSON, R. C. and SIMPSON, W. T. 1955. *J. Chem. Phys.* **23**: 1146.
 NIEF, G. 1951. *J. chim. phys.* **48**: 333.
 NORDHEIM, G., SPONER, H., and TELLER, E. 1940. *J. Chem. Phys.* **8**: 455.
 PASCHEN, F. 1928. *J. Opt. Soc. Amer.* **16**: 231.
 PICKETT, L. W., MUNTZ, M., and MCPHERSON, E. M. 1951. *J. Am. Chem. Soc.* **73**: 4862.
 PLATT, J. R. and KLEVEN, H. B. 1947. *Chem. Revs.* **41**: 301.
 PRICE, W. C. and WALSH, A. D. 1947. *Proc. Roy. Soc. (London)*, **A**, **191**: 22.
 PRICE, W. C. and WOOD, R. W. 1935. *J. Chem. Phys.* **3**: 439.
 ROMAND, J. and VODAR, B. 1951. *Compt. rend.* **233**: 930.
 ROTHAAAN, C. C. J. and MULLIKEN, R. S. 1948. *J. Chem. Phys.* **16**: 118.
 SPONER, H. and TELLER, E. 1941. *Revs. Mod. Phys.* **13**: 75.
 SPONER, H., NORDHEIM, G., SKLAR, A. L., and TELLER, E. 1939. *J. Chem. Phys.* **7**: 207.
 WATANABE, K. 1954. *J. Chem. Phys.* **22**: 1564.
 WILKINSON, P. G. 1955a. *J. Opt. Soc. Amer.* **45**: 862.
 ——— 1955b. *J. Opt. Soc. Amer.* **45**: 1044.
 WILKINSON, P. G. and MULLIKEN, R. S. 1955. *J. Chem. Phys.* **23**: 1895.
 WILKINSON, P. G. and TANAKA, Y. 1955. *J. Opt. Soc. Amer.* **45**: 344.
 ZELIKOFF, M. Unpublished.

NOTES

THE NORMAL CATHODE FALL IN A-C. GLOWS

By E. W. GODBOLE

It is known (Harries and Engel 1951; Joshi 1944) that the photosuppression ($-\Delta i$) of the discharge current is maximum at or near the threshold potential characteristic of the breakdown of a gas. This fact suggested that the mechanism of the effect $-\Delta i$ may be connected with changes of the 'normal' cathode fall which is known to be a major determinant of the glow current in a self-sustained discharge. A reference to the literature also showed absence of quantitative data on the cathode fall measurements under fields due to alternating potentials which, however, have been employed commonly in the studies of $-\Delta i$. Hence it seemed worth while to investigate whether irradiation of a gas discharge leading to a current suppression causes a measurable variation of the cathode fall.

Purified hydrogen was subjected to a 50 c./s. transformer discharge in Geissler tubes fitted with platinum or aluminum disk electrodes having diameters of 1 cm. and 1.4 cm. respectively. Each tube was provided with one movable electrode and a thin cylindrical platinum wire probe (0.2 mm.) partially shielded with glass. A preliminary investigation was carried out to determine the range of pressures of hydrogen (viz., 0.1 mm. to 7 mm. Hg) and of the gap length d (75 mm. to 168 mm.) within which the system showed a large $-\Delta i$ with visible light of but moderate intensity.

The normal cathode fall, V_n , has been defined and measured in various ways. A suitable method employed by the earlier workers consisted in recording the floating potential of a probe placed at the procathode edge of the negative glow. This method was probably open to criticism (Darrow 1932). Later, Oliphant (1931) has discussed the characteristics of small cylindrical probes and shown that the space potential differs very little from the floating potential of the probe—a thin cylindrical probe covered with glass except at the end which dips in the gas. During the present work, the normal cathode fall was measured by the above method, viz. by recording the potential developed by a shielded floating probe placed at the procathode edge of the negative glow, using an electrostatic voltmeter and a calibrated cathode ray oscillograph. Either of these instruments was connected directly across the probe and the earthed electrode for recording V_n . The glow current was measured by a microammeter placed in series with the earthed electrode. For recording current waveforms, the oscillograph was coupled with the earthed electrode through a resistance of 2500 ohms.

According to the usual convention, the glow discharge is 'normal' so long as the negative glow covers the electrode surface only partially. The influence of pressure on the appearance of the negative glow was very marked. At low pressures of hydrogen (below 1 mm. Hg for Pt electrodes and below 2 mm. Hg

for Al electrodes) the discharge was *bipolar*; there was a negative glow at either electrode, followed by a positive column with a well defined but narrow dark space in the center.

At higher pressures, the negative glow appeared only at the earthed electrode and the discharge, termed here as *unipolar*, was similar to that produced under d-c. excitation. The occurrence of the *bipolar* and *unipolar* discharge was an interesting feature of 50 c./s. excitation.

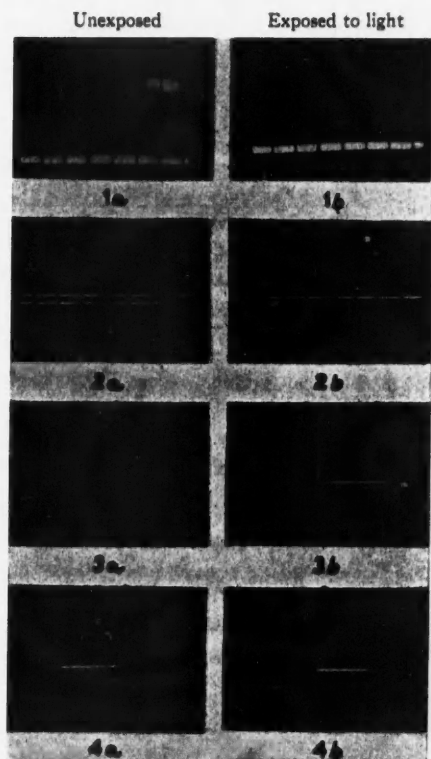


FIG. 1. Normal cathode fall in *unipolar* discharge. Applied potential 1.6 kv., 50 c./s.

FIG. 2. Normal current in *unipolar* discharge. Applied potential 1.6 kv., 50 c./s. (Pt electrodes, pH_2 : 3 mm. Hg, d : 76 mm.)

FIG. 3. Normal cathode fall in *bipolar* discharge. Applied potential 0.8 kv., 50 c./s.

FIG. 4. Normal current in *bipolar* discharge. Applied potential 0.7 kv., 50 c./s. (Al electrodes, pH_2 : 0.3 mm. Hg, d : 165 mm.)

Analogous to what is obtained under d-c. excitation, the normal cathode fall V_n in *unipolar* discharge (50 c./s.) was found to be independent of the pressure of hydrogen and the applied potential. Also the measured values of V_n for Al and Pt electrodes in hydrogen compared well with those recorded in the literature (Bär 1927) on the d-c. glow discharge. At each of the various

pressures within the *unipolar* range, the oscillograph revealed a marked rectification of the discharge current and of the cathode fall. The waveforms of the normal cathode fall and the normal current are shown in Figs. 1(a) and 2(a) respectively. They show completely rectified structures which were characteristic of the *unipolar* discharge.

Under *bipolar* discharge (at lower pressures, when the negative glow appeared at either electrode) the current and voltage pulses occurred symmetrically in both the half cycles, there being no rectification (Figs. 3(a) and 4(a)). Further the value of V_n (for bipolar discharge) measured at either electrode was the r.m.s. value of the voltage. The peak value computed from the r.m.s. value compared well with that cited in the literature for the respective metals.

VALUES OF THE NORMAL CATHODE FALL, V_n , IN VOLTS

	Unipolar	Bipolar		D-c.	Cheney's value (1916)
		r.m.s.	Peak		
Mean value of V_n for Pt in H_2 :	298	215	294	300	302.5
Mean value of V_n for Al in H_2 :	190	129	184	190	197

Experiments were next undertaken for a study of the normal discharge when the tube was exposed to white light from a 200 watt bulb kept at 30 cm. from the discharge tube. Exposure to white light caused a complete suppression of the normal cathode fall (Figs. 1(a), 1(b), and 3(a), 3(b)) and the normal current i_n (Figs. 2(a), 2(b), and 4(a), 4(b)). However, these quantities, namely V_n and i_n , were restored to the normal values on screening off the tube from the light source. The results obtained with Al electrodes were similar to those for Pt electrodes. Exposure to ultraviolet light, obtained from a mercury arc using an interposed Wood's filter, caused an obliteration of the negative glow besides the reversible suppression of V_n and i_n .

Aston's (1911) experiments show that the density ρ^+ of the positive ion space charge (in the Crooke's Dark Space) remains constant so long as the cathode fall is constant. The photosuppression of V_n thus appears to be connected with the photodiminution of the density ρ^+ of the positive ion space charge. This decrease of ρ^+ might be interpreted in terms of the well-known photoactive mechanisms such as (i) the photodestruction of the excited states of hydrogen responsible for the secondary electron liberation, (ii) photodissociation of H_3^+ occurring at higher pressures (Smyth 1931), and (iii) photodissociation of H_2^+ occurring at lower pressures (Smyth 1931), each of which might play a prominent role under optimum conditions. Further work on the influence of traces of electronegative impurities and that of regional irradiation on the normal cathode fall is in progress.

The author is grateful to Professor S. S. Joshi, Principal, College of Science, Banaras, for many helpful discussions.

- ASTON, F. W. 1911. *Proc. Roy. Soc.* **84**: 526.
 BÄR, R. 1927. *In Handbuch der Physik*. Vol. 14. Edited by W. Westphal. Verlag von Julius Springer, Berlin. p. 203.
 CHENEY, W. L. 1916. *Phys. Rev.* **7**: 241.
 DARROW, K. 1932. *Discharge phenomena in gases*. The Williams & Wilkins Company, Baltimore, Md. p. 430.
 HARRIES, W. L. and ENGEL, A. 1951. *Proc. Phys. Soc.* **64**: 916.
 JOSHI, S. S. 1944. *Current Sci. (India)*, **13**: 253.
 OLIPHANT, M. L. E. 1931. *Proc. Roy. Soc.* **132**: 631.
 SMYTH, H. D. 1931. *Revs. Mod. Phys.* **3**: 363.

RECEIVED IN ORIGINAL FORM DECEMBER 7, 1955,
 AND, AS REVISED, FEBRUARY 29, 1956.
 INSTITUTE OF SCIENCE,
 BOMBAY, INDIA.

COMMENTS ON AN EXPERIMENT WITH PERSISTENT CURRENTS

BY M. H. EDWARDS AND D. H. ROGERS

Collins (1955) has recently described an experiment using the apparatus shown in Fig. 1. A thick-walled lead tube was provided with the three rubbing contacts A', A, A'', and one fixed contact B through the base. A persistent

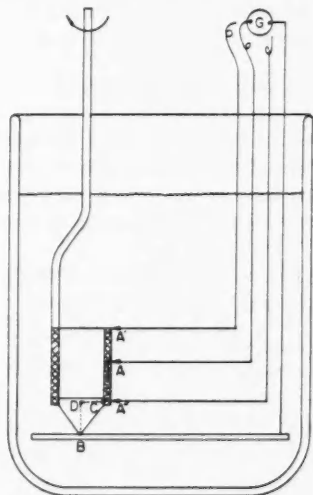


FIG. 1. The apparatus.

current was set up by removing a magnet from the axis of the tube, the tube having been cooled to liquid helium temperatures with the magnet inside. Subsequent rotation of the tube about its vertical axis induced a current in the galvanometer circuit which was the same no matter which of the three rubbing contacts was used, and which did not change with time (over a period of more than a year) provided the rate of rotation was the same.

Collins states that "since there is a finite torque created by the relative motion of the magnetic field of the persistent current and the part of the galvanometer circuit in which the electromotive force arises, the fact that the persistent current neither grows nor decays seems to prove that the magnetic field is associated with the lattice of the superconductor rather than with the superelectrons".

We wish to point out that there is no work done by either the superconducting lattice or the superelectrons, since the part of the galvanometer circuit in which the e.m.f. is generated is just the (presumably normal conducting) metallic conical base which is attached to the lead tube.

The magnetic field of the tube is unaffected by rotation as it is symmetrical about the axis of rotation (cf. Alers *et al.* 1951). Thus the motional e.m.f. will only be produced in the parts of the circuit which move in this fixed field. Thus the e.m.f. between B and A, say, in Gaussian units, is

$$\epsilon = \int_B^A \mathbf{E} \cdot d\mathbf{l} = \int_B^A (1/c) \mathbf{v} \times \mathbf{B} \cdot d\mathbf{l},$$

where \mathbf{v} is the velocity of each line element of length $d\mathbf{l}$. This line integral is independent of the path of integration. Integrating along the dotted path BDCA in Fig. 1, we see that along the axis BD, $\mathbf{v} = 0$, and that along CA, inside the superconductor, $\mathbf{B} = 0$. Hence the e.m.f. is given by

$$\epsilon = \int_D^C (1/c) \mathbf{v} \times \mathbf{B} \cdot d\mathbf{l},$$

which is that of the classical "Faraday disk" generator. Clearly this e.m.f. is the same no matter which of the rubbing contacts is used. This analysis also shows that if the conical base were made of superconducting material, there would be no e.m.f. generated (cf. Wexler and Corak 1949; Houston and Squire 1949).

When a current i flows through the galvanometer circuit there will be a force $d\mathbf{F}$ on each current element of length $d\mathbf{l}$ in the magnetic field \mathbf{B} such that

$$d\mathbf{F} = (i/c) d\mathbf{l} \times \mathbf{B}.$$

The forces on the current elements do not move any of them, as even the current through the rotating member is fixed in space by the position of the contacts. So the magnetic field supplies no energy and thus the supercurrents are unaffected. There is, however, a torque $d\mathbf{L}$ on each part of the current in the moving member such that

$$d\mathbf{L} = \mathbf{r} \times d\mathbf{F},$$

where \mathbf{r} is the distance from the axis. This torque is equal and opposite to the torque supplied by the rotating mechanism. Neglecting friction, the power supplied by this mechanism will be equal to

$$\begin{aligned} \text{Power in} &= \int_B^A \boldsymbol{\omega} \cdot d\mathbf{L} \\ &= \int_B^A \mathbf{v} \cdot d\mathbf{F} \end{aligned}$$

$$\begin{aligned}
 &= (e/R) \int_{\mathcal{L}} (1/c) \mathbf{v} \cdot d\mathbf{l} \times \mathbf{B} \\
 &= -(e^2/R),
 \end{aligned}$$

where R is the resistance in the galvanometer circuit. This is just the Joule heating in the galvanometer circuit, verifying that the magnetic field neither loses nor gains energy from this rotation. Hence this experiment does not justify Collins' rather startling conclusion regarding the nature of the magnetic field.

Collins' method for detecting the magnetic field of a supercurrent without taking any energy away from it remains an ingenious one.

- ALERS, P. B., McWHIRTER, J. W., and SQUIRE, C. F. 1951. *Phys. Rev.* 84: 104.
 COLLINS, S. C. 1955. *Proc. Conference de Physique des Basses Températures*, Paris. p. 588.
 HOUSTON, W. V. and SQUIRE, C. F. 1949. *Phys. Rev.* 76: 685.
 WEXLER, A. and CORAK, W. S. 1949. *Phys. Rev.* 76: 432.

RECEIVED FEBRUARY 27, 1956.
 ROYAL MILITARY COLLEGE OF CANADA,
 KINGSTON, ONTARIO.

LETTERS TO THE EDITOR

Under this heading brief reports of important discoveries in physics may be published. These reports should not exceed 600 words and, for any issue, should be submitted not later than six weeks previous to the first day of the month of issue. No proof will be sent to the authors.

Fine Structure Analysis and Mutual Perturbation of the δ and β Bands of the NO Molecule*

The absorption spectrum of nitric oxide has been studied in the vacuum region with a reciprocal dispersion of 0.63 Å/mm. The same experimental arrangement as described by Herzberg and Hugo (1955) was used: Lyman discharge, low temperature absorption tube, 3 meter vacuum spectrograph. The absorbing path was 26.5 cm., the pressure of the NO gas ranged from 0.1 to 4 mm. Hg and its temperature was -183°C . The low temperature reduced very effectively overlapping of band structures and at the same time eliminated completely absorption by impurities.

The spectra obtained show for the first time well-resolved fine structure in the bands of the β , δ , and ϵ progressions lying in the near Schumann region (2000–1650 Å) as well as very many resolved bands at shorter wavelengths (1650–1400 Å) including the E - X bands (Tanaka, Seya, and Mori 1951) and the β' bands (Miescher 1955) known from emission spectra.

Rotational analyses have been made for the δ and β bands (representing the C - X and B - X transitions of NO) and the B values are given in Table I. Contrary to the result of Schmid

TABLE I

ASSIGNMENTS AND ROTATIONAL CONSTANTS OF THE β AND δ BANDS OF NO

B_0 was obtained from the formula $B_0 = \frac{\Delta_2 F_1(J) + \Delta_2 F_2(J)}{8(J+3/2)}$ (average of the two spin-doublet components); when

this expression is not independent of J , as happens in some of the perturbed bands, the value is enclosed in brackets J and i are estimated intensities of the whole bands and the satellite branches respectively q is the constant of the A -type doubling [$\Delta\nu = qJ(J+1)$]

Band heads $\lambda(\text{\AA})$	β Bands (B - X)				δ Bands (C - X)			$B(\delta) + B(\beta)$	q
	(v', v'')	I	i	$B_0(B^2\Pi)$	(v', v'')	I	$B_0(C^2\Pi)$		
1982	(5,0)	3	0	1.054					
1945	(6,0)	3	1	1.041					
1910	(7,0)	4	—	1.028	(0,0)	8	1.981	3.01	0.016
1877	(8,0)	1	—	—					
1845	(9,0)	4	1	1.019					
{ 1828					(1,0)	10	1.927	2.95	0.014
{ 1815	(10,0)	2	0	1.022					
{ 1787	(11,0)	4	1	1.010					
{ 1762	(12,0)	6	4	(1.3-1.2)	(2,0)	9	(1.5-1.6)	2.81	0.010
{ 1752	(13,0)	—	—	—					
1733	(14,0)	3	1	1.03					
1708	(15,0)	7	4	(1.4-1.3)					
{ 1689					(3,0)	8	(1.3-1.4)	2.66	0.003
{ 1676									0.009
1658	(16,0)	2	1	0.997					
1636	(17,0)	—	—	—					
{ 1620	(18,0)	2	—	0.98	(4,0)	7	1.77	2.75	0.017
{ 1616									
1598	(19,0)	1	—	0.97					

(1930), the δ bands have been found to be a $^2\Pi$ - $^2\Pi$ transition with the upper state $C^2\Pi$ near case b ($A \approx +4 \text{ cm}^{-1}$) and with a large A -type doubling. The $B^2\Pi$ and $C^2\Pi$ states show mutual perturbations of the homogeneous type which can be followed in detail. Mutual perturbations were suggested formerly by several authors on the basis of low dispersion spectra, especially by Sutcliffe and Walsh (1953). The bands $\delta(0,0)$ and $\beta(7,0)$ are superimposed in the spectrum. They show a small perturbation for $J \leq 5\frac{1}{2}$ but give normal values for $B_0(\delta)$ and $B_0(\beta)$. The perturbation is stronger between the pair $\delta(1,0)$ and $\beta(10,0)$ but separate values for $B_1(\delta)$ and $B_{10}(\beta)$ are still well defined. The origins of $\delta(2,0)$ and $\beta(12,0)$ are shifted in opposite directions by approximately 80 cm^{-1} from their unperturbed positions. The well-defined sum $B_2(\delta) + B_{12}(\beta)$ given in the table has been determined by combination rela-

*Issued as N.R.C. No. 3956.

tions from perturbation theory (Kovács 1937; Hultin and Lagerqvist 1951). The $(\Delta_2 F_1 + \Delta_2 F_2)/8(J + \frac{1}{2})$ curves tend to approach normal B values only for high J not observed here. The upper states of the $\delta(3, 0)$ and $\beta(15, 0)$ bands are nearly 50:50 mixtures of the $C^2\Pi(v = 3)$ and $B^2\Pi(v = 15)$ states. These bands are shifted from their unperturbed position in opposite directions by about 200 cm^{-1} . A good value for the sum $B_2(\delta) + B_{15}(\beta)$ results from the combination relations. The next pair of nearly coinciding bands $\delta(4, 0)$ and $\beta(18, 0)$ shows much less mixing as can be seen from the B values given in Table I.

The β bands, $\beta(9, 0)$, $\beta(11, 0)$, $\beta(14, 0)$, and $\beta(16, 0)$, lying between the δ - β pairs discussed above as well as $\beta(19, 0)$ are more or less unperturbed. The band $\beta(13, 0)$ is hidden in $\epsilon(2, 0)$, and $\beta(17, 0)$ is overlapped by $\beta'(1, 0)$. Both these bands have not yet been analyzed but wave numbers of their first R_1 lines have been taken from the plates.

As a check for the identifications of the β bands and in order to establish their vibrational numbering, the values $\nu - 1037(v + \frac{1}{2})$ were plotted against v for all measured bands. As Fig. 1 shows, a fairly smooth line is obtained when the above-mentioned shifts are made for the few

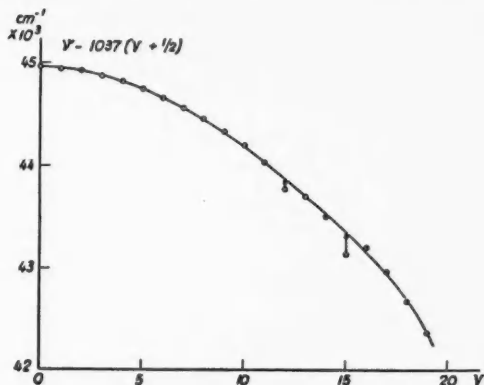


FIG. 1. Band origins of the β bands of NO. $\nu(v, 0) - 1037(v + \frac{1}{2})$ is plotted instead of $\nu(v, 0)$ in order to have a suitable ordinate scale. ν = wave number of the first line of the R_1 branch. The arrows mark shifts from the perturbed positions.

bands strongly influenced by coinciding δ bands. Further confirmation for the present interpretation comes from the observation of isotope bands: the $N^{14}O$ bands corresponding to $\beta(14, 0)$ and $\beta(16, 0)$ are found to show displacements in accordance with theory. The $N^{14}O$ and NO^{18} bands corresponding to the perturbed pair $\beta(15, 0)$ and $\delta(3, 0)$ are readily measurable and show vibrational isotope displacements of equal magnitude ($\Delta\nu^i = -188 \text{ cm}^{-1}$ for $N^{14}O$ and $\Delta\nu^i = -276 \text{ cm}^{-1}$ for NO^{18}) for the two mutually perturbing levels, as might be expected for a 50:50 mixture. Further evidence of the mixing of states in the strongly perturbed levels comes from the observation that the β bands [$^2\Pi(a) - ^2\Pi(a)$] assume in the region of mutual perturbation, $v = 15$ in $B^2\Pi$ and $v = 3$ in $C^2\Pi$. In this region the curves are drawn dotted as their meaning is restricted. Except near this point of intersection, the approximation in which a crossing takes place seems appropriate for the calculation of the vibrational levels.

The perturbations between the B and C states of NO described here represent an unusually fine example of the effects of crossing of potential curves or, in other words, of vibrational perturbations. In Fig. 2 are drawn potential energy curves for the known electronic states of the NO molecule. The crossing point of the $B^2\Pi$ and $C^2\Pi$ states must fall at the energy of the levels of strongest mutual perturbation, $v = 15$ in $B^2\Pi$ and $v = 3$ in $C^2\Pi$. In this region the curves are drawn dotted as their meaning is restricted. Except near this point of intersection, the approximation in which a crossing takes place seems appropriate for the calculation of the vibrational levels.

There can be no doubt that the $B^2\Pi$ state correlates at the dissociation limit with the $^2D(N) + ^1P(O)$ atomic states whose energy is $71,700 \text{ cm}^{-1}$ above the ground state $X^2\Pi$ of NO if the now almost generally accepted value $D_0^0(NO) = 6.50 \text{ eV}$ is assumed. The value $D_0^0(NO) = 5.31 \text{ eV}$ would give a limit of $B^2\Pi$ at $62,100 \text{ cm}^{-1}$ not compatible with the now observed level $v = 19$ at $62,590 \text{ cm}^{-1}$.

A search for the γ bands with $v' > 3$, unknown until now, has been successful insofar as on our absorption plates the $\gamma(4, 0)$ band has been found within the $\epsilon(0, 0)$ band. The R_1 , Q_1 ,

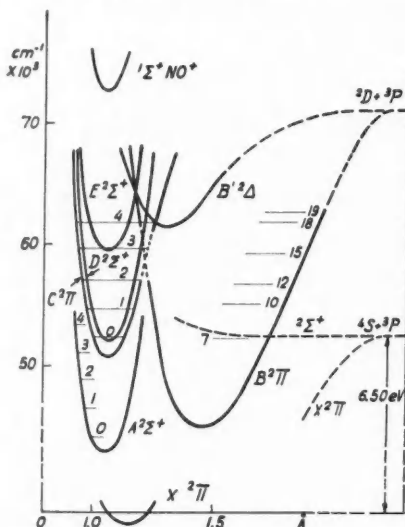


FIG. 2. Potential curves of the NO molecule.
The β , γ , δ , ϵ , and β' bands correspond to the transitions $B-X$, $A-X$, $C-X$, $D-X$, and $B'-X$ respectively.

and P_1 branches of $\gamma(4, 0)$ (Q_1 head at $53,368 \text{ cm}^{-1}$, $B_1(A^2\Sigma^+) = 1,909 \text{ cm}^{-1}$) appear without disturbing overlapping by $\epsilon(0, 0)$ lines. Fig. 2 shows the positions of the vibrational levels in the $A^2\Sigma^+$ state.

The non-appearance of β bands in emission from initial levels above $B^2\Pi$ ($v = 7$) has long been known and is most probably due to the interaction between the $B^2\Pi$ state and the continuum of the $^2\Sigma^+$ state arising from normal atoms. Because of the strong interaction between the B and C states, the C state also will interact with the continuum of the $^2\Sigma^+$ state just mentioned. This may account for the non-appearance of δ bands with $v' > 0$ in emission. But no corresponding broadening of the lines of the β and δ bands above the limit of the $^2\Sigma^+$ state has been observed in the high resolution absorption plates indicating that the predissociations of the B and C states are weak.

A detailed paper will be published later.

We are greatly indebted to Mr. J. Shoosmith for his efficient help in the experiments. This investigation was aided by a research grant from the Swiss National Fund.

HERZBERG, G. and HUGO, T. J. 1955. *Can. J. Phys.* **33**: 757.

HULTIN, M. and LAGERQVIST, A. 1951. *Arkiv Fysik*, **2**: 471.

KOVÁCS, I. 1937. *Z. Physik*, **106**: 431.

MIESCHER, E. 1955. *Can. J. Phys.* **33**: 355.

SCHMID, R. 1930. *Z. Physik*, **64**: 279.

SUTCLIFFE, L. H. and WALSH, A. D. 1953. *Proc. Phys. Soc. (London)*, **A**, **66**: 209.

TANAKA, Y., SEYA, M., and MORI, K. 1951. *J. Chem. Phys.* **19**: 979.

RECEIVED MARCH 26, 1956.
DIVISION OF PURE PHYSICS,
NATIONAL RESEARCH COUNCIL,
OTTAWA, CANADA

AND
PHYSICAL INSTITUTES OF THE UNIVERSITIES OF STOCKHOLM (SWEDEN) AND
BASEL (SWITZERLAND)

G. HERZBERG
A. LAGERQVIST
E. MIESCHER

THE PHYSICAL SOCIETY

MEMBERSHIP of the Society is open to all who are interested in Physics.

FELLOWS pay an Entrance fee of £1 1s. (\$3.00) and an Annual Subscription of £2 2s. (\$6.00).

STUDENTS: A candidate for Studentship must be between the ages of 18 and 26, and pays an Annual Subscription of 5s. (\$0.75).

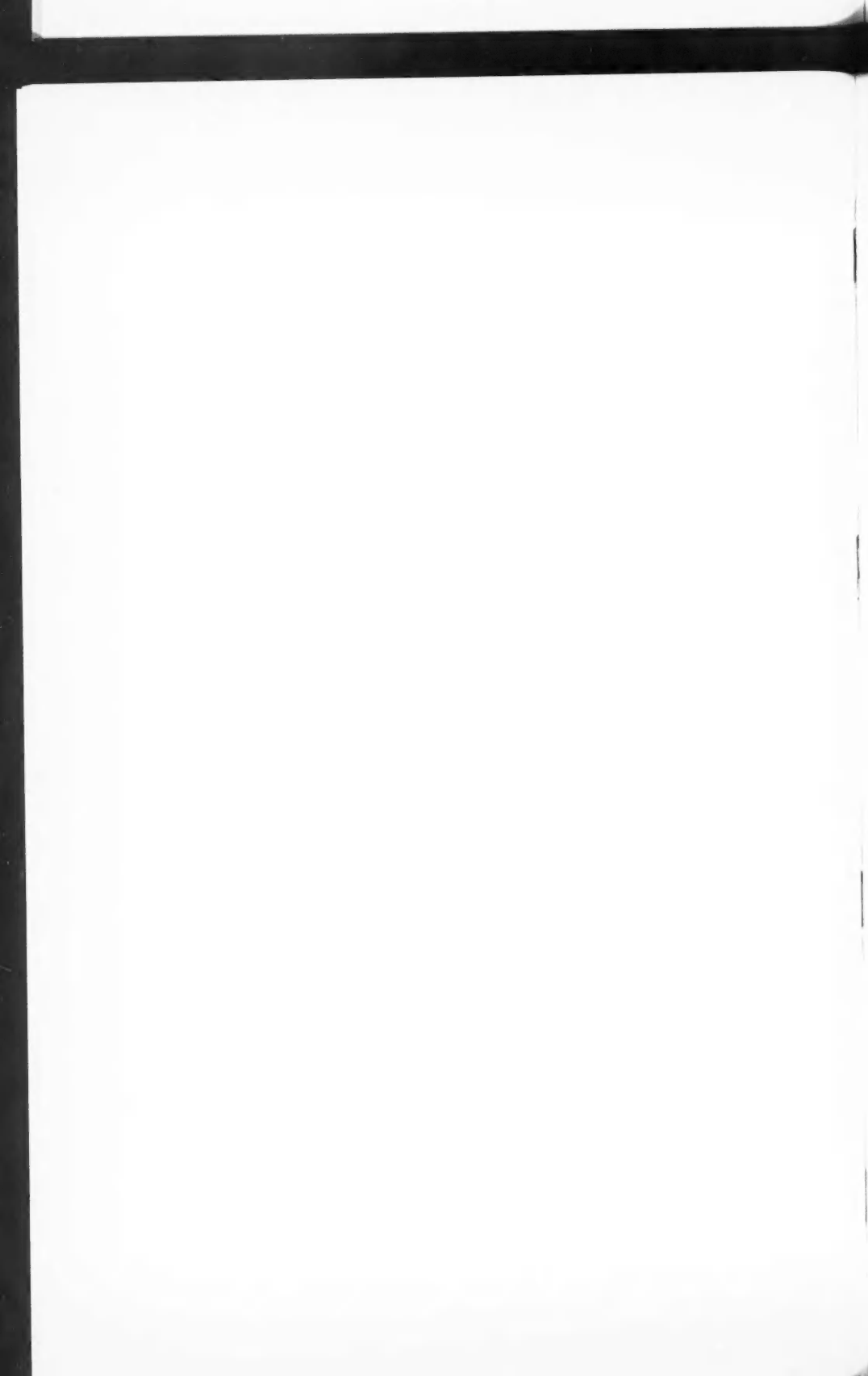
MEETINGS: Fellows and Students may attend all Meetings of the Society including the annual Exhibition of Scientific Instruments and Apparatus.

PUBLICATIONS include the *Proceedings of the Physical Society*, published monthly in two sections, and *Reports on Progress in Physics*, published annually. Volume XVIII, 1955, is now available (price 50s. (\$7.15)). Members are entitled to receive many of the Publications at a reduced rate.

Further information can be obtained from:

THE PHYSICAL SOCIETY

1, LOWTHER GARDENS, PRINCE CONSORT ROAD
LONDON, S.W.7, ENGLAND



CANADIAN JOURNAL OF PHYSICS

Notes to Contributors

Manuscripts

(i) **General.** Manuscripts, in English or French, should be typewritten, double spaced, on paper $8\frac{1}{2} \times 11$ in. **The original and one copy are to be submitted.** Tables and captions for the figures should be placed at the end of the manuscript. Every sheet of the manuscript should be numbered.

Style, arrangement, spelling, and abbreviations should conform to the usage of this journal. Names of all simple compounds, rather than their formulas, should be used in the text. Greek letters or unusual signs should be written plainly or explained by marginal notes. Superscripts and subscripts must be legible and carefully placed.

Manuscripts and illustrations should be carefully checked before they are submitted. Authors will be charged for unnecessary deviations from the usual format and for changes made in the proof that are considered excessive or unnecessary.

(ii) **Abstract.** An abstract of not more than about 200 words, indicating the scope of the work and the principal findings, is required, except in Notes.

(iii) **References.** References should be listed **alphabetically by authors' names**, unnumbered, and typed after the text. The form of the citations should be that used in issues of this journal published in 1956; in references to papers in periodicals, titles should not be given and only initial page numbers are required. The names of periodicals should be abbreviated in the form given in the most recent *List of Periodicals Abstracted by Chemical Abstracts*. All citations should be checked with the original articles and each one referred to in the text by the authors' names and the year.

(iv) **Tables.** Tables should be numbered in roman numerals and each table referred to in the text. Titles should always be given but should be brief; column headings should be brief and descriptive matter in the tables confined to a minimum. Vertical rules should be used only when they are essential. Numerous small tables should be avoided.

Illustrations

(i) **General.** All figures (including each figure of the plates) should be numbered consecutively from 1 up, in arabic numerals, and each figure referred to in the text. The author's name, title of the paper, and figure number should be written in the lower left corner of the sheets on which the illustrations appear. Captions should not be written on the illustrations (see Manuscripts (i)).

(ii) **Line Drawings.** Drawings should be carefully made with India ink on white drawing paper, blue tracing linen, or co-ordinate paper ruled in blue only; any co-ordinate lines that are to appear in the reproduction should be ruled in black ink. Paper ruled in green, yellow, or red should not be used unless it is desired to have all the co-ordinate lines show. All lines should be of sufficient thickness to reproduce well. Decimal points, periods, and stippled dots should be solid black circles large enough to be reduced if necessary. Letters and numerals should be neatly made, preferably with a stencil (**do NOT use typewriting**) and be of such size that the smallest lettering will be not less than 1 mm. high when reproduced in a cut 3 in. wide.

Many drawings are made too large; originals should not be more than 2 or 3 times the size of the desired reproduction. In large drawings or groups of drawings the ratio of height to width should conform to that of a journal page but the height should be adjusted to make allowance for the caption.

The original drawings and one set of clear copies (e.g. small photographs) are to be submitted.

(iii) **Photographs.** Prints should be made on glossy paper, with strong contrasts. They should be trimmed so that essential features only are shown and mounted carefully, with rubber cement, on white cardboard with no space or only a **very** small space (less than 1 mm.) between them. In mounting, full use of the space available should be made (to reduce the number of cuts required) and the ratio of height to width should correspond to that of a journal page ($4\frac{1}{2} \times 7\frac{1}{2}$ in.); however, allowance must be made for the captions. Photographs or groups of photographs should not be more than 2 or 3 times the size of the desired reproduction.

Photographs are to be submitted in duplicate; if they are to be reproduced in groups one set should be mounted, the duplicate set unmounted.

Reprints

A total of 50 reprints of each paper, without covers, are supplied free. Additional reprints, with or without covers, may be purchased.

Charges for reprints are based on the number of printed pages, which may be calculated approximately by multiplying by 0.6 the number of manuscript pages (double-spaced typewritten sheets, $8\frac{1}{2} \times 11$ in.) and including the space occupied by illustrations. An additional charge is made for illustrations that appear as coated inserts. The cost per page is given on the reprint requisition which accompanies the galley.

Any reprints required in addition to those requested on the author's reprint requisition form must be ordered officially as soon as the paper has been accepted for publication.

Contents

	Page
Paramagnetism of the γ Phase in Copper Manganese Alloys— <i>H. P. Myers</i> - - - - -	527
The Duration of Forward-scattered Signals from Meteor Trails— <i>P. A. Forsyth and E. L. Vogan</i> - - - - -	535
Diffraction of 3.2 cm. Electromagnetic Waves by Dielectric Rods. I. Lucite and Tenite 1 in. Diameter Cylinders— <i>M. K. Subbarao</i> and <i>A. B. McLay</i> - - - - -	546
Diffraction of 3.2 cm. Electromagnetic Waves by Dielectric Rods. II. Lucite 1½ in. Diameter Cylinder and Semicylinder— <i>A. B.</i> <i>McLay and M. K. Subbarao</i> - - - - -	555
The Resolver, a Circuit for Reducing the Counting Losses of a Scaler— <i>R. E. Bell</i> - - - - -	563
Nuclear Quadrupole Resonance Spectrum of B ¹¹ in Kernite— <i>R. R.</i> <i>Haering and G. M. Volkoff</i> - - - - -	577
Low Frequency Radiation from a Horizontal Antenna over a Spherical Earth— <i>James R. Wait</i> - - - - -	586
Absorption Spectra of Benzene and Benzene- <i>d</i> ₆ in the Vacuum Ultraviolet— <i>P. G. Wilkinson</i> - - - - -	596
Notes:	
The Normal Cathode Fall in A-c. Glows— <i>E. W. Godbole</i> - -	616
Comments on an Experiment with Persistent Currents— <i>M. H.</i> <i>Edwards and D. H. Rogers</i> - - - - -	619
Letters to the Editor:	
Fine Structure Analysis and Mutual Perturbation of the δ and β Bands of the NO Molecule— <i>G. Herzberg, A. Lagerqvist, and</i> <i>E. Miescher</i> - - - - -	622

